NANOFIBER-BASED TISSUE ENGINEERING SCAFFOLDS FOR REPAIRING INJURED NERVES AND SOFT TISSUES

By

Russell A. Martin

A dissertation submitted to Johns Hopkins University in conformity with the requirements for the degree of Doctor of Philosophy

Baltimore, Maryland

August 2015

Abstract

One objective of the field of tissue engineering is to develop new biomaterials to unlock the body's own potential to rebuild itself. Electrospun nanofibers are one such material, providing topographical features on the length-scales relevant for cellular interactions, recapitulating the cues from the native extracellular matrix. Nanofiber-based scaffolds require careful design to maximize fiber-cell interactions on the micron scale without sacrificing the porosity necessary for healthy healing responses. This thesis describes our work in developing electrospun nanofiber-based scaffolds for improved healing in peripheral nerve and soft tissue injuries.

Peripheral nerve injuries pose a major health problem, leading to severe disability and poor quality of life. It is estimated that 5% of all open traumatic wounds are associated with peripheral nerve injuries, resulting in about 560,000 nerve repairs performed each year in the United States. Despite advancements in surgical techniques, functional recovery remains suboptimal. We have developed nanofiber-based nerve guides to provide off-the-shelf scaffolds for improving repairs in no-gap repairs, gap repairs, and ventral root avulsion repairs. We optimized the fiber properties through live-cell tracking and spheroid migration studies to maximize the contact guidance to Schwann cells, the key support cells of the peripheral nerve. We conducted extensive *in vivo* studies in rats, dogs, and rhesus macaques to determine the optimal design to maximize cell-fiber interactions without limiting porosity.

Soft tissue losses from cancer surgery, trauma, aging, or congenital malformation affect millions of people each year. The loss of such tissues including skin, fat, fascia, and muscle can lead to major functional and aesthetic disturbances that are difficult to reconstruct with conventional methods. For example, more than 300,000 women a year undergo partial mastectomies for breast cancer in the United States, resulting in disfiguring deformities that go untreated in most cases. We have developed a novel scaffold for these injuries comprised of a composite between dispersed nanofibers and a hyaluronic acid hydrogel. These composites can match the stiffness of native fat while simultaneously retaining the porosity necessary for enhanced cellular infiltration and remodeling. We characterized the composite properties through extensive mechanical testing and demonstrated their efficacy through *in vivo* studies.

Readers:

Hai-Quan Mao, Ph.D. (Advisor)

Ahmet Höke, M.D., Ph.D. (Co-Advisor)

Defense Committee:

Peter Searson, Ph.D.

Kalina Hristova, Ph.D.

Warren Grayson, Ph.D.

Acknowledgements

The process of obtaining the skills, knowledge, and research necessary to obtain a PhD is a daunting undertaking that I've only been able to complete with the help of many, many people. I would like to first thank Dr. Hai-Quan Mao, who worked with me tirelessly, with encouragement through the inevitable ups and downs of the research process. He taught me how to carefully and gracefully prepare and analyze scientific experiments and how to oversee the work of others. He took a leap of faith when he took me on as a graduate student. Finally, I wish to thank him for being one of the nicest, supportive people I have ever met.

I would also wish to thank the many coworkers and mentors from my industry experiences that prepared me for graduate studies. In particular, I thank Ira Ison, Yves Arramon, and Travis Rappleye at Calcitec Biomaterials and Satoshi Ohtake, Luisa Yee, Binh Pham, and Vu Truong at Aridis Pharmaceuticals. I would like to especially thank Vu for his help in my search for grad schools and for recommending me to join Dr. Mao's lab.

Next, I wish to thank my colleagues within the Mao lab, many of whom worked with me intimately on the subjects of this dissertation. My undergraduate researchers Andrew Kim, Alex Mullen, Kevin Feng, and Andrew Han helped generate much of this data and shared my trials and tribulations. Kellin Krick was integral to my nerve repair projects, working with me literally side-by-side on my in vitro and in vivo nerve repair studies. The regenerative medicine subgroup provided valuable feedback and suggestions, with valuable discussions on electrospinning and nerve repair with Eric Lopez, Shawn Lim, Jose Roman, Shuming Zhang, Korey Kam, Brian Ginn and always

thoughtful critiques from Markus Tammia. I further thank Xiaowei Li, Xuesong Jiang, and especially Jisuk Choi for their collaborative work on our soft tissue composites. Thank you to the rest of Mao lab for all of your help, suggestions, and encouragement.

I am also indebted to my many collaborators, beginning with YuJa Huang and Dr. Searson's lab, who performed all of the live-cell tracking experiments. Dr. Hoke was an excellent co-advisor to me and provided invaluable guidance into peripheral nerve regeneration. Without the help of Ruifa Mi, this thesis would have been impossible. He dedicated hundreds of hours into performing all of the nerve repair surgeries, as well as countless hours aiding me with the electrophysiology and histology analyses. I would also like to thank Dr. Leif Havton and his lab in performing the delicate, time-consuming ventral-root avulsion surgeries and analyses. The soft tissue regeneration project was only possible with the help of Dr. Sacks, Dr. Sashank Reddy, and Georgia Yalanis. I would also like to thank my many other collaborators from my other projects, such as Val Sluch and Dr. Zack, Jean-Philippe Richard, Karim Sarhane, and Zuhaib Ibrahim. I would like to further thank Dr. Mao, Dr. Hoke, Dr. Searson, Dr. Grayson, and Dr. Hristova for serving on my thesis defense committee.

I would like to thank my friends out here in Baltimore, for keeping me sane and happy through the PhD process. I made several lifelong friends in the department, including Travis Dejournett, Stephen Farias, Adam Stover, Korey Kam, Charli and Tom Dawidczyk, Jesse and Amanda Placone, and Justin Bradfield. Thanks to everyone for coming out to the department softball games; they were the highlight of the summer for me every year. I would also like to specifically thank my climbing friends for introducing me to a new passion and new adventures, particularly Andrew Wong, YuJa Huang,

Charles Hu, Kayam Chak, Tricia Gibo, Guus Bol, Francisco Munoz, Sven Cattell, Eric Chow, and all of my other friends at Earth Treks.

My family has been both a support and inspiration for me. My parents, themselves chemical engineers, instilled and nurtured a sense of curiosity in me that lies at the heart of my love of science. They helped get me through moments of doubt in my undergraduate studies and encouraged me to take the leap into the unknown of graduate studies across the country. My brothers gave me great role models, both in being good students and researchers, but also being great husbands and fathers. They have also given me sisters-in-law, nephews, and a niece that have added joy to my life as well.

Finally, I would like to thank my fiancé, Brittany Sumnicht, for her tireless support throughout the long PhD process, particularly the stressful dissertation-writing period. My life has been immeasurably better for the light she has brought the last five years, and I can't wait for the adventures we will embark on next.

Table of Contents

Table of Figures

Chapter 1 Tissue Engineering and Topographical Guidance

1.1 The field of tissue engineering

In the first issue of the journal *Tissue Engineering*, Tissue Engineering is defined as the use of living cells, manipulated through their extracellular environment and genetics to develop biological substitutes for implantation into the body and/or to foster the remodeling of tissue in some other active manner [1]. The tissue engineering field has exploded since this first publication in 1995, to the point where 8,000 tissue engineering papers were published between January 2012 and September 2013 [2]. The field has also received significant institutional support, with dedicated centers at many elite institutions such as the Translational Tissue Engineering Center (TTEC) at Johns Hopkins. The cellular-based therapy branch has thrived, particularly since the discovery of embryonic stem cells and induced pluripotent stem cells, though the promise of these technologies has still not been translated into clinical use [3]. The use of minimally modified cells and tissues has seen quicker adoption, such as fat grafting or the use of mesenchymal stem cells (MSCs). Considerable effort has also been employed to produce biomaterials capable of inducing remodeling by the body's native cells. These strategies mitigate the risks inherent to cell-based therapies and have significantly easier paths to clinical adoption. The field has improved the hosts response to the biomaterials in several applications, including utilizing hydrogels and decellularized tissues, modifying the hydrophobicity and biochemistry of implant surfaces, providing adhesive cues,

incorporating biodegradable elements, varying pore sizes, and creating scaffolds that allow for three-dimensional cellular migration and growth instead of the standard flat geometries of traditional cell culture.

1.2 Topographical guidance within the native ECM

Cells interact mechanically with their environment on many different length-scales simultaneously, modulating cell adhesion, migration, proliferation, differentiation, maturation, and overall cell function [4]. On the molecular length scale, cells have evolved to respond to many biochemical cues present in the extracellular matrix (ECM), such as those provided by proteoglycans, laminins, chondroitin sulfates, fibronectin, hyaluronic acid, and elastin. There are at least 28 different subtypes of collagen alone, each with different yet overlapping functions [5]. For instance, in peripheral nerve regeneration, several different collagen subtypes each play different key roles in Schwann cell proliferation and function, dorsal root ganglion organization, myelination, and perineurial formation [6]. Hyaluronic acid can encourage cell migration and discourage cell-cell adhesion [7]. Laminin can facilitate or inhibit cell migration depending upon the surface density [8]. Fibronectin can enable cell migration and aids translocation better than laminin [9]. Chondroitin sulfate plays a key role in both peripheral and central nervous system regeneration, with certain subtypes severely inhibiting axonal regeneration [10]. The cells sense their environment in part through membrane integrin receptors, which mediate cell adhesion as well as serving as signaling molecules to direct the cell function in myriad ways [11-17].

Increasing the length scale to that of 10's of nanometers introduces numerous surface features that influence cellular function through mechanical action. The basement membrane is the supportive substrate for cells found throughout the vertebrate body and is made of ECM components such as collagen, hyaluronic acid, proteoglycans, fibronectin, and laminin [18]. The basement membrane is composed of numerous features, such as ridges, fibers, and pores. For example, the corneal epithelial basement membrane has an average feature height of between 147 nm and 191 nm, and average fiber width of 77 nm, and 15% of the surface area is covered with pores with an average diameter of 72 nm [19, 20]. Likewise, the rat kidney ECM has fibrils 5-9 nm in diameter and pores 11-30 nm wide [21]. Similarly, the glomular, tubular, and Bowman's capsule membranes in rats have fibers 6-7 nm in diameter and pores 9-13 nm wide [22]. Feature sizes of this length-scale are observable to the body's cells. The composition and features of the corneal basement membrane have been shown to influence cellular proliferation, migration, and differentiation[23-26].

Increasing the length scales of topographical features further into the range of hundreds of nanometers has a profound effect upon cell motility and function through the guidance of the cell lamellipodia and filopodia. Lamellipodia, the primary organelles for cell motility, are sheet-like projections about 200 nm thick and 1-5 μm in breadth (depending upon cell type) that extend in front of spreading or migrating cells. They are the primary sites of the actin polymerization, the "filament factory" of the cell [27]. They also direct the formation of adhesion complexes and are involved with macropinocytosis

and phagocytosis [27]. The branched actin can coalesce into thin projections called "microspikes" when within the lamellipodia or "filopodia", tight parallel bundles of filamentous F-actin 100-300 nm in width, which can extend for several microns out from the lamellipodia when extended [28]. The filopodia are key in both initiating motility, but also in sensing the environment; integrins and cadherins accumulate within the filopodia in an unligated, but activated state, serving as "sticky fingers" for cell adhesion and motility [29]. Filopodia also exist in large numbers in neuronal growth cones and are able to sense gradients and direct growth towards the chemoattractant [30]. Thus, features at the molecular scale, nanometer scale, and 100's of nanometer scale can potentially synergistically effect cell function and motility by regulating the activation of surface receptors, guiding actin formation, and directing the overall organization and growth of filopodia and lamellipodia.

Finally, surface features in the length-scale of microns and above can also direct cell function and motility. One mechanism is to physically restrict the whole cell body, forcing the cell to take on an elongated morphology to squeeze through a pore or by restricting the directions the cell can migrate towards. Schwann cells, for instance, have a thickness of 200-500 nm, widening to 2-5 μm at the nucleus, with the nucleus 10-20 μm long and the total cell length ranging in the hundreds of microns in the mature state [31]. The sural (sensory) axon diameter and nerve fiber diameter (axon + myelin) in the cat is bimodal, with peaks at 2 μm and 6 μm for the axon and peaks at 6 μm and 10 μm for the nerve fiber; the medial gastrocnemius (motor) axons and nerve fibers are also bimodal with peaks at 1.5 μm and 5 μm for the axon and 6 μm and 16 μm for the nerve fiber [32].

The axons ranged from 1 to 10 μm in diameter and the nerve fiber diameter ranged from 2 to 20 μm for the two nerve types. Topographical features of a similar dimension can either physically restrict cellular movement or be interpreted as cells themselves. Schwann cells and oligodendrocytes preferentially myelinate the larger axons first [33].

One example of the nanotopography of the native ECM can be seen in the structure of adipose tissue (Fig 1.1). The adipocytes store fat in large vacuoles with diameters of around 100 μm. Following decellurization and delipidization, the fibrillar nature of the surrounding ECM is exposed, both on the surface and emerging from the basement membrane. Cryomilling the decellularized, delipidized tissue further highlights the predominance of fibrous structures that compose the adipose ECM.

1.3 In vitro analysis of topographical guidance

Attempts to study the cellular response to topographical cues in vitro began in 1912, when Harrison et al studied the guidance of embryonic cells with spider thread [34]. Paul Weiss subsequently pioneered the concept of "contact guidance" in the 30's-50's [35]. The same effects can be seen in i*n vitro* analyses that are able to control for exogenous variables. Research into nanofeature effects goes back to the 60's [36, 37]. Dalby et al has shown that fibroblasts can respond to nanopits 35 nm in diameter and nanoislands just 10 nm in height [38, 39]. The nanopit response is particularly impressive, as it shows an intrinsic sensitivity to subtle surface features, not just abrupt step changes in height. Numerous studies have shown that modulating the roughness of a surface at various length scales can likewise affect many aspects of cell function. Surface roughness

has been shown to affect cell adhesion and migration rate [40, 41]. Additionally, ECM-deposition were higher on surfaces sandblasted to have rougher surfaces [42]. Culturing osteoblasts upon titanium surfaces which had increased surface roughness through sandblasting and etching resulted in increased cell adhesion and proliferation [43]. The in vitro surface-roughening experiments are usually conducted on different surfaces than those used for tissue engineering, such as silicon substrates or metal surfaces. The same effects of Nanotopography can also be important on the materials used for in vivo applications, though; Zamani et al showed that increasing the surface roughness on PLGA nanofibers can influence cell adhesion and proliferation [44]. At the subcellular level, filopodia have been shown to respond to features as small as 35 nm-diameter nanopits and 10 nm-high nanoislands [38, 39].

The initial focus of synthetic topographies was using photolithography to etch grooves of varying shapes, such as square or v-shaped grooves [45, 46]. Additional methods employed include glancing angle deposition [47, 48], laser ablation [49, 50], microcontact printing and etching [51, 52], inkjet printing [53, 54], and electron-beam lithography [55-57]. Seeding endothelial cells upon a polymer cast of the native arterial ECM results in increased spreading and more natural cell morphology than smooth-surfaced alternatives [58].

The lithography-based groove experiments show that cells align along the long axis of the groove with corresponding alignment of the actin and cytoskeleton [18]. The depth of the groove has a strong effect on the cellular organization with increasing cell

alignment with increasing groove depth, as opposed to decreasing cellular alignment with increasing groove width [59]. When there are conflicting groove orientations, with minor grooves in the floor of major grooves but offset 54° from the major groove axis, the cells orient along the major groove axis, though the cells show the propensity to align along the minor grooves in the absence of major grooves [60]. Not all cell-types respond equally to alignment cues, however. In one study, 100% of fibroblasts align along 1μm grooves, but only 20% of macrophages and monocytes align with the underlying topography and no alignment at all is seen in keratinocytes or neutrophils [61]. Cell types that must rely upon cues from the microenvironment to either migrate to the proper location or align themselves for proper function (such as cardiomyocytes) may inherently respond more strongly to topographic cues.

1.4 Nanofiber-based topographical guidance

Electrospinning, then known as "electrostatic spinning" first appeared in a patent application back in 1934 [62]. Research into the use of electrospun fibers began in earnest in the 1990's and has grown exponentially since, with 2,110 electrospinning articles listed on Web of Science for the year 2014 alone. Electrospinning is the process wherein a polymeric material is dissolved in a solvent. A large voltage is applied to the solution, which induces the formation of a fluid jet. The charge-charge repulsion at the jet surface drives a uniaxial stretching of the fluid stream, continuously reducing the fluid diameter as the solvent evaporates until it reaches a grounded target [63]. The Initial, coherent stream is called the Taylor cone, where the surface tension is sufficient to

maintain a stable steam. This eventually gives way to an instable regime called the plume, where the charge-charge repulsion term dominates the surface tension due to its decreased cross-sectional area. The fiber stream whips wildly and rapidly reduces the fiber diameter further. The result is the rapid generation of long, nonwoven solid polymeric fibers with uniform diameters. Fibers can be produced in the range of tens of nanometers up to several microns in aligned or random orientations. The fibers can be produced from numerous synthetic polymers such as PCL, PLA, or PES as well as biological sources such as collagen or chitosan.

Nanofibers can also affect cell fate by mimicking the topographical cues in the native ECM. Chua et al demonstrated that surface-aminated PES nanofibers were able to mimic key features of the native hematopoietic niche, allowing for greatly increased expansion of cell numbers through increased proliferation and maintenance of stemness [64]. This phenomenon of fibers effecting cell fate is also seen in the use of PES nanofibers to guide neural stem cell (NSC) differentiation. Christopherson et al seeded NSCs onto random meshes of electrospun fibers of various diameters [65]. The geometry of the fibers restricted the NSCs to certain geometries, with the smaller 283 nm fibers allowing the cells to take on a spread-out cell morphology with lots of radiating cell processes, which lead to higher frequency of differentiation into oligodendrocytes, which have a similar morphology. In contrast, the NSCs seeded upon the larger 749 nm and 1452 nm nanofibers were forced into an elongated morphology by being able to associate with only one or two fibers and correspondingly differentiating at a higher frequency into neuronal cells with a similar geometry. Our lab has also previously demonstrated that

larger aligned nanofibers can help efficiently differentiate neural crest stem cells into Schwann cells [66].

Another mechanism of action for topographical features is if the substrate geometry recapitulates the cell's native environment in a key way. For example, Oligodendrocytes are the supportive, myelinating cells of the central nervous system. Lee et al seeded oligodendrocyte precursor cells (OPCs) onto electrospun polystyrene fibers with diameters ranging from 200 nm to 4 μm [67]. Even before differentiation, the OPCs preferentially attached to and ensheathed the larger fibers above 4 μm in diameter. Upon differentiation into mature oligodendrocytes, the majority of the cells (60%) ensheathed fibers with diameters from 2 – 4 μm, while only 5% of cells ensheathed fibers from 300-400 nm, and no cells ensheathed fibers under 300 nm. The diameter dependence of the oligodendrocyte-fiber ensheathment recapitulates the native oligodendrocyte function, wherein larger axons are preferentially myelinated over smaller axons [33].

1.5 Development of nanofiber matrices for in vitro and in vivo applications

1.5.1 Description of electrospinning apparatus and methodology

A modified version of the electrospinning setup was used for this study (Fig. 1.2). The nanofiber-solvent solution is added to a 1 mL plastic syringe (with a plastic plunger not rubber to prevent leaching of plasticizer from the plunger). A flat-edged syringe

needle (27 gauge unless otherwise specified) is added to the syringe, and the syringe is placed inside a syringe pump (KD Scientific, Holliston, MA). The syringe pump is mounted upon a linear stage (Newmark Systems, Rancho Santa Margarita, CA) to allow for controllable rastering over the area of interest. A DC power supply (Gamma High Voltage power supply, Ormond Beach FL) is used to generate a positive charge onto the tip of the syringe needle with an alligator clip or metal wire loop. A Dayton DC Speed Control controls the rotation speed of the wheel, which was verified with a non-contact tachometer (Fisher Scientific). The syringe pump is aimed at the face of a large wheel 40 cm in diameter. The fiber sheets or coverslips are spun on the outer third of the wheel face to minimize curvature of the fibers. The syringe pump is then rastered back and forth across the desired area, with more passes and/or slower speeds corresponding with thicker layers of aligned fibers.

1.6 Nanofiber production capabilities

By varying the nanofiber parameters (Table 1.1), we were able to create highly aligned fibers with different fiber diameters from 180 nm to 8 microns, as seen in Fig. 1.3. The PCL molecular weight and concentration were the most important factors in determining the nanofiber diameter. Lowering the viscosity of the solution through either reduced polymer molecular weight or through lower concentrations resulted in smaller diameter fibers. Additional charge carriers, such as the inclusion of a small percentage of PBS could also be introduced to reduce the fiber diameter. Finally, increasing the positive voltage decreased the fiber diameter by increasing the charge-charge repulsion, resulting

in a faster whip speed and smaller fibers. To obtain excellent alignment, the wheel rotation had to be adjusted such that the tangential speed of the wheel surface is slightly faster than the instantaneous whip speed of the fiber jet, such that the fibers are dragged slightly into alignment. A faster rotation will result in snapped fibers, while a slower rotation results in poor alignment. Solutions with higher whip speeds (either lower viscosity or higher voltages) require higher rotation speeds to obtain good alignment. Solvent choice can also affect the fiber diameter, as 100% chloroform produced better alignment and more reproducible diameters in fibers above a micron, while a 90% DCM/ 10% DMF blend produced better fibers under a micron in diameter. The DCM/DMF solvent fibers had a smooth surface morphology, while the chloroform-solvent fibers generally had a rougher surface morphology. Polycaprolactone (PCL) was chosen as our standard electrospinning polymer for several reasons. PCL is a biodegradable polymer that eventually is fully bioresorbed without production of toxic or acidic degradation products [68]. It has excellent rheological properties that can be tuned with the choice of the molecular weight. It is simple to synthesize and is available in clinical-grade forms. PCL also has a long history of successful use in medical devices.

1.7 Nanofiber matrix as an in vitro cell culture platform

We were able to expand the utility of this spinning ability by spinning fibers into a number of configurations. For cell culturing experiments, the nanofibers were spun onto glass coverslips for easy placement into 24well tissue culture plates. For example, we used highly aligned 650nm PCL nanofibers for culturing human pluripotent stem cell-

derived neurons. Our collaborator Dr. Jean-Philippe Richard studies the mechanisms underpinning ALS with a particular focus upon the neuronal function in this disease. Motor neurons are derived from iPS cells from ALS patients to compare with similar neurons from healthy patients to better pinpoint the source of the pathology. Neurite extension is the particular variable of interest in the study in order to better understand the differences that arise in ALS. Problematically, the neurons do not adhere and grow as single cells when cultured on standard TCPS, but rather form clumps that make the analysis of neurites very difficult, since the neurites thus grow on top of one another and make it impossible to identify the soma for a given neurite. When cultured on 650 nm aligned PCL nanofibers, however, the neurons adhered readily as single-cells with their neurites extending along the aligned nanofibers, easing quantification (Fig. 1.4).

The fibers were more easily incorporated into implantable scaffolds when they were made into larger sheets that had the strength to be manipulated by hand. We were able to generate more exotic configurations of fibers, such as mixed topographical coverslips that could simultaneously present cells with two different topographic cues (Fig. 1.5). We also created coverslips for our collaborator Dr. Ted Dawson's that recapitulated the geometry of cortical neuron migration and differentiation, wherein neuronal precursors migrated out radially in progressive waves, resulting in a layered structure that determined the differentiation of the cortical neuron. These coverslips have a central, randomly aligned nanofiber region from which radially aligned nanofibers emerge and sweep towards the coverslip periphery (Fig. 1.6). The neuronal precursors

can be seeded upon the inner, random fiber region. They can then migrate outwards to theoretically generate similar layers of different cortical neurons as seen in the brain.

1.8 Degradable PCL-gelatin fibers

While PCL is an excellent candidate polymer for nanofibers for tissue engineering, there are scenarios wherein the fibers would degrade more quickly than the 18months or more of PCL. In particular, quicker-degrading fibers may be useful in scenarios such as that seen in our lab's previous work with nanofibers with adhesive cues. Lim et al discovered an "oasis effect" wherein the strong adhesion cue on the nanofibers encouraged migration into the nerve guide and across the nerve guide, but inhibited the regenerating nerve from being able to leave the nerve guide to enter the distal nerve stump. The PCL nanofibers had been modified to present laminin on the fiber surface as an adhesive cue or heparin (which would thus present endogenous growth factors on the fiber surface). This is a physical analogue to the "candy-store effect" commonly seen in the CNS, wherein high concentrations of growth factors within the treatment area inhibit migration towards the distal target. The regenerating nerve had a higher number of myelinated axons and a higher nerve area within the conduit midpoint than the Neuragen control, yet poorer functional regeneration and fewer myelinated axons within the distal, tibial nerve. If the adhesive cue degraded over the course of weeks instead of years, the fibers could serve as an excellent guidance cue across the nerve guide before degrading and thus allowing successful reinnervation of the distal stump. We chose to blend in gelatin to the PCL nanofibers during electrospinning to increase the degradation rate of

the fibers. We have created nanofibers wherein gelatin forms 0%, 50%, 70%, 80%, 90%, and 100% of the mass, as compared to PCL. The gelatin was crosslinked via glutaraldehyde vapor in ethanol. Ethanol was used as the glutaraldehyde carrier during crosslinking because when water was the carrier, the water vapor dissolved the gelatin fibers together before they had been sufficiently crosslinked by the glutaraldehyde. To determine the structure and degradation properties of the nanofibers, we have tested the degradation rate of the fibers both in accelerated *in vitro* conditions, and *in vivo* conditions. To accelerate the degradation in vitro, we selectively add *pseudomonas* lipase to degrade the PCL, and collagenase to degrade the gelatin. To most-closely approximate the degradation conditions the nanofibers will experience within the conduit, we created tubes composed of the nanofibers and implanted them into the rats, immediately neighboring the sciatic nerve. The composition of the nanofibers had a large impact upon the degradation rate. The 100% gelatin fibers were severely degraded within 2 weeks and completely gone within 4 weeks, too quickly for use in nerve guides. Meanwhile, the 50%/50% Gelatin-PCL fibers were still present in fibrous form (Fig. 1.7) with no apparent mass loss after 8 weeks i*n vivo* (Fig. 1.8). Thus, we explored three intermediate compositions of 70% gelatin, 80% gelatin, and 90% gelatin. The 90% gelatin group degraded almost as quickly as the 100% gelatin group, being almost entirely degraded by mass-basis at 2 weeks. The 80% gelatin group, however, had lost significant mass (62%) within two weeks, but still was present at 4 and 8 weeks. The 70% gelatin group did not have any apparent mass loss through the first 4 weeks of the study, but lost 15% of its mass by week 8, showing significantly faster degradation than PCL alone.

1.9 Conclusion

These results demonstrate our capability to generate nanofiber constructs with properties tuned to elicit the desired biological response both *in vitro* and *in vivo*, with a particular focus on fiber diameter, alignment, composition, degradation rate, density, and surface properties.

1.10 Figures

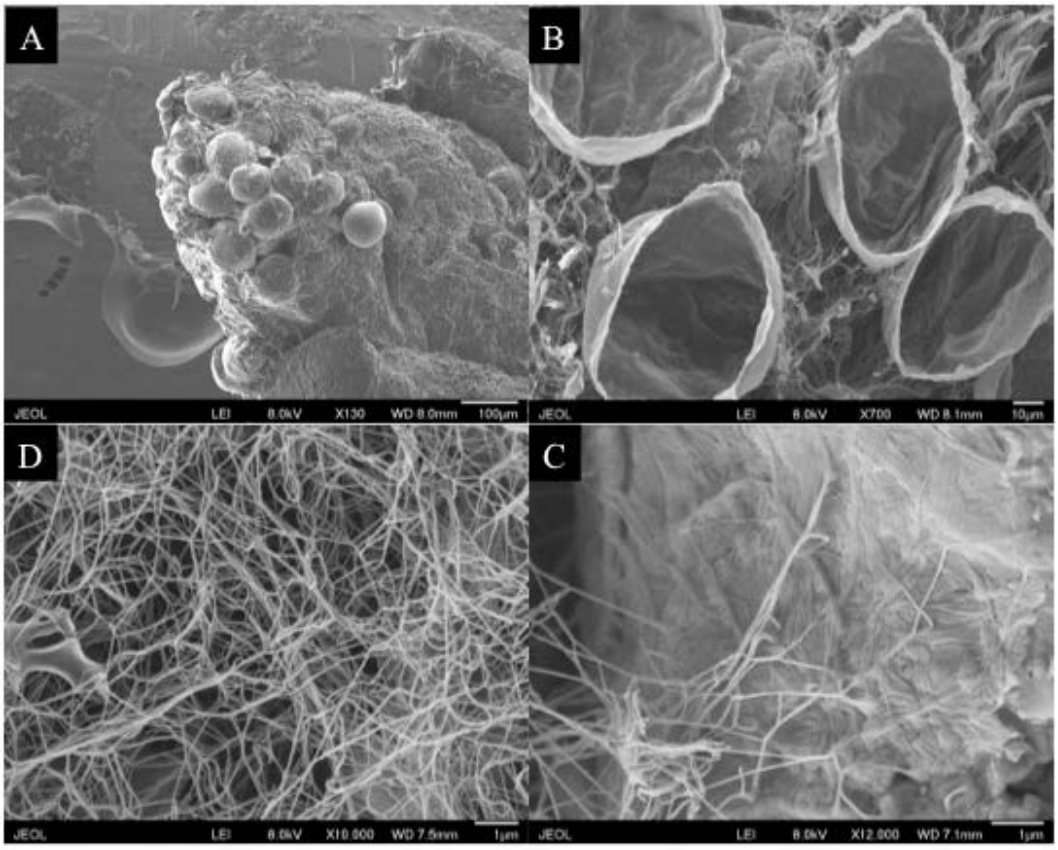

Figure 1-1: Nanotopography in adipose tissue.

SEM images of native fat tissue from a rat inguinal fat pad. A. Naïve adipose tissue. Note the large, spherical adipocytes. B. Delipidized, decellularized adipose tissue. Removing the lipids highlights the fibrillar nature of the surrounding ECM. C. Basement membrane of Delipidized, decellularized adipose tissue. Note the fibrillar structure to the membrane, with fibers emerging from the surface. D. Delipidized, decellularized adipose tissue after cryomilling. Note the predominance of fibrillar structures.

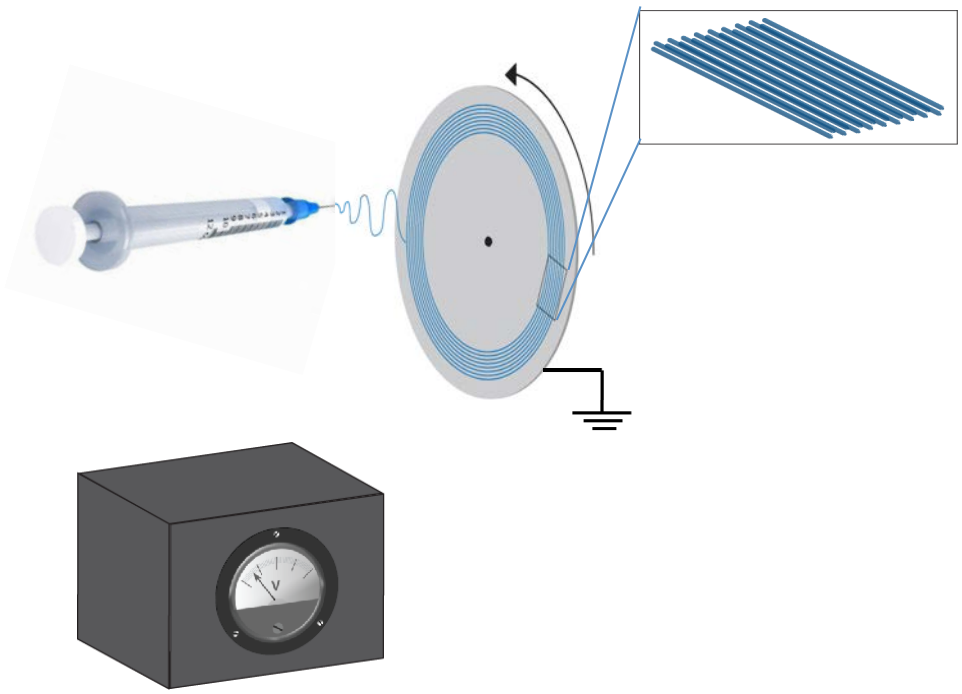

Figure 1-2: Electrospinning setup for producing aligned nanofibers

nm		cm	ml/hr	kV	rpm	gauge
goal size	Solution Composition	Separation	Flow Rate	Voltage	Rotation Speed	Needle
185	16% 95LMW-5HMW PCL in HFP	3.5	0.35	8	1820	32
325	16% 75LMW-25HMW PCL in HFP	3.5	0.35	8	1820	32
400	15% w/v PCL in HFP	6	0.25	10	1820	27
450	16% w/v PCL in HFP	4.5	0.25	10	1800	27
500	15% w/v PCL in HFP	3.5	0.25	7	1800	32
525	17.5% w/v PCL in HFP	4	0.25	10	1800	27
625	17.5% w/v PCL in HFP	4	0.35	7	1100	27
675	17.5% w/v PCL in HFP	3	0.35	9	1100	27
750	17.5% w/v PCL in HFP	4.2	0.35	7	1100	32
850	20%w/v PCL in 90HFP-10DCM	5	0.6	8.5	1300	27
950	20%w/v PCL in HFP	6	0.6	6.8	1300	27
1050	11%w/w PCL in Chloroform	8	0.35	7.5	750	27
1150	12%w/w PCL in Chloroform	8	0.35	7.5	750	27
1250	12%w/w PCL in Chloroform	4	0.6	8	750	27
1325	12%w/w PCL in Chloroform	8	0.6	8	750	27
1500	13% w/w PCL in Chloroform	8	0.6	8	750	27
1850	13% w/w PCL in Chloroform	15.5	0.6	8	600	27
2000	13% w/w PCL in Chloroform	15.5	0.6	8	600	27
2300	15% w/w PCL in DCM	7	2	9.3	750	21
2400	13% w/w PCL in Chloroform	15.5	1.5	9	40	27
2500	15% PCL w/w in DCM	10	3	11	750	21
2600	15% PCL w/w in DCM	7	2.5	9	750	21
2900	15% PCL w/w in DCM	10	2	10	750	21
3000	15% PCL w/w in DCM	10	3	11	1200	21
3200	15% PCL w/w in DCM	10	3	11	100	21
5500	15% w/w PCL in Chloroform	17	2	8.9	100	27
6000	15% w/w PCL in Chloroform	20+	1.25	8.9	100	27
8000	15% w/w PCL in Chloroform	20+	1.25	8.9	100	27

Table 1.1. Electrospinning parameters to produce aligned nanofibers of varying diameters

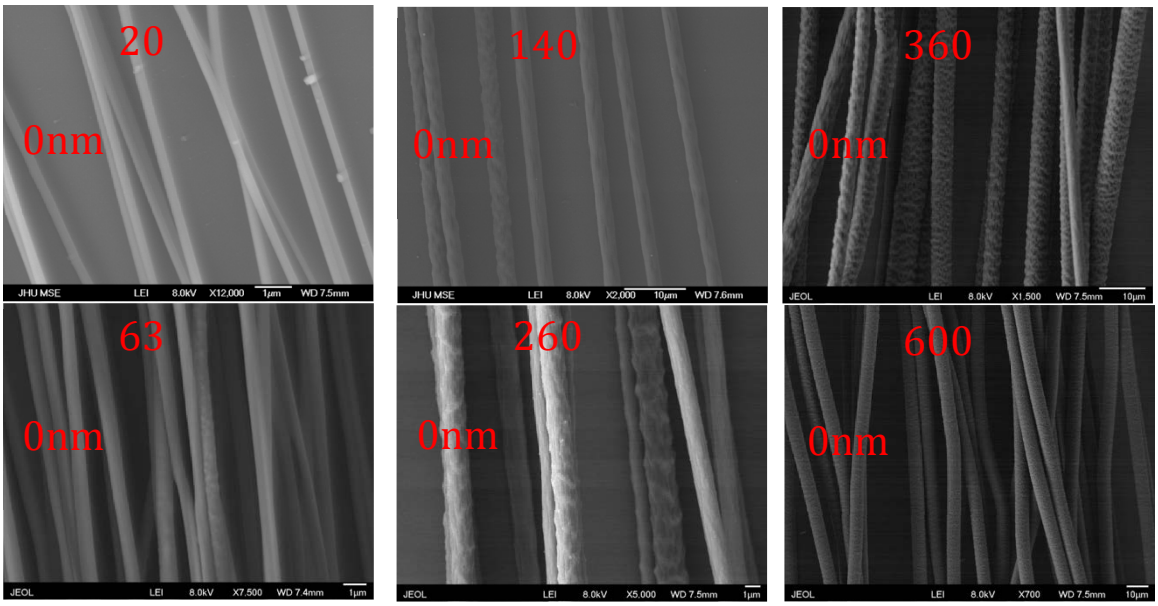

Figure 1-3: Aligned PCL nanofibers produced with the parameters given in Table 1.

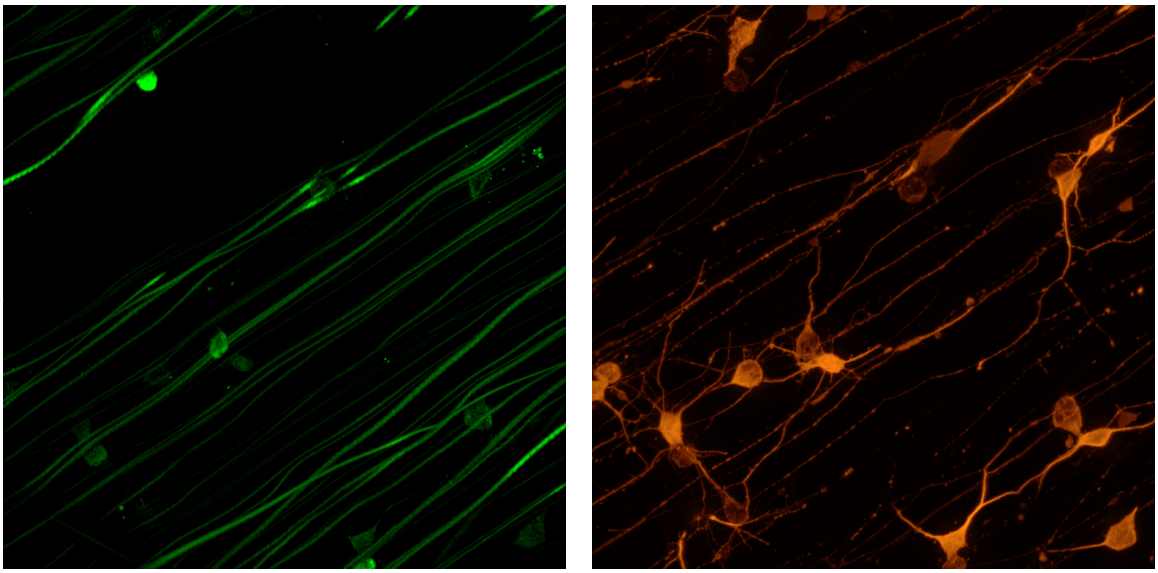

Figure 1-4: iPS-derived motor neurons cultured upon aligned 650nm PCL nanofibers.

Green: neuronal GFP. Red: motor microtubule marker MAP2. Note the aligned axonal extension and the neurons adhered as single-cells

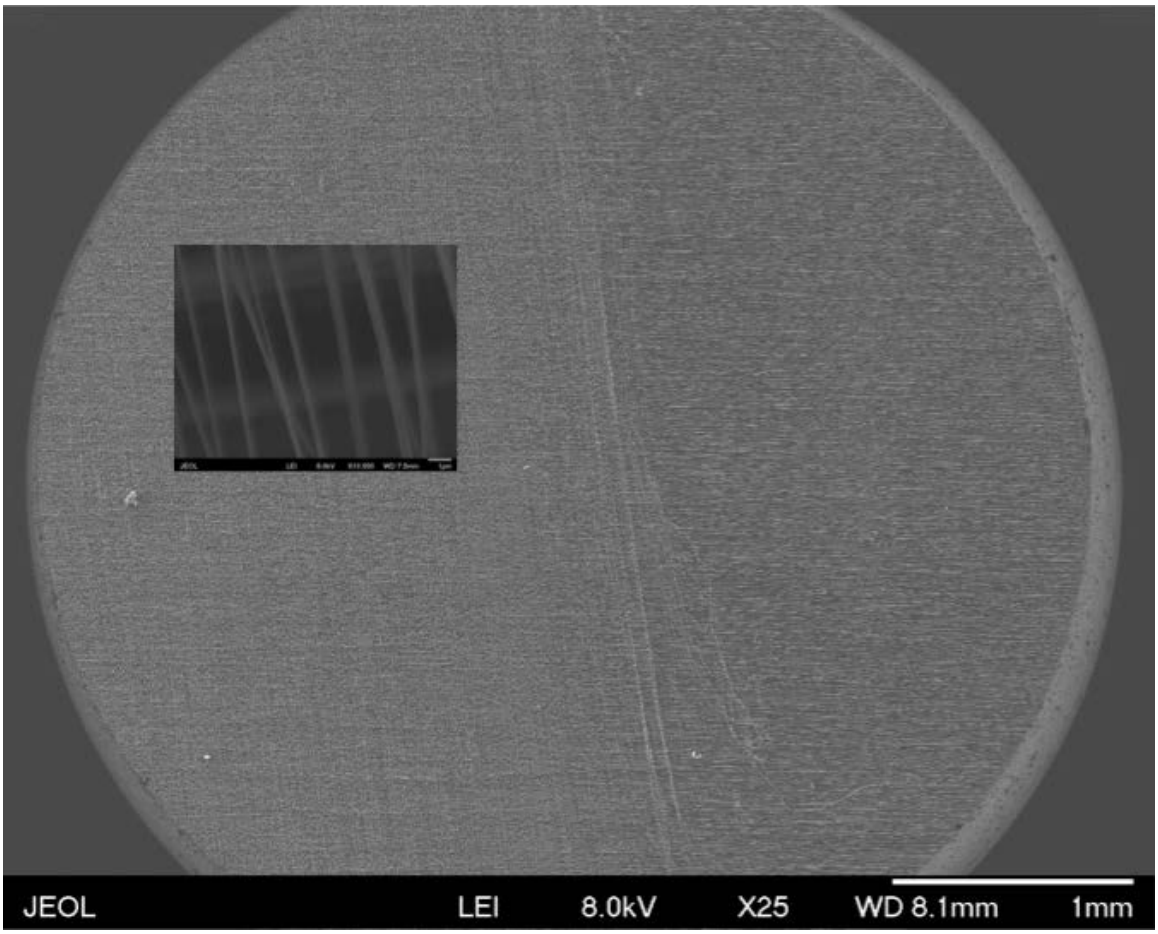

Figure 1-5: Mixed topography coverslips for cell studies.

Aligned 200nm fibers were overlaid off axis upon larger, aligned nanofibers. This allows for studying differential cell response to fiber diameters on the same coverslip

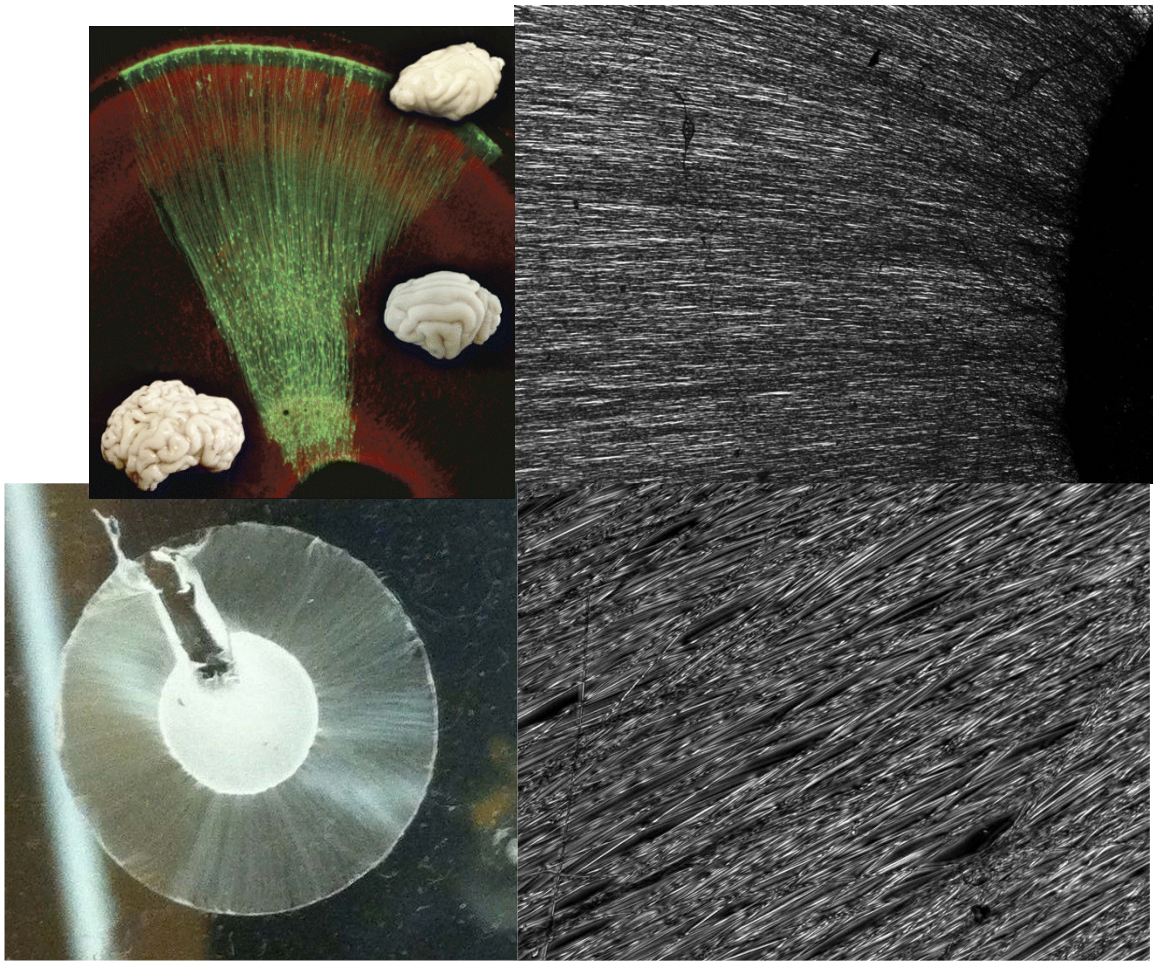

Figure 1-6: Radial coverslips to recapitulate the geometry of cortical neuron migration and differentiation.

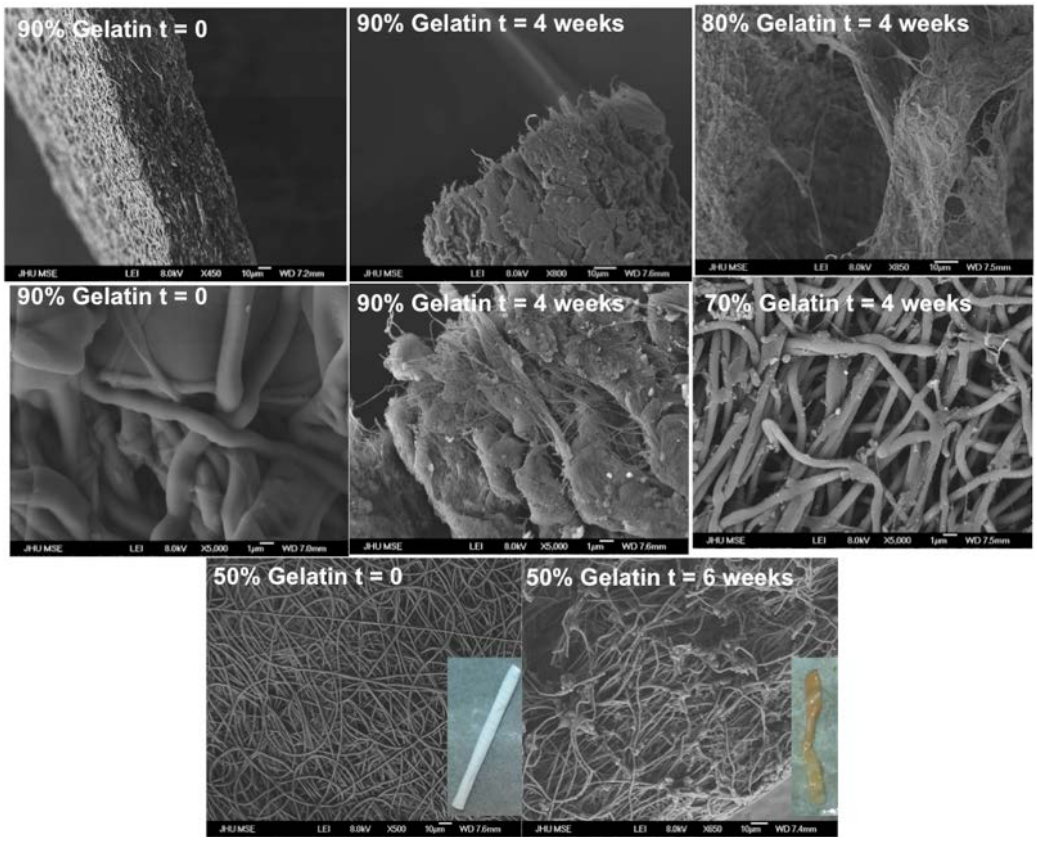

Figure 1-7: Nanofiber tubes with different degradation rates after implantation in vivo.

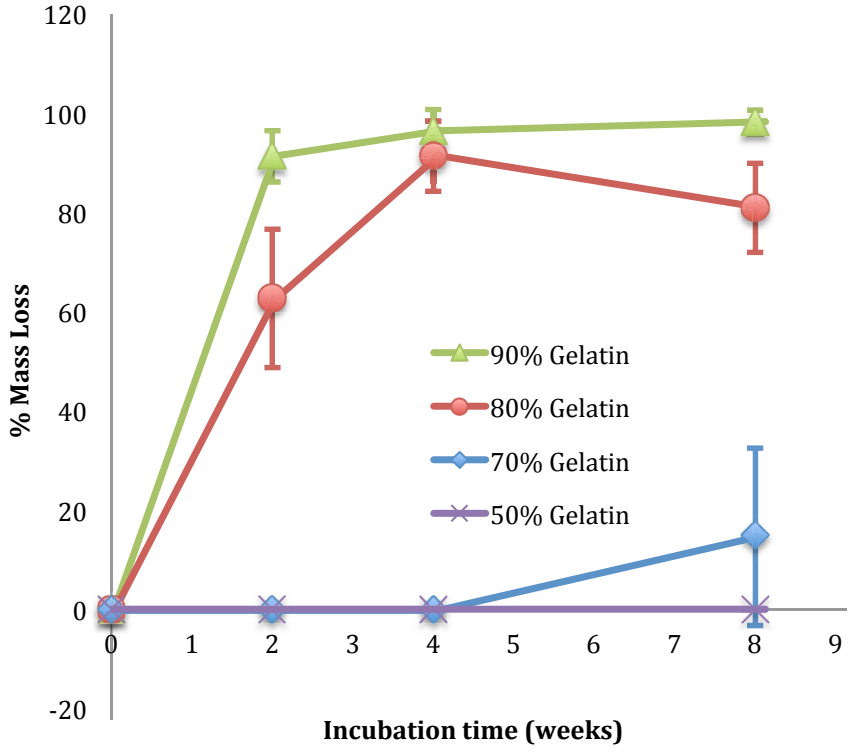

Figure 1-8: Quantification of mass loss of degradable fibers after implantation near the sciatic nerve in a rat.

1.11 References

1. Nerem, R.M. and A. Sambanis, *Tissue engineering: from biology to biological substitutes.*, in *Tissue Engineering*. 1995. p. 3-13.
2. Harrison, R.H., J.-P. St-Pierre, and M.M. Stevens, *Tissue engineering and regenerative medicine: a year in review.* Tissue Engineering Part B: Reviews, 2014. **20**(1): p. 1-16.
3. Lin, X., et al., *Tissue engineering and regenerative medicine in applied research: a year in review of 2014.* Tissue Engineering Part B: Reviews, 2015. **21**(2): p. 177-186.
4. Han, Y.L., et al., *Engineering physical microenvironment for stem cell based regenerative medicine.* Drug discovery today, 2014. **19**(6): p. 763-773.
5. Heino, J., *The collagen family members as cell adhesion proteins*, in *Bioessays*. 2007. p. 1001-1010.
6. Chen, P., M. Cescon, and P. Bonaldo, *The role of collagens in peripheral nerve myelination and function.* Molecular neurobiology, 2014: p. 1-10.
7. Coopman, P.J., et al., *Influence of basement membrane molecules on directional migration of human breast cell lines in vitro.*, in *J. Cell. Sci.* 1991. p. 395-401.
8. Darnell, J., H. Lodish, and D. Baltimore, *Multicellularity: cell—cell and cell—matrix interactions*, in *Molecular Cell Biology. New York: Scientific American Books Inc*. 1990. p. 903-951.
9. Carnegie, J.A. and O. Cabaca, *Extracellular matrix composition and resilience: two parameters that influence the in vitro migration and morphology of rat inner cell mass-derived cells.*, in *Biol. Reprod.* 1993. p. 287-299.
10. Gause, I., W.N. Sivak, and K.G. Marra, *The Role of Chondroitinase as an Adjuvant to Peripheral Nerve Repair.* Cells Tissues Organs, 2014. **200**(1).
11. Dua, H.S., J.A. Gomes, and A. Singh, *Corneal epithelial wound healing.*, in *Br J Ophthalmol*. 1994. p. 401-408.
12. Juliano, R.L. and S. Haskill, *Signal transduction from the extracellular matrix.*, in *The Journal of Cell Biology*. 1993. p. 577-585.
13. Mousa, S.A. and D.A. Cheresh, *Recent advances in cell adhesion molecules and extracellular matrix proteins: potential clinical implications*, in *Drug Discov. Today*. 1997. p. 187-199.
14. Chen, C.S., et al., *Geometric control of cell life and death.*, in *Science*. 1997. p. 1425-1428.
15. Clark, E.A. and J.S. Brugge, *Integrins and signal transduction pathways: the road taken.*, in *Science*. 1995. p. 233-239.
16. Hynes, R.O., *Integrins: versatility, modulation, and signaling in cell adhesion.*, in *Cell*. 1992. p. 11-25.
17. Ruoslahti, E., *Stretching is good for a cell.*, in *Science*. 1997. p. 1345-1346.
18. Flemming, R.G., et al., *Effects of synthetic micro- and nano-structured surfaces on cell behavior.*, in *Biomaterials*. 1999. p. 573-588.
19. Abrams, G., et al. *Nanoscale topography of the extracellular matrix underlying the corneal epithelium of the non-human primate*. in *Investigative Ophthalmology & Visual Science*. 1997.

20. Abrams, G.A., et al., *Nanoscale topography of the basement membrane underlying the corneal epithelium of the rhesus macaque*, in *Cell Tissue Res*. 1999. p. 39-46.
21. Shirato, I., et al., *Fine structure of the glomerular basement membrane of the rat kidney visualized by high-resolution scanning electron microscopy.*, in *Cell Tissue Res*. 1991. p. 1-10.
22. Hironaka, K., et al., *Renal basement membranes by ultrahigh resolution scanning electron microscopy.*, in *Kidney Int.* 1993. p. 334-345.
23. Trinkaus-Randall, V., et al., *Development of a biopolymeric keratoprosthetic material. Evaluation in vitro and in vivo.*, in *Invest. Ophthalmol. Vis. Sci.* 1988, The Association for Research in Vision and Ophthalmology. p. 393-400.
24. Watanabe, K., S. Nakagawa, and T. Nishida, *Stimulatory effects of fibronectin and EGF on migration of corneal epithelial cells*, in *Invest Ophthalmol Vis Sci*. 1987. p. 205-211.
25. Watanabe, K., S. Nakagawa, and T. Nishida, *Chemotactic and haptotactic activities of fibronectin for cultured rabbit corneal epithelial cells.*, in *Invest. Ophthalmol. Vis. Sci.* 1988. p. 572-577.
26. Reid, T.W., *Growth control of cornea and lens epithelial cells*, in *Progress in retinal and eye research*. 1994, Progress in retinal and eye research. p. 507-554.
27. Small, J.V., et al., *The lamellipodium: where motility begins*, in *Trends in Cell Biology*. 2002. p. 112-120.
28. Mattila, P.K. and P. Lappalainen, *Filopodia: molecular architecture and cellular functions*, in *Nat Rev Mol Cell Biol*. 2008. p. 446-454.
29. Galbraith, C.G., K.M. Yamada, and J.A. Galbraith, *Polymerizing actin fibers position integrins primed to probe for adhesion sites.*, in *Science*. 2007. p. 992-995.
30. Gallo, G. and P.C. Letourneau, *Regulation of growth cone actin filaments by guidance cues*, in *J. Neurobiol.* 2003. p. 92-102.
31. Carlsen, F. and F. Behse, *Three dimensional analysis of Schwann cells associated with unmyelinated nerve fibres in human sural nerve.*, in *J. Anat.* 1980. p. 545-557.
32. Gillespie, M.J. and R.B. Stein, *The relationship between axon diameter, myelin thickness and conduction velocity during atrophy of mammalian peripheral nerves.*, in *Brain Research*. 1983. p. 41-56.
33. Friede, R.L., *Control of myelin formation by axon caliber (with a model of the control mechanism).* in *J. Comp. Neurol.* 1972. p. 233-252.
34. Harrison, R.G., *The reaction of embryonic cells to solid structures*, in *Journal of Experimental Zoology*. 1914. p. 521-544.
35. Weiss, P., *Cell contact*, in *International review of cytology*. 1958, Elsevier. p. 391-423.
36. Rosenberg, M.D., *Long-range interactions between cell and substratum.*, in *Proc. Natl. Acad. Sci. U.S.A.* 1962. p. 1342-1349.
37. Rosenberg, M.D., *Cell guidance by alterations in monomolecular films.*, in *Science*. 1963. p. 411-412.

38. Dalby, M.J., et al., *Investigating filopodia sensing using arrays of defined nano-pits down to 35 nm diameter in size*, in *Int J Biochem Cell Biol*. 2004. p. 2005-2015.
39. Dalby, M., *Investigating the limits of filopodial sensing: a brief report using SEM to image the interaction between 10 nm high nano-topography and fibroblast filopodia*, in *Cell Biology International*. 2004. p. 229-236.
40. Martin, J.Y., et al., *Effect of titanium surface roughness on proliferation, differentiation, and protein synthesis of human osteoblast-like cells (MG63).* in *J. Biomed. Mater. Res.* 1995. p. 389-401.
41. Lampin, M., et al., *Correlation between substratum roughness and wettability, cell adhesion, and cell migration.*, in *J. Biomed. Mater. Res.* 1997. p. 99-108.
42. Groessner-Schreiber, B. and R.S. Tuan, *Enhanced extracellular matrix production and mineralization by osteoblasts cultured on titanium surfaces in vitro.*, in *J. Cell. Sci.* 1992. p. 209-217.
43. Rosales-Leal, J., et al., *Effect of roughness, wettability and morphology of engineered titanium surfaces on osteoblast-like cell adhesion.* Colloids and surfaces A: Physicochemical and Engineering aspects, 2010. **365**(1): p. 222-229.
44. Zamani, F., et al., *The influence of surface nanoroughness of electrospun PLGA nanofibrous scaffold on nerve cell adhesion and proliferation.* Journal of Materials Science: Materials in Medicine, 2013. **24**(6): p. 1551-1560.
45. Madou, M.J., *Fundamentals of Microfabrication (CRC, Boca Raton, FL)*. 1997.
46. Thompson, L.F., C.G. Willson, and M.J. Bowden, *Introduction to Microlithography, 1994*, in *Washington, DC: ACS*. 1994.
47. Robbie, K. and M. Brett, *Sculptured thin films and glancing angle deposition: Growth mechanics and applications.* Journal of Vacuum Science & Technology A, 1997. **15**(3): p. 1460-1465.
48. Robbie, K., J. Sit, and M. Brett, *Advanced techniques for glancing angle deposition.* Journal of Vacuum Science & Technology B, 1998. **16**(3): p. 1115-1122.
49. Phillips, H.M. and R.A. Sauerbrey, *Excimer-laser-produced nanostructures in polymers*, in *Optical Engineering*. 1993, International Society for Optics and Photonics. p. 2424-2436.
50. Schleicher, B. and S.K. Friedlander, *Characterization of nanostructured carbon microwires fabricated by an aerosol process*, in *Journal of applied physics*. 1995, AIP Publishing. p. 6046-6049.
51. Xia, Y., et al., *Microcontact printing of alkanethiols on copper and its application in microfabrication*, in *Chemistry of materials*. 1996, ACS Publications. p. 601-603.
52. Xia, Y., E. Kim, and G.M. Whitesides, *Microcontact printing of alkanethiols on silver and its application in microfabrication*, in *Journal of the Electrochemical Society*. 1996, The Electrochemical Society. p. 1070-1079.
53. Blanchard, A.P., R.J. Kaiser, and L.E. Hood, *High-density oligonucleotide arrays*, in *Biosens Bioelectron*. 1996, Elsevier. p. 687-690.

54. Giordano, R.A., et al., *Mechanical properties of dense polylactic acid structures fabricated by three dimensional printing*, in *Journal of Biomaterials Science, Polymer Edition*. 1997, Taylor & Francis. p. 63-75.
55. Gold, J. and B. Kasemo, *Morphological and chemical characterization of microfabricated fibres for biological applications*, in *J Mater Sci-Mater M*. 1997, Springer. p. 251-263.
56. Gold, J., B. Nilsson, and B. Kasemo, *Microfabricated metal and oxide fibers for biological applications*, in *Journal of Vacuum Science & Technology A*. 1995, AVS: Science & Technology of Materials, Interfaces, and Processing. p. 2638-2643.
57. Terris, B.D., et al., *Nanoscale replication for scanning probe data storage*, in *Applied Physics Letters*. 1996, AIP Publishing. p. 4262-4264.
58. Goodman, S.L., P.A. Sims, and R.M. Albrecht, *Three-dimensional extracellular matrix textured biomaterials.*, in *Biomaterials*. 1996. p. 2087-2095.
59. Dunn, G.A. and A.F. Brown, *Alignment of fibroblasts on grooved surfaces described by a simple geometric transformation.*, in *J. Cell. Sci.* 1986. p. 313-340.
60. Brunette, D.M., *Fibroblasts on micromachined substrata orient hierarchically to grooves of different dimensions.*, in *Experimental cell research*. 1986. p. 11-26.
61. Meyle, J., K. Gültig, and W. Nisch, *Variation in contact guidance by human cells on a microstructured surface.*, in *J. Biomed. Mater. Res.* 1995. p. 81-88.
62. Li, D. and Y. Xia, *Electrospinning of nanofibers: Reinventing the wheel?*, in *Advanced Materials*. 2004. p. 1151-1170.
63. Pham, Q.P., U. Sharma, and A.G. Mikos, *Electrospinning of polymeric nanofibers for tissue engineering applications: a review.*, in *Tissue Engineering*. 2006. p. 1197-1211.
64. Chua, K.-N., et al., *Surface-aminated electrospun nanofibers enhance adhesion and expansion of human umbilical cord blood hematopoietic stem/progenitor cells.* Biomaterials, 2006. **27**(36): p. 6043-6051.
65. Christopherson, G.T., H. Song, and H.-Q. Mao, *The influence of fiber diameter of electrospun substrates on neural stem cell differentiation and proliferation*, in *Biomaterials*. 2009, Elsevier Ltd. p. 556-564.
66. Ren, Y.-J., et al., *Enhanced differentiation of human neural crest stem cells towards the Schwann cell lineage by aligned electrospun fiber matrix.*, in *Acta Biomaterialia*. 2013.
67. Lee, S., et al., *A culture system to study oligodendrocyte myelination processes using engineered nanofibers*, in *Nat Meth*. 2012. p. 917-922.
68. Woodruff, M.A. and D.W. Hutmacher, *The return of a forgotten polymer—polycaprolactone in the 21st century.* Progress in Polymer Science, 2010. **35**(10): p. 1217-1256.

Chapter 2 In Vitro Analysis of Schwann Cell Migration on Aligned Nanofibers

2.1 Background

2.1.1 Role of Schwann cells in peripheral nerve repair

Schwann cells derive from the neural crest via an intermediate cell type, the Schwann cell precursor [1]. They are potent regulators in the peripheral nervous system, organizing the axonal architecture, modulating the axonal caliber and function, and directing the organization of the peripheral nerve sheath [2]. Mature Schwann cells ensheath and myelinate individual large axons, while adult non-myelinating Schwann cells wrap around multiple, smaller axons, without myelination. Schwann cells, as opposed to Schwann cell precursors, are able to survive the loss of the associated axon after injury through autocrine signaling loops, particularly NT-3 and PDGF-BB. The axotomized Schwann cells are able to de-differentiate, proliferate, phagocytize the myelin debris (along with macrophages) [3, 4]. The Schwann cells can then produce neurotrophic factors and adhesion molecules to attract and support the regenerating axons, and form bands of Buengner to physically guide the regenerating axons [3, 5]. Following reinnervation, the Schwann cells are then capable of maturing anew into myelinating and non-myelinating phenotypes [6]. The key role of Schwann cells in the regenerative process can be seen in how the mechanism for poor functional recovery after chronic denervation is not intrinsic to the axons, but rather the death of distal Schwann cells [7-9].

Physically, the Schwann cell basal lamina is predominantly laminin-2 with smaller amounts of laminin 1 and plays an important factor in myelination [10-12]. Integrins modulate the Schwann cell function; for example, α6β1 is necessary for myelination to proceed [13]. Blocking β1 prevents myelination on laminin 1 or laminin 2 substrates, and RGD peptides block migration on fibronectin substrates [14]. These integrins allow Schwann cells to respond to numerous ligands to direct migration and instigate myelination. There is a complex interplay between axons and Schwann cells, with extensive signaling from both axons to Schwann cells and Schwann cells to axons [15]. One main component of our nerve guide design philosophy is to design our nerve guides specifically to optimize the interactions with Schwann cells. Previous studies have shown that Schwann cells can migrate into an acellular nerve graft from both nerve stumps, with Schwann cells throughout the 10mm graft by 10 days, followed later by the regenerating axons [16]. We would like to develop synthetic scaffolds that can induce more Schwann cells to migrate faster to better populate larger scaffolds. Our goal is to provide a scaffold that quickly enables Schwann cell migration into and across the nerve guide such that there is a dense population of Schwann cells in place for guiding and supporting the regenerating axons [17]. After the axons have bridged the nerve guide, the Schwann cells should be encouraged to mature and myelinate the axons to enable functional recovery of the distal motor targets. This chapter focuses on our in vitro work to develop guidance cues to efficiently direct the native Schwann cells into and across our synthetic nerve guides. While our lab is also exploring the use of gradients of growth factors like GDNF to provide guidance cues, this chapter focuses upon optimizing

topographical guidance to increase the migration distance and orientation of Schwann cells [18].

2.1.2 Previous studies into the migration of Schwann cells on nanofibers

There have been several previous studies that have either used nanofibers in peripheral nerve guides or attempted to study the mechanisms. Unfortunately, the current studies offer relatively little predictive power for determining the optimal fiber properties due to the conflicting results between the studies and other differences between their experimental setups and our intended use in nerve guides. Regan et al only saw an improvement of Schwann cell migration out of DRGs on nanofibers when cell proliferation was blocked and saw the axons precede the Schwann cells; this conflicts with other papers, however, and may be a function of their coating protocol [19]. Daud et al compared the effects of 1, 5, and 8 μm aligned fibers upon the migration of Schwann cells, neuronal cells, and DRG explants [20]. In this study, neurites extended furthest along 8 μm fibers when cultured alone, while Schwann cells migrated furthest along 1 μm fibers. When co-cultured, the axons never migrated beyond the Schwann cells, using the Schwann cell basal lamina as the guidance cue instead of the underlying fibers. However, this study did not compare migration upon fibers smaller than 1 μm to determine further improvement. Additionally, the fibers were used at a low density suspended in the media, which constrains the cells to narrower geometries than when the cells can interact with several layers of aligned fibers, as would be the case in our nerve guides. Tonazzini et al studied the effects of contact versus boundary guidance [21]. Jha

et al prepared bundles of aligned nanofibers by utilizing two pole air gap electrospinning [22]. They compared bundles of 383 nm, 906 nm, and 1667 nm nanofibers. In these scaffolds, DRG axons extended along individual nanofibers in the 383 nm group, but rather interacted more heavily with one another in the 1667 nm group, forming fascicle bundles of axons. The axons extended in close association with the interstitial fibroblasts and Schwann cells from the DRG. However, the spinning conditions also varied the alignment, amount of fiber-beading, porosity and mechanical properties of the constructs as well. Wang et al studied the migration of Schwann cells and the extension of axons from DRG explants grown on aligned nanofibers over 5 days [23]. They found that neurites extended similarly on 1325 nm and 759 nm PLLA fibers, but slower on 293 nm fibers. Schwann cells migrated progressively faster with increasing fiber diameter, migrating much faster on the 1325 nm versus 293 nm fibers. In another study, Jiang et al compared nerve regeneration using 251 nm aligned fibers as a topographical cue versus 981 nm fibers [24]. The smaller fibers resulted in significantly better overall nerve regeneration, with a higher total of myelinated axons and better functional recovery when measured with electrophysiology (CMAP amplitude). However, the fiber diameter may have effected the regeneration by means other than topographical guidance. The microfiber conduits were mechanically weaker than the nanofiber conduits and lacked a cell-impermeable layer to prevent infiltration of fibroblasts and macrophages from the surrounding tissue.

These studies offer some clues as to how to choose nanofiber properties for peripheral nerve repair, but often with specific methodologies that would not translate to our in vivo model. Moreover, the different studies often give conflicting results as to the

ideal size. To obtain a clear understanding of which nanofiber diameter is ideal for our intended use, we must perform our own analysis.

2.2 Methods

2.2.1 Plate preparation

Nanofiber coverslips were prepared via the parameters and instrumentation described in Chapter 1. The coverslips were sterilized via either 40min exposure to UV in the biosafety hood or ethylene oxide sterilization. The coverslips were glued to the bottom of the 24-well plates with Factor 2 silicone surgical glue, which was allowed to vent overnight to remove residual solvent. The coverslips were then washed with PBS and coated for cell adhesion by soaking in 1/100 Matrigel solution overnight at 37°C, unless otherwise stated. The coverslips were washed the following day with PBS and were equilibrated for 1 hour at 37°C with the cell media prior to adding the spheroids or single cells for live cell tracking.

2.2.2 Live-cell tracking

Fetal-derived primary human Schwann cells were purchased from Sciencell (Carlsbad, CA). The Schwann cells were seeded for two days prior to experiment and exposed to 1 μg/mL Hoechst 33342 (Pierce) for 30 minutes prior to use. Cells were washed to remove unused Hoechst, were trypsinized, resuspended in cell solution, and pipetted at about 1000 cells per well onto each coverslip and allowed to adhere for 6 hours prior to cell tracking. Cell migration was observed every 10 minutes for 12 hours

using a live cell imaging microscope with programmable stage (Nikon) and environmental chamber (37°C, 5% CO2, and 100%RH). The migrations of individual cells were analyzed using custom MatLab code. The final live-cell tracking experiment was performed with a cytosolic GFP marker instead of the nuclear stain to better highlight the cell's interactions with the nanofibers.

2.2.3 Schwann cell spheroid culturing

Fetal-derived primary human Schwann cells (Sciencell cat# 1700, Carlsbad, CA) were transfected with lentivirus to express cytosolic eGFP. To form spheroids, the transfected cells were cultured in agarose molds prepared with the Microtissues (Providence, RI) 24-35 molds. Each agarose mold fits into a well in a 24-well plate and has 35 recesses that are approximately 800 μm in diameter and 800 μm in depth to collect the cells and form spheroids. 75 μL of the cell suspension (1x10^6 cells/mL) was pipetted into each agarose mold. The suspension was placed into the 37°C incubator overnight. The following morning, the spheroids were collected by inverting the molds in the 24-well plate and spinning for 5 minutes at 500 rpm. The spheroids were collected and stored in a non-adherent flask on a shaker (to maintain individual spheres) in the 37°C incubator until used in the study.

2.2.4 Spheroid seeding onto coverslips

For seeding the spheroids onto the nanofiber-coverslips, the media was collected from the shaker flask and spun down at 500 rpm to concentrate the spheroids, which were resuspended in 1mL of media. Individual spheroids were then placed in the center of the coverslip (1-2 per coverslip) in about 5 µL of media with a 10 µL pipette. Additional media (100uL) was then added to keep the spheroid submerged, but also in the center of the coverslip. After 60 minutes in the incubator, 400 µL of additional media is gently added to each well and the plate is returned to the incubator.

2.2.5 Spheroid imaging

The 24-well plate containing the coverslips and migrating spheroids were imaged after 1, 2, and 4 days (and in some groups 6 and/or 8 days) of migration on an EVO FL Auto Cell Imaging System (Thermo-Fisher Scientific). The on-scope incubator maintained a 37°C, 5%CO2 and 100%RH environment during imaging. The spheroids and migrating cells were imaged at 10x or 20x in the GFP channel, using the scope software to stitch the tiled images of the cell field into one large image per spheroid.

2.2.6 Data analysis

MatLab was used to analyze the images. Briefly, the program first normalized the images and a blob detection algorithm was employed to identify all cell clusters in the

images. Starting from the spheroid cluster, the cell clusters were traversed outwardly, with traverses in both the left and right directions. The traverses were halted when the next cluster was beyond 70 μm beyond the previous cluster to prevent artifacts from clouding the analysis. After reaching the end of the traverse, the weighted average distance of the five most distant clusters was determined. The weights were determined by the size (number of pixels) of each cluster, to account for multiple cells, in a cluster, though at the cell field periphery, the cell clusters were almost exclusively single cells. The parameters optimized for the analysis include threshold distance, normalizing factor, and min/max cluster size to prevent artifacts.

2.3 Results

2.3.1 Live cell tracking: coating study

The Schwann cells were seeded upon glass coverslips with identical 1.2 μm fiber properties, but varying coatings. The live cell tracking results show that Schwann Cell migration is an inherently heterogeneous process with subpopulations of slower cells and faster cells, which can reach speeds of 2 μm/min. Coating had little effect, with similar median migration rates and range of rates on PLL-coated fibers, Matrigel coated fibers, and laminin-coated fibers with 4 different concentrations from 200 ng/mL up to 100 μg/mL (Fig 2.1). This is not necessarily surprising, as the cell media is supplemented with 5% fetal bovine serum (FBS), which contains proteins such as albumin that will add to the coating on the surfaces regardless of the previous coatings, making the fiber coating differences subtle. The 200 ng/mL coating of laminin had almost the exact same

median migration rate as the 100 μg/mL laminin coating. Matrigel coatings were used in subsequent studies for convenience and consistency since the results were similar to the other groups.

2.3.2 Live cell tracking: fiber diameter screen

The boxplots of the Schwann cell migration rates on a broad range of fibers can be seen in Fig 2.2a. There is a slight trend towards slower migration rates on fibers with diameters of 350nm or 750 nm, with relatively faster migration upon larger 3.2 μm and 6 μm. The median migration rates are fairly uniform being about 0.5 μm/minute, which correlates to 30 μm/hour or 720 μm/day. The overlaid traces of the cells migrating on 610 nm random fibers and glass slides show that there is no directional bias to the migration (Fig 2.2b). In comparison, the 750 nm fibers had extremely oriented cell migration, while the 180nm fibers had strong overall migration, but more off-axis migration as well. This is likely a result of two factors: the 180 nm fiber group had a higher percentage of off-axis fibers as a function of the higher whip speed during electrospinning; the smaller fibers providing less of a barrier height to the lamellipodia of migrating cells, allowing more lateral movement across the fiber alignment axis. The cell migration on the 2D glass was almost normal in distribution, unlike the nanofiber-covered groups (Fig 2.2c). A larger fraction of cells on the nanofiber groups have essentially zero migration over the course of the imaging. It is unknown whether this is due to the inability of those cells to migrate or whether the fibers themselves induced this stationary behavior. The cells exhibited a broad range of speed on the nanofibers, and while the median cell migration

was no higher than the 2D glass, the aligned fiber groups may enable the cells predisposed towards motility to migrate faster—the aligned fibers groups had a much higher percentage of the cell population that migrated at rates over 1 μm per minute and had more outliers at rates above 2 μm per minute.

2.3.3 Spheroid net migration studies: glass versus randomly aligned nanofibers

To determine if fiber alignment is necessary to generate the increased cell migration rate, we seeded Schwann cell spheroids onto glass coverslips, coverslips with 650nm randomly aligned fibers, and coverslips with 1200 nm randomly aligned fibers. For comparison, the images of a spheroid seeded upon aligned 1.5 μm fibers can be seen in Fig 2.3. The cells migrated distances remarkably similar migration rates, which were significantly lower than the rates seen along aligned fibers (Fig. 2.4). Determining the rate from the linear regression of the points from day 1 to day 4, the cells on glass migrated 382.4 μm/day, the cells on 650 nm random fibers migrated 325.6 μm/day, and the cells on the 2300 nm random fibers migrated 336.3 μm/day. The cells showed no directional preference, in the random fiber groups or on the glass, migrating outward equally in all directions producing a circular cell field. This indicates that the increased surface area alone (which is still provided in the random nanofiber groups) is not responsible for the increased migration rate, but rather the topographical guidance.

2.3.4 Spheroid net migration studies: fiber-coated coverslips to migration on suspended fibers with and without gel

One possible artifact of this analysis is that the fibers are generally adhered onto an extremely stiff substrate, namely the glass coverslip. Such a stiff substrate is absent in the actual regenerating nerve, however. If the migrating cells interacted heavily with the glass surface, or if the glass surface affected the local properties of the nanofibers, then this style of evidence may provide little predictive value over how the cells will respond to the nanofibers *in vivo*. The fibers in vivo will consist of a dense layer of aligned fibers that may or not remain attached to a random-fiber backing. To address this concern, we compared the migration of Schwann cells from spheroids placed upon a layer of 650 nm fibers attached to the glass coverslip to the same fibers suspended but taut in the media via a plastic washer. The migration results can be seen in Fig 2.5, showing that the differences in migration between fibers on glass and suspended fibers was within the typical variance from experiment to experiment in the same group. Determining the rate from the linear regression of the points from day 1 to day 4, the cells on 650 nm fibers on glass migrated 577.8 μm/day, the cells on 650 nm suspended fibers migrated 593.4 μm/day, and the cells on the 650 nm fibers suspended in gel migrated 359.2 μm/day. This adds validity to the idea that our results of our cell migration on fiber-coated coverslips will translate to the regenerating nerve environment. Note that this analysis corresponded with the case wherein the cells follow along multiple fibers. If the fibers were sufficiently dispersed so as to restrict the cells to travel along individual fibers, then it is possible that there would be a large difference between the coverslip-fibers and the

suspended fibers due to the vastly different adhesion sites available in the two cases. Additionally, this experiment included a group wherein the cells were seeded upon suspended 650 nm fibers that were further embedded within a hydrogel (5 mg/mL thiolated hyaluronic acid with 10 mg/mL PEG-DA and 20 μg/mL laminin). The cells preferentially adhered to the nanofibers versus the hydrogel, despite adhesion sites available in the gel as well in the form of laminin. The cells readily migrated through the gel along the nanofibers, albeit at a slower rate, as expected by the increased resistance of the gel.

2.3.5 Spheroid net migration studies: varying nanofiber diameter

The spheroids were next seeded upon glass coverslips with several different nanofiber diameters that cover the range of diameters we may try *in vivo*, namely 200 nm, 750 nm, 1200 nm, and 3000 nm. This data indicates that Schwann cells migrate readily upon several different fiber diameters, with similar overall migration rates and extremely high directedness in all groups (Fig 2.6). The smallest fiber group in the experiment (200nm) migrated the fastest at 1080.4 μm/day, with the next fastest being the largest fiber group in the experiment 3000 nm at 757.1 μm/day. This demonstrates that there is no inherent correlation between fiber diameter and migration rate at this length scale. The 1200 nm fiber group migrated the next fastest at 623.2 μm/day, while the 750 nm fiber group migrated the slowest at 552 μm/day.

2.3.6 Live cell tracking: cytosolic imaging

To better understand the interactions between the migrating Schwann cells and the different diameters of nanofibers, a live cell tracking experiment was performed, but with the eGFP Schwann cells instead of the Hoechst stain, allowing for the imaging of the whole cell's responses to the nanofibers. While this imaging method made it significantly more difficult to identify the individual cells for determining the migration rates, it showed in much greater detail how the cells interact with the nanofibers with its lamellipodia. The lamellipodia and filopodia response was very different depending upon the fiber conditions. The cells seeded upon glass had several fringes of lamellipodia on all sides and frequently changed directions (Fig. 2.7). The cells seeded upon the randomly aligned fibers also frequently switched directions, but the lamellipodia were more spindly and associated with the underlying fibers.

The smallest aligned fiber groups had broad lamellipodia that aligned with the nanofibers, with each lamellipodia spreading over multiple fibers (Fig. 2.7). Thus, the cells were able to move laterally with more ease, diminishing directedness. However, the broader lamellipodia may speed cell motility by giving the cell a clear signal about which direction to move with what is likely a coherent, broad region of actin formation.

The 650 nm fiber group had very interesting lamellipodia/filopodia interactions. The leading edges of the cell would have lamellipodia with multiple filopodia stretching out several microns ahead along the aligned fibers. (Fig. 2.7) The cells may be receiving conflicting signals about where to move the cell, potentially explaining the reduced speed

on this size of fibers. The 1200 nm fiber group also exhibited extremely long cell processes (Fig. 2.8).

The largest two fiber groups (2 μm and 8 μm) largely restricted the lamellipodia/filopodia to one or two fiber tracts, providing boundary guidance to the cells, which may explain their increased rate over the 650nm fibers. Additionally, the lamellipodia may be able to attach more easily to individual fibers with the larger fiber surface area of the 2 μm and above fibers. The cells can be seen with lamellipodia clearly able to adhere to individual fibers in the suspended fiber group (Fig 2.8).

2.4 Discussion

The aligned nanofiber groups tested all showed excellent potential to direct cell migration. While the differences in the migration of individual cells were small between groups in the live cell tracking experiments, the directedness was far higher on the aligned fibers. This resulted in dramatically different migration patterns when the cells were allowed to migrate continuously for several days in the spheroid culture experiments. Committing the cells to migrate largely upon one axis resulted in the net migration of cells far further than was seen in the randomly aligned fiber or 2D glass groups. In some of the groups, the cells were able to migrate a net distance of up to 1 mm a day, much faster than seen in much of the literature. The similar migration rates may not be surprising, as the cells were seeded upon a dense layer of nanofibers, not individual fibers. The cells tended to migrate along the grooves formed by two neighboring fibers. These grooves are more subtly different between fiber diameters than a single suspended cell would be, leading to more subtlety in the differences between

fiber groups. As seen in the live cell tracking experiments, the cells migrated slightly slower on the 650 nm fiber group than the smaller (200 nm) or larger (1 μm and above fibers) fiber groups.

This unexpected phenomenon may be explained by the live cell tracking of the eGFP cells, as the fibers were too large to allow the lamellipodia to spread over several fibers, while still allowing multiple lamellipodia/filopodia to extend for several microns, trapping the cell between the conflicting signals from its lamellipodia.

It has previously been established that aligned nanofibers can increase the maturation of Schwann cells [25]. Since immature Schwann cells differentiate into myelinating or non-myelinating adult Schwann cells depending upon interaction with larger versus smaller fibers, it is plausible that larger aligned fibers will induce maturation in Schwann cells. It is unclear if this would be a benefit or detriment in a nerve guide, as mature Schwann cells migrate slower, proliferate slower, and potentially produce less growth factors for attracting axons. On the other hand, mature Schwann cells are necessary for the support and myelination of the regenerated axons. Very large fibers might induce maturation too early in the regeneration process, while small, 180 nm fibers could theoretically inhibit maturation by mimicking the small axons which drive Schwann cells into a mature, non-myelinating stage.

2.5 Conclusions

These experiments clarified the properties that we should select for the nanofibers in our *in vivo* applications. All of the aligned fiber groups provided excellent directional

guidance as compared to the glass or random fiber controls, validating our expectations that they could provide topographical guidance to the regenerating tissue. Further, the studies showed that the fibers could direct the cells to migrate for several days at the net rate of up to 1 mm/day, an appropriate rate for rapidly populating the nerve guides.

Based upon this set of experiments, we chose 1200 nm fibers to be used as the initial alignment cue in our nerve guides. This diameter was chosen for several reasons. Firstly, all of the aligned fiber groups did a good job of directing cells in one orientation fairly rapidly. The 1200 nm fiber group exhibited similar migration rates to the other fiber rates, enabling Schwann cell migration of up to nearly 1mm/day, which is sufficiently fast to populate the nerve guide from both sides before the axons begin extending through the nerve guide. While the 1200 nm fibers induce slightly slower migration than 180 nm fibers, they provide a stronger directional cue and will likely only have a mild effect upon cell maturation. It may be worth exploring the use of 180 nm fibers in future studies, however.

2.6 Figures

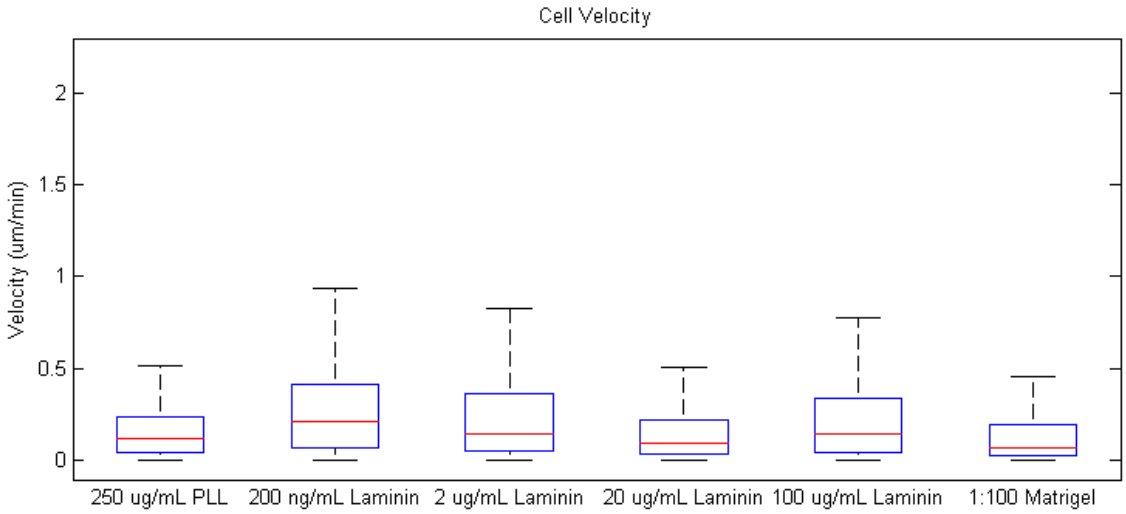

Figure 2-1: Live cell imaging of Schwann cells: The effect of fiber coatings

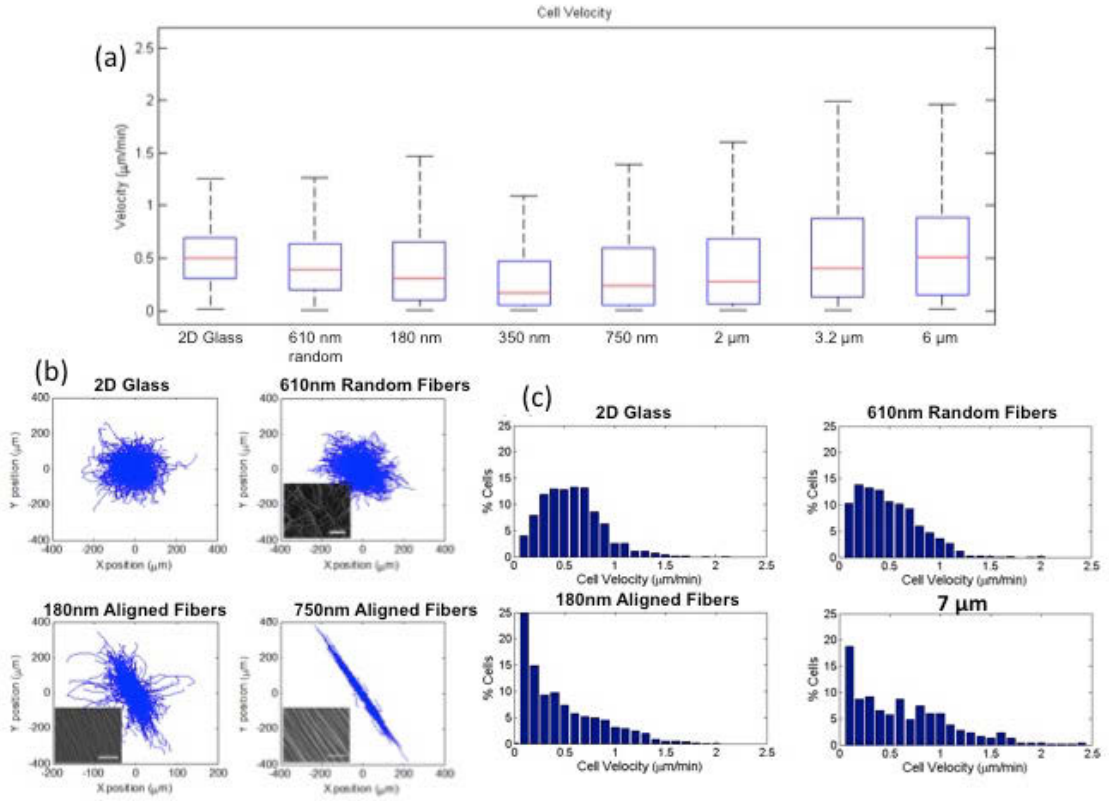

Figure 2-2: Live Cell imaging. The effects of fiber diameter and alignment

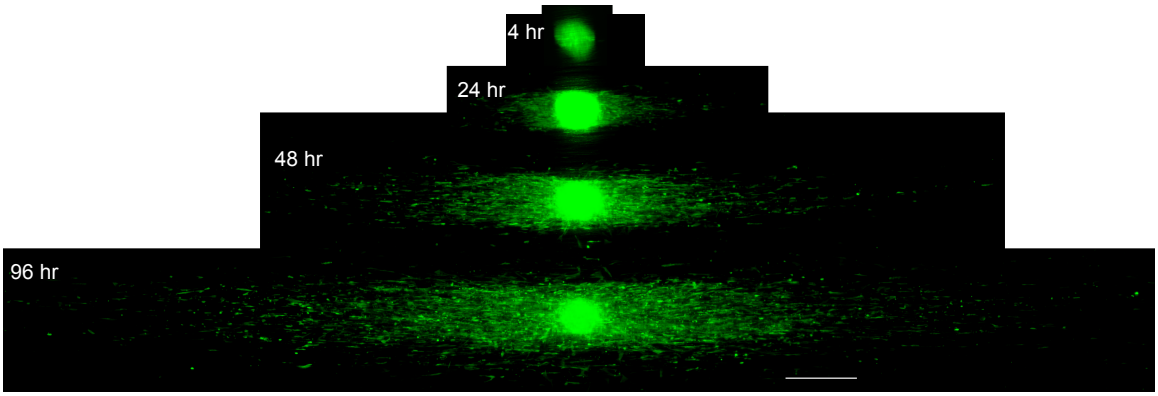

Figure 2-3: Migration of Schwann cells from the same spheroid seeded upon 1.5 μm aligned nanofibers.

Time listed is hours post-seeding. Scale bar is 500 μm

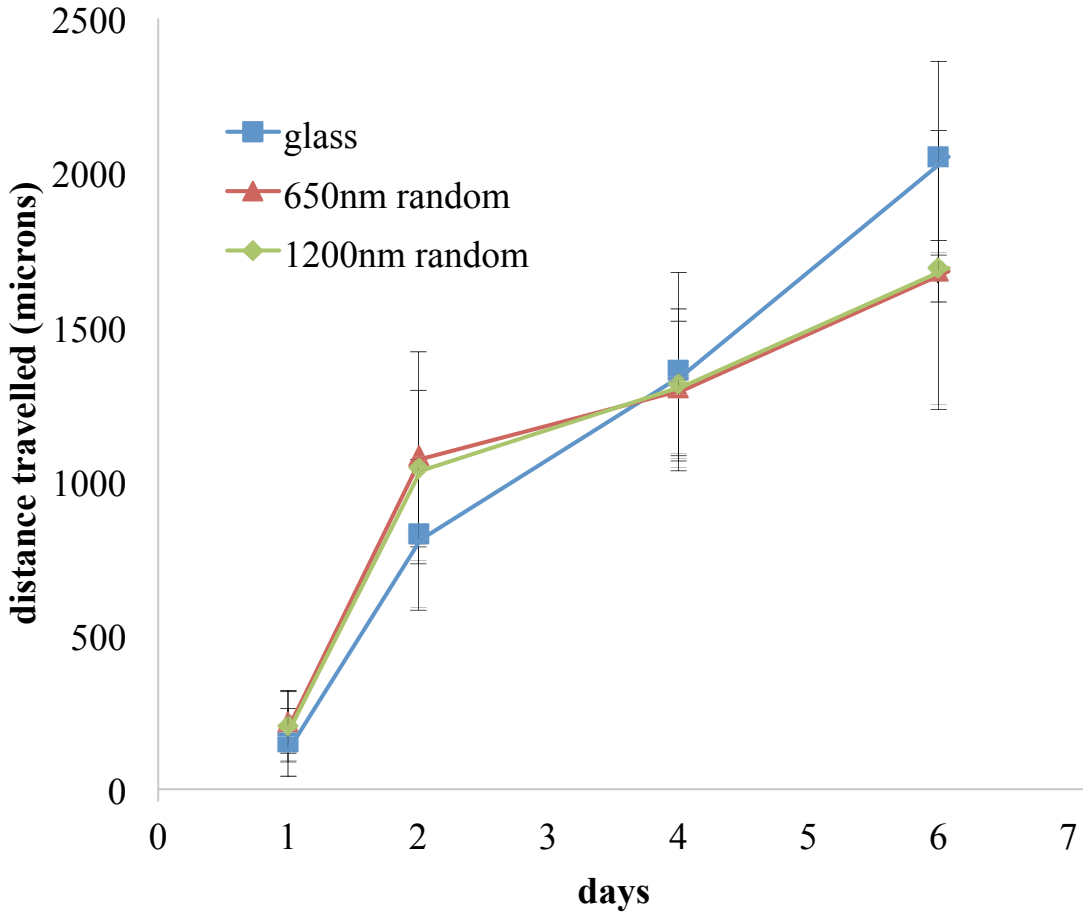

Figure 2-4: Quantification of the net migration of Schwann cells on non-oriented substrates: glass, 650nm random fibers, and 1200nm random fibers.

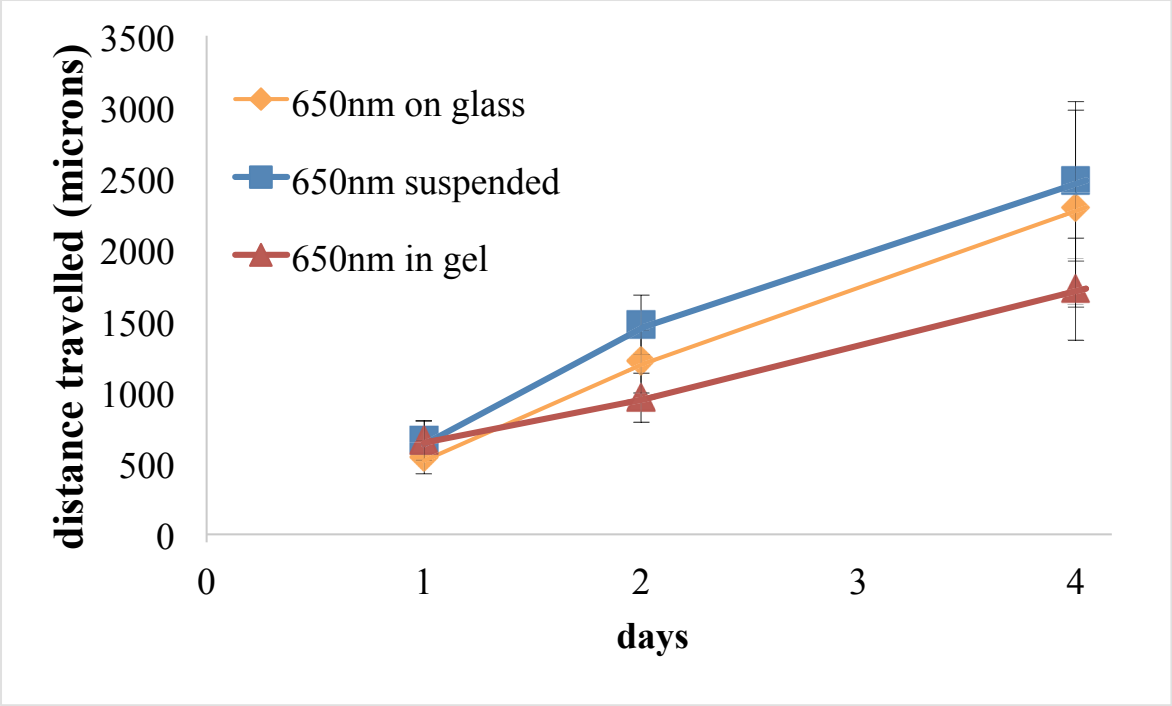

Figure 2-5: Quantification of the net migration of Schwann cells: varying media

Schwann cells were cultured on 650nm fibers that are either: adhered to a glass coverslip, suspended in the cell media, or suspended in a hydrogel.

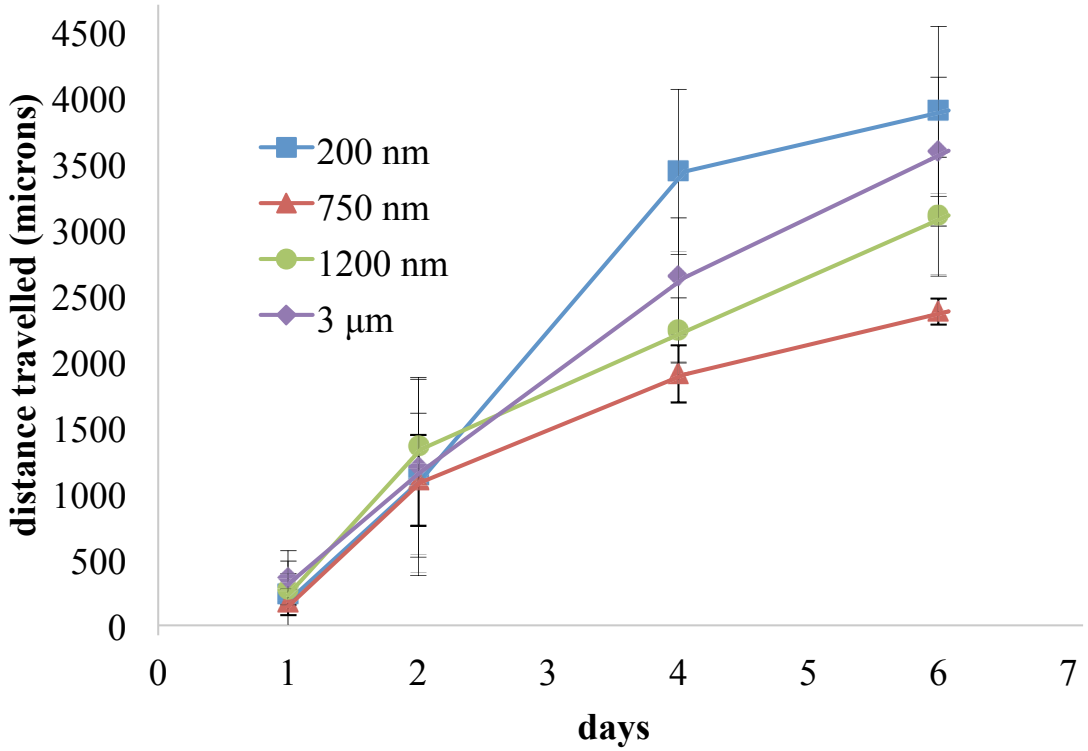

Figure 2-6: Quantification of the net migration of Schwann cells: fiber diameter

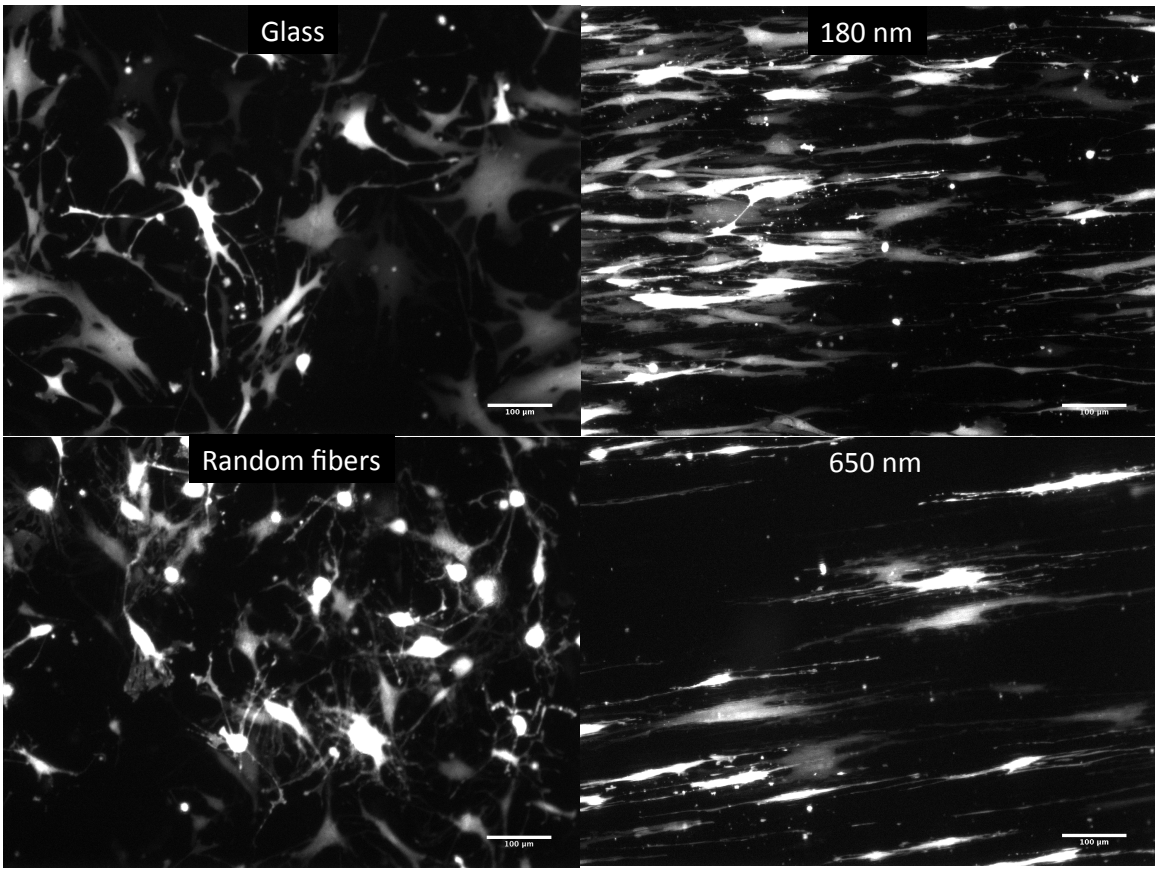

Figure 2-7: Live cell tracking of GFP Schwann cells on fibers.

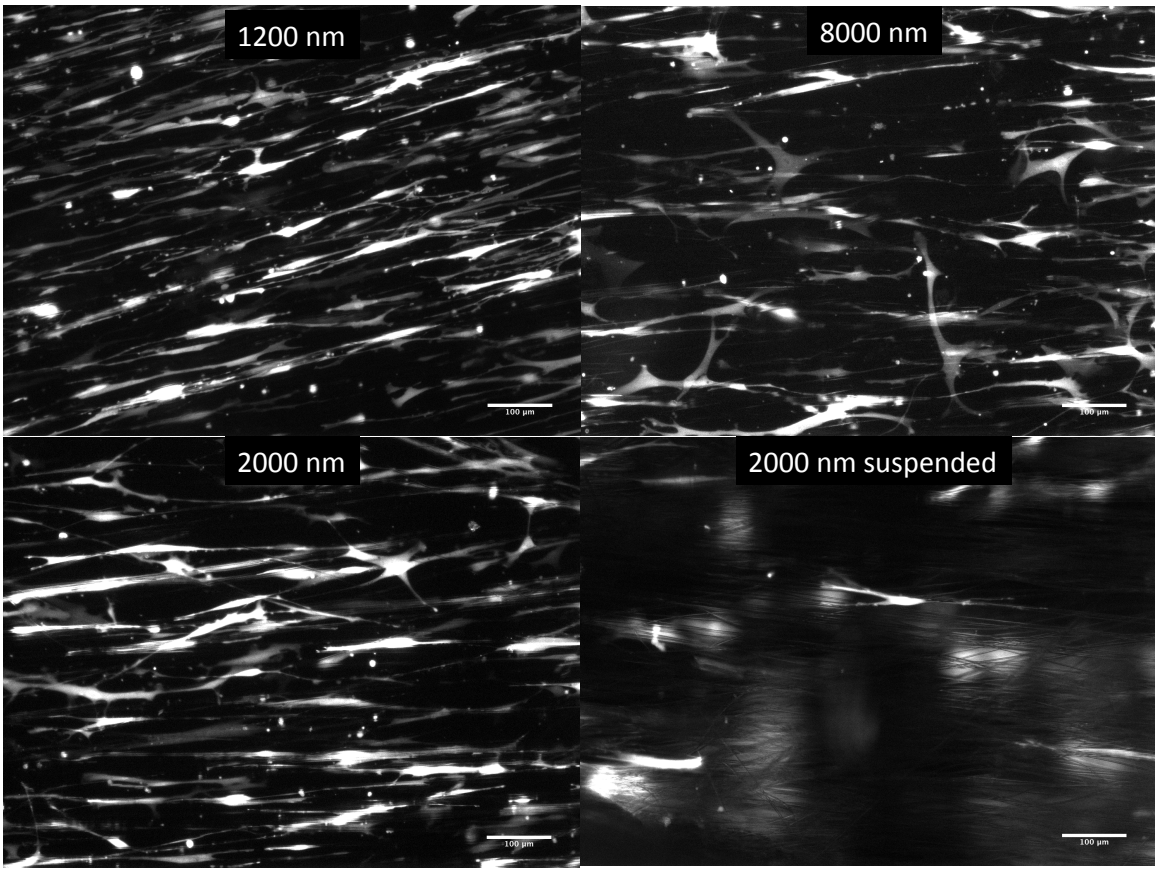

Figure 2-8: Live cell tracking of GFP Schwann cells on fibers.

2.7 References

1. Mirsky, R., et al., *Schwann cells as regulators of nerve development*, in *J Physiol Paris*. 2002. p. 17-24.
2. Jessen, K.R. and R. Mirsky, *Schwann cells and their precursors emerge as major regulators of nerve development.*, in *Trends Neurosci.* 1999. p. 402-410.
3. Fawcett, J.W. and R.J. Keynes, *Peripheral nerve regeneration.*, in *Annu. Rev. Neurosci.* 1990. p. 43-60.
4. Namgung, U., *The Role of Schwann Cell-Axon Interaction in Peripheral Nerve Regeneration*, in *Cells Tissues Organs*. 2015.
5. Scherer, S.S. and J.L. Salzer, *Axon-Schwann cell interactions during peripheral nerve degeneration and regeneration*, in *Glial cell development*. 1996, Bios Scientific Publishers Oxford. p. 299-330.
6. Jessen, K.R. and R. Mirsky, *Schwann cells: early lineage, regulation of proliferation and control of myelin formation.*, in *Current opinion in neurobiology*. 1992. p. 575-581.
7. Gordon, T., N. Tyreman, and M.A. Raji, *The basis for diminished functional recovery after delayed peripheral nerve repair.*, in *Journal of Neuroscience*. 2011. p. 5325-5334.
8. Hoke, A., et al., *A decline in glial cell-line-derived neurotrophic factor expression is associated with impaired regeneration after long-term Schwann cell denervation.*, in *Experimental Neurology*. 2002. p. 77-85.
9. Jonsson, S., et al., *Effect of Delayed Peripheral Nerve Repair on Nerve Regeneration, Schwann Cell Function and Target Muscle Recovery*, in *PLoS ONE*. 2013. p. e56484.
10. Mirsky, R. and K. Jessen, *The neurobiology of Schwann cells*, in *Brain Pathology*. 1999. p. 293-311.
11. Jaakkola, S., et al., *Basement membranes during development of human nerve: Schwann cells and perineurial cells display marked changes in their expression profiles for laminin subunits and beta 1 and beta 4 integrins.*, in *J. Neurocytol.* 1993. p. 215-230.
12. Bunge, R.P., *Expanding roles for the Schwann cell: ensheathment, myelination, trophism and regeneration.*, in *Current opinion in neurobiology*. 1993. p. 805-809.
13. Hogervorst, F., et al., *Biochemical characterization and tissue distribution of the A and B variants of the integrin alpha 6 subunit.*, in *The Journal of Cell Biology*. 1993. p. 179-191.
14. Milner, R., et al., *Division of labor of Schwann cell integrins during migration on peripheral nerve extracellular matrix ligands.*, in *Dev. Biol.* 1997. p. 215-228.
15. Webber, C., *The nerve regenerative microenvironment: Early behavior and partnership of axons and Schwann cells*, in *Experimental Neurology*. 2010.
16. Hayashi, A., et al., *A double-transgenic mouse used to track migrating Schwann cells and regenerating axons following engraftment of injured nerves.* Experimental neurology, 2007. **207**(1): p. 128-138.

17. Seggio, A.M., et al., *Self-aligned Schwann cell monolayers demonstrate an inherent ability to direct neurite outgrowth*, in *Journal of Neural Engineering*. 2010. p. 046001.
18. Frostick, S., Q. Yin, and G. Kemp, *Schwann cells, neurotrophic factors, and peripheral nerve regeneration*, in *Microsurgery*. 1998. p. 397-405.
19. Regan, T., et al., *Nanofibers promote Schwann cell migration when Schwann cell proliferation is impaired.* MINERVA BIOTECNOLOGICA, 2013. 25(3): p. 143-150.
20. Daud, M.F.B., et al., *An aligned 3D neuronal-glial co-culture model for peripheral nerve studies.*, in *Biomaterials*. 2012. p. 5901-5913.
21. Tonazzini, I., et al., *Schwann Cell Contact Guidance versus Boundary Interaction in Functional Wound Healing along Nano and Microstructured Membranes.*, in *Advanced Healthcare Materials*. 2015.
22. Jha, B., et al., *Two Pole Air Gap Electrospinning: Fabrication of Highly Aligned, Three Dimensional Scaffolds for Nerve Reconstruction*, in *Acta Biomaterialia*. 2010.
23. Wang, H.B., et al., *Varying the diameter of aligned electrospun fibers alters neurite outgrowth and Schwann cell migration.*, in *Acta Biomaterialia*. 2010. p. 2970-2978.
24. Jiang, X., et al., *Nanofibrous nerve conduit enhanced peripheral nerve regeneration*, in *J Tissue Eng Regen Med*. 2012, Wiley Online Library.
25. Chew, S., et al., *The effect of the alignment of electrospun fibrous scaffolds on Schwann cell maturation*, in *Biomaterials*. 2008. p. 653-661.

Chapter 3 Nanofiber-based Nerve-Guidance Conduits for Enhanced Peripheral Nerve Regeneration

3.1 Background

Peripheral nerve injuries are a serious public health concern, occurring in 2.8% of traumatic injuries and often causing lifelong disabilities [1]. Approximately 360,000 patients suffer upper extremity paralytic syndromes annually in the United States, causing over 8.5 million restricted activity days [2]. While direct end-to-end anastomosis is preferred where possible, peripheral nerve injuries often exhibit nerve gaps that need to be surgically bridged in order to restore function. Autologous nerve grafts are the current gold standard for this type of repair, but have several drawbacks including the need for additional surgeries, donor site morbidity, neuroma formation, size mismatch, and limited efficacy [3]. There are several FDA-approved conduits for bridging these gaps, but these have poor efficacy over longer gaps, in part due to the absence of any guidance cues [4]. One of the most commonly tested methods of providing a guidance cue is via inclusion of physical alignment features, such as filaments, aligned electrospun fibers, grooves, interconnected pores, and channels, to provide topographical guidance substrate upon which the regenerating nerve can grow across the longer gaps [5-10]. Besides physical guidance cues, various approaches of delivering neurotrophic factors (NFs) to the regenerating nerve have been explored using hydrogels, microspheres, and viral-based gene transfection methods to promote nerve survival and enhance axonal outgrowth across the injury gap [11-16]. Localization of delivery of immobilized or diffusible NF

gradients within nerve conduits have shown promising improvements in regeneration of nerves compared to isotropic delivery of NFs. Although showing moderate success in promoting nerve growth into the nerve gap, delivery of uniform concentrations or excessively high concentrations of NFs has been shown to cause axon trapping within the conduit, resulting in poor functional outcome by limiting the number of nerves exiting the conduit into the distal stump [11-14].

One of the major limitations of the current conduit designs is the lack of *unidirectional* guidance cue capable of promoting outgrowth of axons towards the distal stump. To address this challenge, several strategies of delivering NF gradients have been proposed to enhance unidirectional migration of axons *in vitro* [17-20]. However, the optimal gradient pattern for nerve regeneration remains elusive. This provides impetus for further investigation of the effect of NF gradient steepness and concentration range, as well as the type of NFs, on the regenerative outcome [21, 22]. The lack of technical platforms for preparing and testing tuneable gradient patterns has limited the advance in optimizing the NF gradient characteristics at centimeter length scales prior to translation of gradient delivery to *in vivo* platforms.

Guidance of endogenous Schwann cells is of particular importance in enhancing nerve regeneration due to the numerous roles of Schwann cells in the nerve repair process, during which Schwann cells precede the axons into the lesion site secreting extracellular matrix tracks upon which regenerating axons grow [23-25]. Additionally, Schwann cells, especially in the distal stump of the nerve injury, produce a cocktail of NFs to promote

neuron survival and growth of regenerating neurons into the distal stump [23-24]. Little attention has been given to the effect of NF gradients in a nerve guide on Schwann cell migration and ingrowth.

Here we have developed a gradient generation platform to produce hydrogels loaded with tailorable gradients of glial-derived neurotrophic factor (GDNF) that are suitable for both i*n vitro* and i*n vivo* testing. Using this versatile platform, we investigated the effect of GDNF concentration and gradient steepness on Schwann cell migration using *in vitro* live cell tracking method. More importantly, we examined the synergistic effect of NF gradient pattern and aligned nanofiber topography on migration guidance of Schwann cells. We then incorporated the gradient hydrogels into nanofiber-based nerve conduits and evaluated the effect of gradient pattern on nerve regeneration outcome in a rat sciatic nerve repair model.

3.2 Methods

3.2.1 Gelatin spiral-based NGC design

We initially designed a NGC to test the hypothesis that increasing the available surface area of aligned fibers should increase the alignment "signal" to the regenerating nerve, and thus boost the regeneration rate and the accompanying functional recovery. The previous design by Shawn Lim utilized only one layer of aligned fibers along the periphery of the open NGC lumen, providing a surface area of only 70 mm^2 within the 15mm nerve guide. To increase the surface area of aligned fibers, we electrospun the

aligned fibers onto 20 mm by 15mm sheets of crosslinked gelatin (exposed to the vapor-phase of 1.5% glutaraldehyde in water), which were then rolled up into a "spiral" bundle around a 500 μm steel mandrel, increasing the area of aligned fibers to 300 mm^2.

The random-mesh PCL outer wall was then electrospun directly upon the outside of the spiral bundle (8%wt PCL (80k) in 90/10 DCM-DMF solution at 0.75 mL/hr through a blunt 27 gauge needle with a positive voltage of 7.5 kV on the needle and a negative voltage of 2 kV applied to the mandrel with a separation distance of 6cm. The wall was spun for 7 min. The spiral tubes are then soaked on the mandrel for 90 minutes in 1.5% Glycine solution to neutralize any residual glutaraldehyde present and to swell the gelatin to allow for the planned 14 mm gap in the 15 mm tube. The bundle was then washed in RO water and cut to 14mm and a copper spacer placed at each end. The bundles were then electrospun again with the same spin conditions for an additional 10 minutes to produce a thicker outer wall that also extended 0.5mm past the gelatin layer on both sides to allow placement of the nerve stumps. The completed tubes were then removed from the mandrel, sterilized via serial ethanol soaking (3x 30 min soaks in 100% ethanol), and allowed to dry. The tubes were then implanted into the left sciatic nerve of male Sprague-Dawley rats, per standard protocol. There were several groups tested with this design, with 8 rats per group and a study length of 8 weeks. The groups varied the density of aligned fibers (electrospun for 0, 6, 12, and 18 passes), the GDNF loading level (0, 20, 200, and 2000 ng GDNF per tube loaded via soaking the gelatin backing sheets in GDNF solution), and the overall gelatin configuration as compared with a single fiber layer design, as can be seen in table 3.1. Following the end of the

study, the rats were sacrificed and the nerve guides were harvested, sectioned, and stained for histological analysis.

3.2.2 Fibrin spiral design

To replace the gelatin backing with an alternative, cell permeable fiber backing, the aligned nanofiber layer was produced by electrospinning directly upon plastic sheets instead of the gelatin films. The aligned fibers were then sterilized via exposure to the UV light in the biosafety cabinet for 30 minutes before the fibrin-backing layer was formed aseptically. The fibrin glue (Baxter Tisseel ndc-0944) used at 38.825 mg/mL, 25% of its stock concentration. The15 mm by 20 mm aligned fiber layer was wetted with 50 μL of Tisseel fibrinogen solution, with tweezers used to ensure even coverage. 50 μL of Tisseel thrombin solution (75 units/mL in 300mM calcium chloride solution) was then added to the layer to induce clotting. After mixing, the construct was tilted to remove excess liquid and the fiber-fibrin layer was allowed to set in the incubator. After setting. The fibrin-fiber layer was rolled up into a spiral with the use of a titanium mandrel, with the fibers aligned with the long axis of the mandrel. The fibrin spiral bundle was then wrapped in a layer of PVA-Collagen hydrogel foam, which had been preformed to controllably release the GDNF (600 ng per conduit). The resulting bundle was then cut to 14 mm in length and place inside the pre-formed PCL outer tube. The conduits were implanted and analyzed identically to the gelatin-spiral groups previously described. The fibrin spiral groups were designed to test for the effects of varying the fiber diameter (400 nm, 760 nm, and 1200 nm) and the fiber degradation rate with slowly degrading (100%

PCL), medium degrading (80% Gelatin and 20% PCL), and quickly degrading fibers (90% Gelatin and 10% PCL).

3.2.3 Gradient generation and characterization for S-Shaped NGC design

Gradients of GDNF (R&D Systems) were created using a surface tension and evaporation-based, single channel microfluidics method developed by the Khademhosseini lab [26]. Gradients were immobilized in methacrylated gelatin synthesized as described previously [27, 28]. Gradient characterization was conducted by generating a gradient of fluorescently-tagged lysozyme or GDNF and imaging using a Typhoon Gel Reader.

3.2.4 Concentration-dependent gradient-based release

Hydrogels containing gradients (0 to 5 μg/mL) of FITC-labelled lysozyme were generated and cut into six equal segments. The segments were placed separate wells of 96 well plate and PBS was added to the wells, collecting and replacing the solution volume on days 1, 3, 7, and 14. Concentration was measured using a plate reader and compared to standards.

3.2.5 Live cell tracking

Hydrogels (8 mm in length) containing GDNF gradients (0 to 1 μg/mL) were prepared and placed on 15 mm coverslips. Aligned electrospun fibers (see below for fiber fabrication) were placed over the hydrogels and immobilized using factor 2 tissue glue. A custom PDMS migration channel (4 mm by 10 mm by 0.1 mm) was placed over the hydrogel/fiber construct. Primary human Schwann cells (ScienCell) were seeded for two days prior to experiment and exposed to 1 μg/mL Hoechst 33342 (Pierce) for 30 minutes prior to use, washed with PBS, trypsinized, injected into the channel at 1000 cells per sample and allowed to adhere for 6 hours prior to cell tracking. Cell migration was observed using live cell imaging microscope with a programmable stage (Nikon) and migration was analysed using Metamorph. Motility for each cell is calculated as follows: $Motility = \frac{Total\ distance\ travelled}{Total\ migration\ time}$. Directedness for each cell is calculated as follows: $Directedness = \frac{\sum \frac{Cell\ vector \cdot Field\ vector}{norm(Cell\ vector) \times norm(Field\ vector)}}{Number\ of\ frames}$, where "Cell vector" is the positional vector a cell has moved in one frame and "Field vector" is the vector defined as the direction of the gradient.

3.2.6 Electrospinning and preparation of S-Shaped nerve guide

The electrospinning was performed as described in chapter 1 and previous work [29]. Briefly, a solution of 8%w/w PCL (molecular weight of 80k, Sigma) in a solvent of 90%w/w DCM and 10%w/w DMF is electrospun at 5mL/hr through a 27-gauge needle 11cm from the face of a 40cm-diameter wheel rotating at 70rpm with a 13 kV positive voltage. The apparatus was moved across the wheel face via a linear stage (Newmark

Systems), over a distance of 75mm at 0.1mm/sec for 2 hours. The nanofiber mat was partially melted to increase strength by heating with a hair dryer for 5 seconds. The aligned PCL nanofibers were then electrospun directly onto the partially-melted backing film, by spinning 12%w/w PCL in Chloroform at a flowrate of 0.6mL/hr and +8kV voltage 6cm from the wheel surface, which rotated at 750rpm. The aligned fibers were spun for 12 passes at 0.1mm/sec for travel distance of 70 mm. The conduit outer wall was electrospun with the 8%w/w PCL in DCM/DMF solution at a flowrate of 0.75mL/hr through a 27-gauge needle 6cm from a rapidly rotating 1.5mm steel mandrel. A 7.5kV positive voltage is applied to the needle tip, while a 2.5kV negative voltage is applied to the mandrel, spinning over a distance of 23cm for 70 passes at 5mm/sec. The tubes were then lyophilized for 48 hours to remove residual solvent, then heat-treated to increase strength by soaking in hot water, 20 minutes subsequently at each of 50°C, 54°C, and 56°C. The tubes were then cut to 10mm segments and sterilized. The aligned nanofiber sheets and nanofiber outer walls were sterilized via ethylene oxide sterilization.

3.2.7 Gradient hydrogels for nerve guidance conduits

Hydrogels containing GDNF gradients were prepared using a 1 cm gradient channel (4.5 μL channel volume) and cut to 7 mm in length. All groups with GDNF contained 600 ng of GDNF in the final 7 mm hydrogel strip. Uniform GDNF was loaded at 190 μg/mL. To generate the shallow gradient, 4.5 μL of 95.2 μg/mL GDNF was preloaded into channel and 1.5 μL of 200 μg/mL GDNF was added at the inlet. Steep

gradient hydrogels were generated by adding 1.5 μL of 400 μg/mL GDNF solution onto the inlet of a pre-filled channel containing no GDNF. The gradient gels were placed between two layers of aligned nanofibers, which were then wrapped around two 500μm steel mandrels to form the S-shape seen in Figure 3.3. The wrapped sheets were then inserted into the lumen of the 10mm-long electrospun outer tube, and the mandrels are carefully removed. The sheets were oriented so that the fibers were aligned longitudinally along the nerve guide.

3.2.8 Sciatic nerve transection and repair in rats

All animal surgeries and evaluation of the outcome of the nerve repair were carried out according to protocols approved by the Johns Hopkins Institutional Animal Care and Use Committee. The surgeries were performed on adult male Sprague-Dawley rats (200 – 300 g). Following isoflurane anesthetization, the sciatic nerve in the left leg was exposed through a mid-thigh incision. The nerve guidance conduits were pre-wetted by soaking in sterile PBS. 5mm of the nerve was resected, and each end of the nerve was inserted 1.5 mm into the nerve guidance conduit to leave a gap of 7 mm between the nerve ends. The nerve ends were sutured in place via 10 – 0 nylon sutures (Ethicon). The surgical site was closed with wound clips, and 0.1 mg/kg of buprenorphine was injected for pain management. The animals were allowed free access to food and water and were regularly monitored.

3.2.9 Electrophysiology assessments

The compound motor action potentials were recorded according to standard protocols using LabChart (AD Instruments) [30]. The stimulating needle electrodes were inserted into the sciatic notch, proximal to the nerve guide. The recording electrodes were placed into the ankle, at a distance of 7.2 cm +/- 0.3 mm from the stimulating electrodes.

3.2.10 Harvesting of regenerated nerves

Following electrophysiology testing, the rats were euthanized. The nerve guide and surrounding nerve was removed and fixed in 4% Paraformaldehyde. After 24 h at 4°C, the middle segment of the nerve guide (2.5-5.5 mm from proximal nerve stump) was resected and fixed for a further 24 h at 4°C in 4% paraformaldehyde and 3% glutaraldehyde. The tissue was mounted in embedding resin, sectioned, and stained with toluidine blue [30].

3.2.11 Histomorphometric analysis

Imaging of the fixed nerve sections was conducted using an inverted microscope (Nikon) at 10× and 63× magnification. Total nerve tissue area was measured at 10×. Nerve count was measured at 63× by averaging the axon count within 8 randomized images within each sample nerve area and calculating total nerve count using the measured nerve tissue area.

3.2.12 Preparation of NGCs for 14 mm gap rat model

To evaluate the performance of the S-design with GDNF gradients over a larger nerve gap (14 mm vs 7 mm) and a longer timeframe (12 weeks vs 4 weeks), we prepared nerve guides identically to the previous set of groups, but with a few small changes. The same outer conduits were prepared, but were cut to 15mm to be consistent with the control groups. The aligned fiber layer was also identically prepared, but cut to a length of 14mm. The gradient gelation parameters were likewise modified to accommodate the longer gradient length, though the 600ng/tube loading of GDNF was maintained, for both the uniform and gradient groups.

3.2.13 Preparation of NGCs for 20mm gap dog model

In order to evaluate our conduit designs in a more rigorous pre-clinical model, we prepared NGCs for repairing the peroneal nerve in a canine model. The dog model has several key distinctions from the rat model that improves its predictive power for how a treatment will work in humans. Firstly, the immune and cellular responses are more similar between dogs and humans than rats and humans. Secondly, the dog model allows us to repair larger nerves than are available in the rat model that are closer to the sizes needed for repairing nerves like the medial nerve in humans. Thirdly, the dog model allows for testing longer gaps, where guidance cues are especially necessary. Finally, the dog model allows for testing the response when the regenerating nerve must travel a

further distance beyond the nerve conduit to reach the distal target, which also requires longer study timepoints. The NGCs were prepared identically to the previous rat S-design NGCs, though with some slight variations. To accommodate the larger nerve diameter, the inner diameter of the conduit was raised from 1.5 mm to 2.0 mm. The conduits were also sized to be 22 mm in length, so that each nerve end can be inserted 1 mm into the NGC and then have a gap of 20 mm. The fiber sheets were also cut into longer lengths, leaving 20 mm between nerve ends. Finally, the hydrogel properties were tweaked to create gradients that bridged the larger gap distance, while still maintaining the 600ng/tube loading level for the uniform-loading and gradient groups.

3.3 Results & Discussion

3.3.1 Gelatin-based spiral NGC design

Eight groups of NGCs were prepared and successfully implanted into rat sciatic nerves for analysis. The overall design and a microtome section that is representative of the groups can be seen in Fig 3.1. The groups performed poorly in their nerve repair, as seen in their histological slides (Fig 3.2). The nerve area and myelinated axon count were both very low in almost every animal. The gelatin spiral did not provide the intended additional surface area of aligned fibers, as the layers packed together into the outer wall. This may be the product of hoop stress generated by how the sheets were crosslinked while flat, not curved. The release profile of the growth factors was difficult to control, and the gelatin swelling degree and degradation rate were more variable than desired. The design also did not allow for the heat-treatment that may be necessary for obtaining

adequate strength in the nerve guide, since the outer tube was directly spun onto the spiral bundle, components of which cannot handle the temperatures of the heat treatment. Considering the generally poor regeneration, we could not make any conclusive statement from comparing the groups other than that aligned nanofibers and GDNF can both greatly improve regeneration. For all of these reasons, we modified the design for the next set of experiments.

3.3.2 Fibrin-based spiral NGC design

The fibrin-based spiral NGC was designed to address many of the problems of the previous tier of gelatin-based NGCs through several means: The gelatin was replaced with fibrin, which should not collapse together outwards and was used at a concentration that the literature indicated was cell-permeable. The growth-factor delivery was transferred to a rolled film of the same PVA-collagen hydrogel used previously in our lab. Finally, the outer tubes were pre-fabricated, which allowed for strengthening through heat-treatment as well as more efficient manufacturing. These key features can be seen in Fig. 3.3. The design changes were an engineering success, in that they maintained a much more even distribution of nanofibers within the NGC lumen. In general, the fibrin-based spiral NGCs offered superior regeneration to the gelatin spirals, with an increased number of myelinated axons. However, there were several issues observed based on the results. While the concentration of the Tisseel-based fibrin gels were chosen because they have been shown to be cell permeable in the literature, the cells were largely seen elsewhere in the nerve guide from the fibrin and fiber layers. Cells mostly did not enter

the hydrogel-fiber composite likely due to the high density of hydrogel used here. Since the nanofibers themselves were largely unobserved by the regenerating cells and especially axons, the group comparisons between fiber characteristics did not lead to any conclusions about ideal fiber composition.

3.3.3 S-Shaped NGC design

The resistance of the regenerating nerve cells to enter dense areas caused us to redesign our NGCs again, with the new goal of ensuring a permissive environment where the proximal nerve stump enters the nerve guide. The S-design was chosen as an option since it had a mostly open, cell permissive lumen while still increasing the surface area of aligned nanofibers (Fig 3.4). The gap length was shortened to 7 mm together with a challengingly short 4 week timepoint in order to quickly identify designs that allow for quick migration of Schwann cells and nerve tissue into and across the nerve gap. The "S"-configuration produced impressive results, with both large pockets of the conduit filled with large areas of regenerating nerve, including large areas dense with myelinated axons (Fig 3.5). The vast improvement seen with this design encouraged us to adopt this S configuration for our later studies.

3.3.4 NF gradient generation

To generate NF gradient-containing hydrogels, we utilized a single channel microfluidics method developed by the Khademhosseini lab previously [26], which

allows for generation of gradients of tailorable concentration ranges and gradient length scales, which are then encapsulated within UV-crosslinked methacrylated gelatin strip (Fig. 3.6a). In brief, the gradient generation platform utilizes a single microfluidics channel with an inlet and outlet at opposite ends of the channel. The channel is filled with a hydrogel precursor solution and a large droplet is pipetted over the outlet. A small volume of NF solution is pipetted onto the inlet and driven into the channel through surface tension-driven flow. Combined with evaporation-driven backflow, a gradient is generated that can be immobilized through UV-activated polymerization of the hydrogel. By controlling the pre-loaded NF concentration and the concentration of NF in the droplet, linear gradients of controllable concentration ranges and multi-centimeter length scales can be generated as seen in Fig. 3.6b. After immobilization of NF gradients within the hydrogel strips, the NFs can be released in a spatially controlled manner depending on the region of hydrogel, in which the NFs are immobilized. Fig. 3.6c depicts the diffusion of lysozyme as a model protein out of the hydrogel. As expected, the regions of the hydrogel with higher loading concentration consistently released higher levels of the NF than the lower loading concentration regions of the gradient gels, even after several days. The release of NF continued in gradient fashion during the 2-week release study, though the release per day decreased over time. The gradient gels were configured to have a 14-day release profile so as to consistently provide a positive NF gradient while the endogenous Schwann cells and regenerating axons bridge the guidance conduit, which we assumed to occur primarily during the first one to two weeks of regeneration of peripheral neurons [31]. The levels of released NFs are then designed to taper off dramatically, so as to prevent the localized, high concentration that would cause the

"axonal trapping" that prevents nerves entering the distal stump. This degree of gradient generation and presentation control allows us to investigate the effects of numerous gradient characteristics (concentration range, steepness, and combination) in both *in vitro* and *in vivo* nerve guidance paradigms. It is worth noting that this method allows for the incorporation of various NF or combination of NFs into hydrogels. The scalable, versatile method of gel fabrication combined with the centimetre length-scale make these gels uniquely suited for *in vitro* migration screening experiments and for incorporation of NF gradients in nerve guidance conduits for *in vivo* nerve regeneration.

To investigate the effect of GDNF gradient delivery on Schwann cell migration velocity and directional guidance, we utilized an *in vitro* live cell-imaging platform incorporating both biochemical guidance from gradient hydrogels as well as topographical guidance from aligned nanofibers (Figure 3.7a). Aligned nanofibers were placed directly on top of gradient-containing hydrogel strip and a custom PDMS migration chamber was placed over the fiber/hydrogel construct to localize delivery of GDNF within the small volume of the chamber. Cells seeded on the fibers were tracked using time-lapse video microscopy on a programmable stage, allowing us to monitor cell migration over a large area of the gradient hydrogels (Figure 3.7b). We then analysed the migration of populations of cells within different regions of the GDNF gradients, compiling the individual cell tracks within each region to show the relative movement of each cell from its point of origin (Figure 3.7b). Using this method, we investigated the migration of human primary Schwann cells in response to three GDNF gradients of varied steepness to investigate the sensitivity of the Schwann cells to the gradients and to

determine the limitations in ability for the cells to detect and respond to the NF gradient. We selected uniaxially aligned electrospun poly(ε-caprolactone) (PCL) fibers for this study as our pilot experiment confirmed that cell migration was most effectively restricted to the direction of fiber alignment axis (Figure 3.7b). However, cell migration responses are relatively heterogeneous with a wide distribution of migration responses both towards and against the NF gradient in all three gradient steepness groups (Fig. 3.7c). Cells in the two lowest gradient steepnesses tested (2 μg/mL per cm and 10 μg/mL per cm) had median directedness values that were greater than 0.2, indicating biased movement toward the high end of the gradient. However, cells in the highest steepness, 20 μg/mL per cm, exhibited no directional bias with median directedness close to 0, and indicating that the steepness may be too great for the Schwann cells to detect the presence of a gradient. It should be noted that even in the lowest gradient steepness groups, the migration was largely heterogeneous with numerous cells migrating both towards and against the gradient. This demonstrates the need for further studies investigating a wider range of steepnesses to determine the gradient detection range for Schwann cells and to improve the efficacy of directional guidance. Nevertheless, these steepness studies suggest that steepness of the NF gradient is an important factor in cell migration guidance, thus it is necessary to tailor the gradient pattern to accelerate cell migration in the repair process. We also investigated the directional guidance of Schwann cells within different regions of the same gradient culture, determining if the cell response differs in gradients of the same steepness but different concentration ranges **(**Fig. 3.7d**).** Within the gradient range tested, Schwann cell migration velocity gradually increased as the average concentration of the gradient increased. Directional migration was apparent for all

gradient conditions in contrast to no GDNF and uniform GDNF (1 μg/mL) concentration conditions, although the highest average concentration (0.8 – 1.0 μg/mL) showed the strongest bias of cell migration towards the gradient. Nevertheless, it is likely that much lower and higher average GDNF concentration than this tested range could diminish the acceleration or directional migration due to limited receptor binding in low concentrations and receptor saturation in high concentrations, respectively. These results demonstrate the necessity to examine NF gradient concentration range and steepness for the optimization of direction guidance of neural cell migration, and the versatility of this gradient generation platform making it a powerful tool for such cell migration optimization studies.

This method is also suitable to generate NF gradient hydrogel strips with large sizes for *in vivo* testing. We next analysed the efficacy of these hydrogel-nanofiber constructs in a rat sciatic nerve regeneration model. The gradient gels were tested in a nerve guidance conduit with an "S" configuration to increase the contact area of regeneration axons and Schwann cells (Figure 3.8a), similar to a design tested in the spinal cord repair [32]. The aligned fibers (1.2 μm in diameter) were placed on both surfaces of the S-shaped hydrogel sheet with the GDNF gradient-loaded hydrogel strip placed in the centre of the conduit. This conduit was designed to provide both topographical (aligned fibers) and GDNF-gradient guidance cues. Here we tested groups with two different GDNF gradient patterns but the same total amount GDNF loaded inside our conduit, one with 600 ng GDNF per conduit with a steeper range of 0 – 400 μg/mL, and one with 600 ng GDNF per conduit with a gradient from 95.2 – 200 μg/mL.

As a control, the same total GDNF (600 ng) loaded uniformly inside the conduit was tested, together with another control group without GDNF. As a pilot experiment, we used a relatively short 7-mm nerve gap, and examined the regeneration outcome at a short time-point of 4 weeks. Representative histological images of the mid-point of the conduit at 4 weeks after repair are shown in Fig. 3.8. The GDNF-free group has few myelinated axons within the nerve area as compared to the GDNF-containing groups. The gradient-containing groups had a higher density of myelinated axons based on the Histomorphometric analysis (Fig. 3.8b). The presence of GDNF increased the area of the regenerating nerve, regardless of the gradient presentation, as the GDNF-containing groups had larger nerve areas than the GDNF-free group. However, GDNF gradient influenced the quality of the regeneration, as the steep gradient group had a higher axonal density, as well as higher nerve area, resulting in a much larger total axon count (Fig. 3.8c). The steep gradient group had an average myelinated axon count of 4046 ± 2464 axons per nerve, greater than the other groups with a shallow gradient (2085 ± 1569 axons), uniform GDNF loading (1610 ± 1656 axons), or no GDNF (1208 ± 1116 axons). This study indicates that gradient presentation of GDNF facilitates cell migration into the nerve guide, as seen in the increased nerve area and axonal density within the midpoint of the conduit, but that regeneration of the nerve is highly dependent on the concentration range of the gradient being delivered. Achieving robust regeneration into the midpoint of the nerve guide is a prerequisite for ultimately achieving functional recovery. We employed electrophysiology analysis to verify if the regenerating nerves were able to traverse the entire length of nerve guide, reinnervate the distal stump, and form functional connections in the target tissues. Nerve conduction from the sciatic notch to the ankle

was compared in the left, treatment leg to the right, uninjured leg of the same rat, with the resulting boxplot and individual data points shown in Fig. 3.8d. There was considerable variation within each group, reflecting the heterogeneous nature of nerve regeneration, particularly at early time points. Nonetheless, the steep gradient demonstrated the greatest functional recovery of the groups, with an average amplitude of 0.63 mV, which was 16.1% of control amplitude, higher than that of the no GDNF group (0.49 mV, 7.4%), uniform GDNF (0.38 mV, 3.16%) and shallow gradient (0.31 mV, 2.6%), respectively. The EMG measurement for the foot muscle was too small to discern at this time point. No significant differences were found between the groups for the velocity of the nerve signal. Given these promising results, assessments at longer time points are warranted.

3.3.5 The 14-mm gap rat model

The 14 mm gap model was chosen to better differentiate between designs, as guidance cues become more important as the nerve gap grows. From the previous 7 mm gap study, we expected the GDNF gradient group to outperform the other groups, due to potential synergies between two different guidance cues. After the 12 week study, all animals also had at least some myelinating axons visible within the conduit midpoint (Fig. 3.9). Every single conduit in every group had robust cell growth into the conduit, with nerve areas comparative or greater than those of the previously-run controls, Neuragen or a blank tube (Fig 3.10). When combining the nerve area with the density of myelinating axons, the uniformly loaded GDNF group has a much larger number of myelinated axons

per tube than the GDNF-gradient group or GDNF-free group, comparable or above the Neuragen positive control group (Fig 3.10).

The axons of the GDNF-gradient group were distributed differently than the axons of the other groups. Dense concentrations of myelinating axons can be seen in the immediate vicinity of the edge of the gradient gels (Fig 3.11) in most of the subjects of the GDNF gradient group. This phenomenon was not seen in the other groups, nor in the previous gradient groups. The large area of dense cells often contained almost no myelinating axons in this group, as well as the no-GDNF group. The gradient gels were placed in between fiber layers and not meant to directly interact with the axons, and it is unclear if this phenomenon is related to the decreased performance relative to the 7 mm gap experiment.

The electrophysiology data was likewise surprising (Fig. 3.12). The uniform-GDNF group had detectable CMAP responses in 5 out of 6 rats, while only one, very small response was seen in both the GDNF-gradient group and the no-GDNF group. The best treatment group, with uniform GDNF loading, had lower average amplitude than the Neuragen group, which had a detectable response in all 8 rats. The foot CMAP response is a much more difficult functional assay than the ankle test, since the axons must travel much further to reinnervate the foot muscles. Unlike the 7 mm gap study, motor ankle measurements were not taken because they had not been performed previously in the control groups.

The analysis of the atrophied distal muscles of the calf (soleus and gastrocnemius) correlated with the other analyses (Fig. 3.13). The group without GDNF had the poorest functional regeneration, as well as the fewest numbers of myelinated axons. The group also thus has the most atrophied muscles, as they have been poorly reinnervated to date.

The nerve area does not correspond to axon counts in these groups, as compared to Neuragen. The cues may be disproportionally attracting other cells than just the desired Schwann cells and axons. Moreover, the longer gap may together with the same total loading level means that a gradient must be less steep, and that the amount observable at the proximal stump will be lower. Possibly, the concentration of GDNF in the gradient group is too low to elicit the initial ingrowth necessary for regeneration. The canine study will hopefully elucidate whether the current gradient configuration is unsuitable for long gaps or whether the 14-mm gradient group underperformed for a different, as of yet unknown reason.

3.3.6 20 mm gap in a canine model of peripheral nerve repair

The nerve guides were successfully prepared and implanted into lower leg model of the canine, without major complications. The study design can be seen in Table 3.2. The histological and functional data should become available over the next few months.

3.4 Conclusion

In conclusion, we have developed a versatile and scalable NF gradient-generation method for studying and improving peripheral nerve repair. The NF gradient hydrogels were first used to demonstrate the unidirectional migration response of Schwann cells *in vitro*. Directional migration response was dependent on both the gradient steepness and concentration range, confirming the importance of control over gradient characteristics and delivery to maximize unidirectional cell migration. In a rat sciatic nerve repair model, we have shown that a steeper GDNF gradient yielded a higher count of myelinated axons and a higher density of axons within the nerve guidance conduit as compared with a shallower gradient and no gradient GDNF loading in an aligned fiber conduit. The steeper GDNF-gradient conduit further increased median amplitude in the ankle motor signal, with a few subjects showing dramatically higher functional recovery than any other group. These studies demonstrate that GDNF gradient can aid in Schwann cell migration and thus peripheral nerve repair, and that the concentration and steepness of the gradients needs careful tuning to maximize its efficacy. These results provide the rationale for future studies to validate the efficacy of GDNF gradient optimization in critical gap repair models using our nerve conduits combining NF gradient delivery and aligned fiber contact guidance. This gradient generation platform may be used to determine the mechanisms by which neurons and Schwann cells respond to gradients of different NFs, and study potential synergistic effects of topographical and biochemical gradient guidance to accelerate the regrowth of nerves across the nerve gap. More optimization may be necessary, however, to produce the ideal conditions for every stage of nerve regeneration (recruitment into NGC, migration across the gap, reinnervation of the distal stump, and finally travelling to and reinnervation of the target tissue). For

longer gaps, the 14 mm gap experiment indicates that special care must be taken to ensure there is sufficient GDNF present at the proximal stump to attract the axons into the conduit, while still maintaining a guiding gradient. This could be achieved several ways, such as by having a burst release of GDNF immediately upon implantation, and while the gradient-loaded gel would be able to establish a gradient in the conduit over the first several days. Alternatively, the range and steepness of the gradient could be adjusted to a non-zero level at the low end of the gradient.

3.5 Figures

	Groups	# rats	nerve gap (mm)	study length (weeks)	Fiber Distribution	Aligned Fiber Density	Fiber Diameter (nm)	Composition % of Gelatin (PCL is Remainder)	GDNF Loading (ng/tube)	Implantation Date
	1	8	14	8	spiral no fiber				0	
	2	8	14	8	Single Layer	medium	760	0	0	
Tier 1	3	8	14	8	Spiral	medium	760	0	0	Jun-12
	4	8	14	8	Spiral	high	760	0	0	
	5	8	14	8	Spiral	low	760	0	0	
	6	6	14	8	Spiral	medium	760	0	20	
	7	6	14	8	Spiral	medium	760	0	200	Oct-12
Tier 2	8	6	14	8	Spiral	medium	760	0	2000	
	9	6	14	8	Fibrin Spiral	medium	**1200**	0	600	3/5/13
	10	6	14	8	**Fibrin Spiral**	medium	760	0	600	3/7/13
Tier 3	11	6	14	8	Fibrin Spiral	medium	**400**	0	600	3/8/13
	12	6	14	8	Fibrin Spiral	medium	760	**90**	600	3/12/13
	13	6	14	8	Fibrin Spiral	medium	760	**80**	600	3/13/13
	14	4	7	4	**Microfibers**	medium		0	~600 via microfibers	5/6/13
Tier 4	15	4	7	4	**Fringe Spiral**	medium	1200	0	~600 via microfibers	5/6/13
	16	4	7	4	**"S" open design**	medium	1200	0	~600 via microfibers	5/7/13
	17	8	7	4	S design	medium	1200	0	**Uniform**	6/13 & 8/14
Tier 5	18	8	7	4	S Design	medium	1200	0	**Shallow Gradient 60-180**	6/13 & 8/14
	19	8	7	4	S Design	medium	1200	0	**Steep Gradient 1-240**	6/28/13
	20	8	7	4	**1 layer**	medium	1200	0	Steep Gradient 1-240	10/8/13
	21	8	7	4	S design	medium	1200	0	**NONE**	8/13/14
	22	8	14	8	S design	medium	1200	0	uniform 600ng	9/24/14
Tier 6	23	8	14	8	S design	medium	1200	0	Gradient of 600ng	9/25/14
	24	8	14	8	S design	medium	1200	0	NONE	9/26/14

Table 3.1: Treatment groups for peripheral nerve repair tested in rats

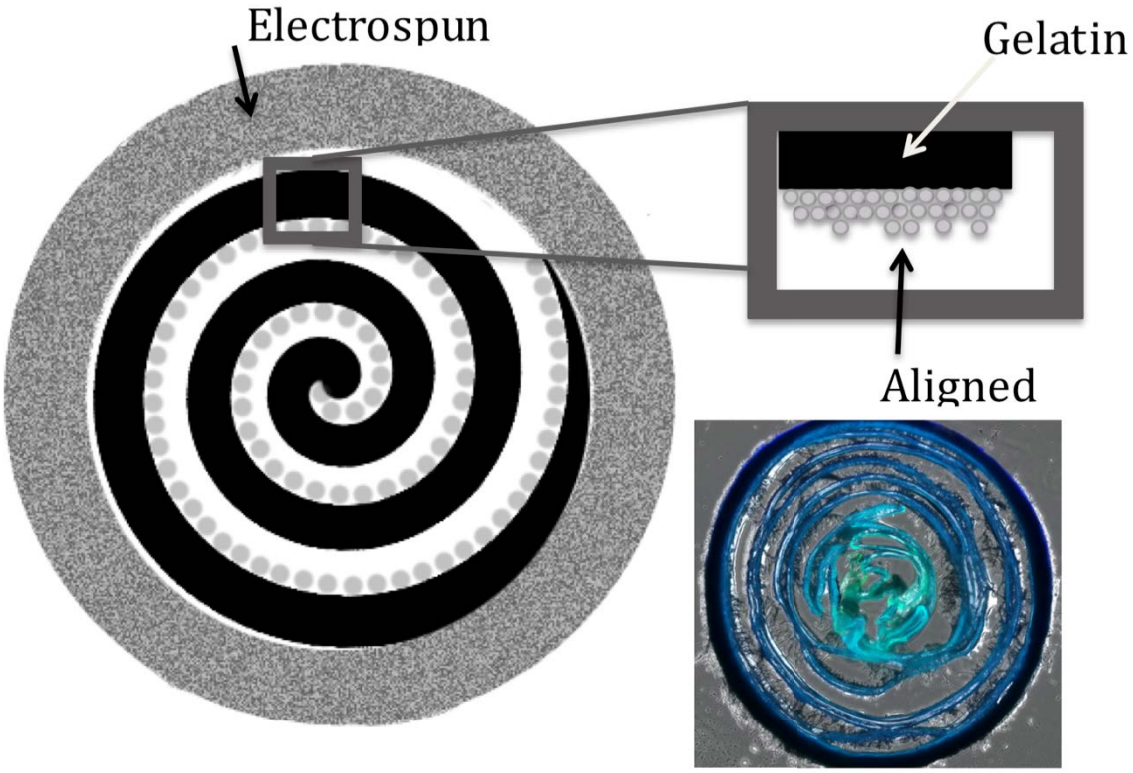

Figure 3-1: Design of Gelatin-based spiral NGC

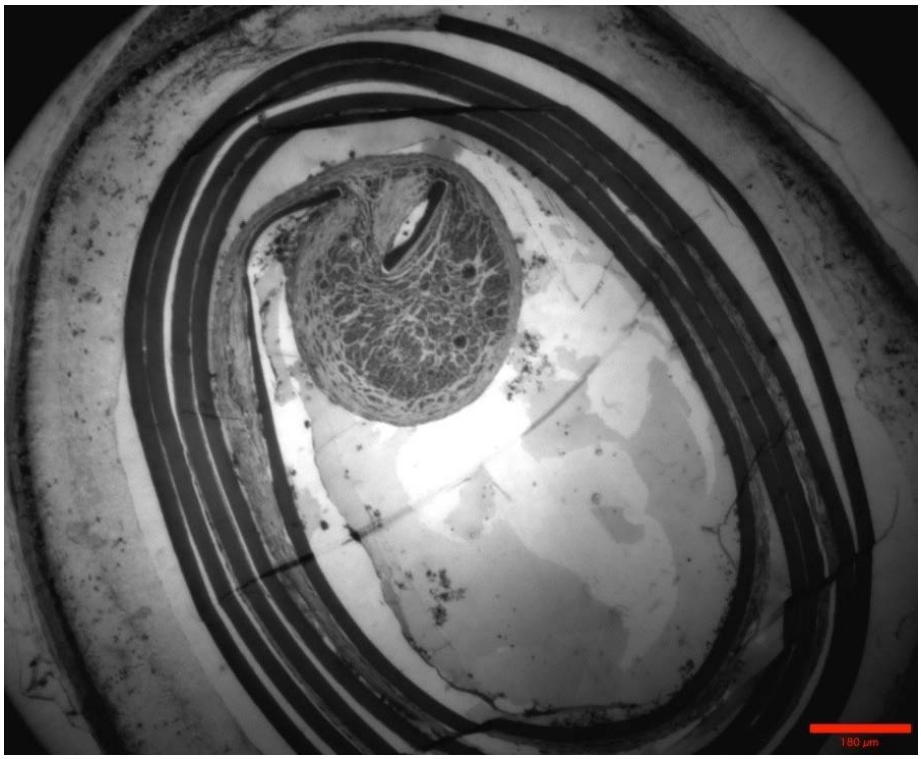

Figure 3-2: Gelatin Spiral NGCs underperform in vivo.

The groups 1-8 resulted in poor nerve regeneration in vivo, with small nerve areas within the conduits and few myelinated axons, as seen in this representative micrograph of a conduit after 8 weeks in vivo. Note the collapsed spiral fiber layers.

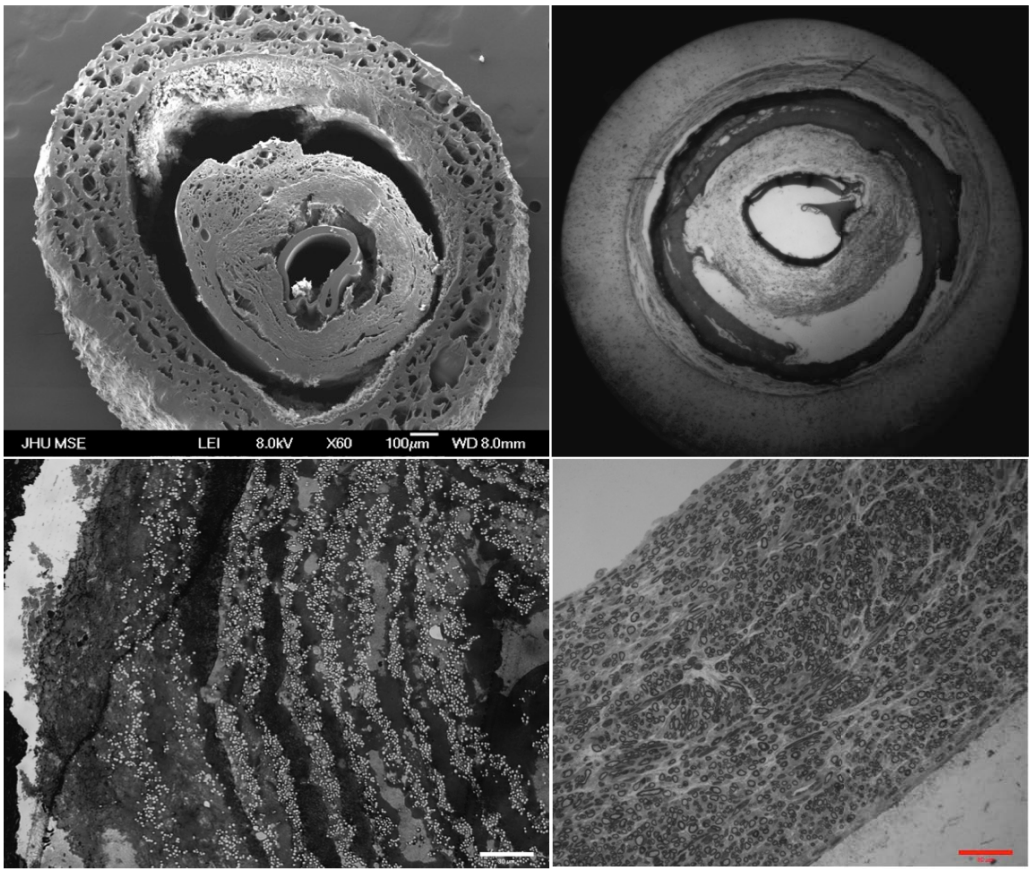

Figure 3-3: Fibrin spiral design and performance in vivo.

Clockwise from top left: SEM image of completed fibrin spiral. Top right: low magnification micrograph of fibrin spiral after 12 weeks in vivo. Note the dark band for the GDNF-releasing PVA-hydrogel and inner layers of aligned nanofibers. The innermost, dark layer is PVA leftover from use in the spiral-wrapping procedure. Bottom right: Higher magnification micrograph of conduit after 12 weeks in vivo. The conduit has regions with dense concentrations of myelinated axons, but they are separate from the fiber areas. Bottom left: the fibrin-aligned fiber layers after 12 weeks in vivo. Note the ordered spacing between layers, but also the lack of cellular or axonal association with the fiber layers.

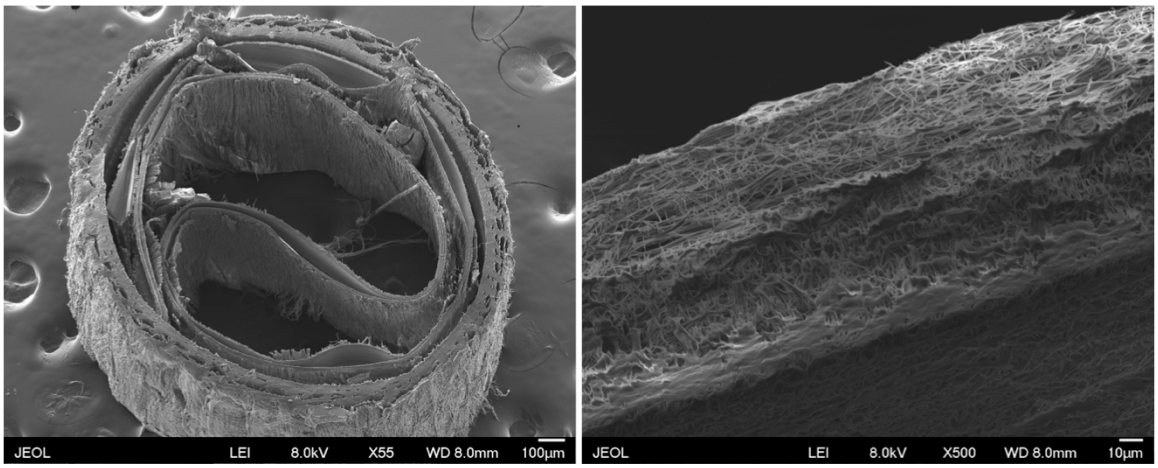

Figure 3-4: SEM images of the S-Shaped NGC (group 16)

Left: The overall view of the conduit, with the layers of aligned fibers evident in the conduit lumen. Right: The semiporous Nanofibrous outer wall maintains its porosity after heat-treatment to increase its mechanical strength.

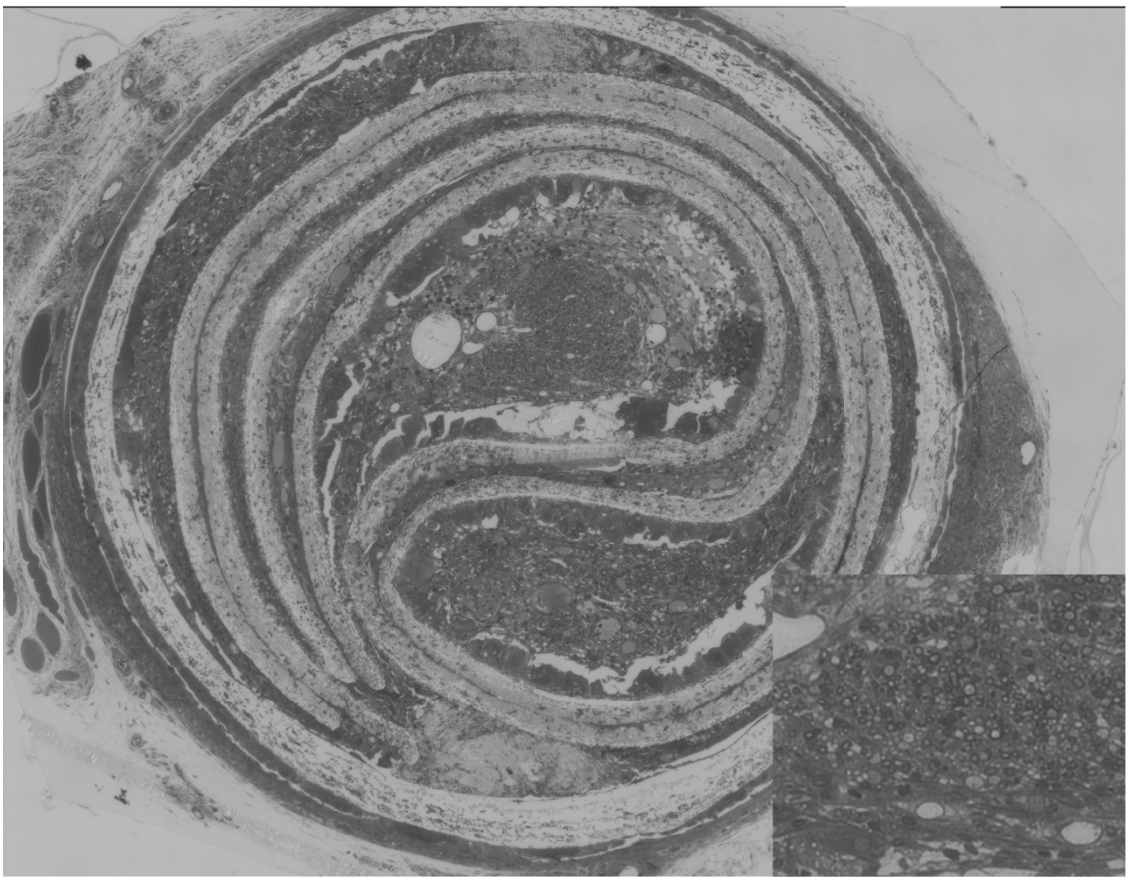

Figure 3-5: Histological assessment of S-Shape NGC after 4 weeks in vivo.

Note the large area of the regenerated nerve, with dense areas of myelinated axons in both fascicles (inset)

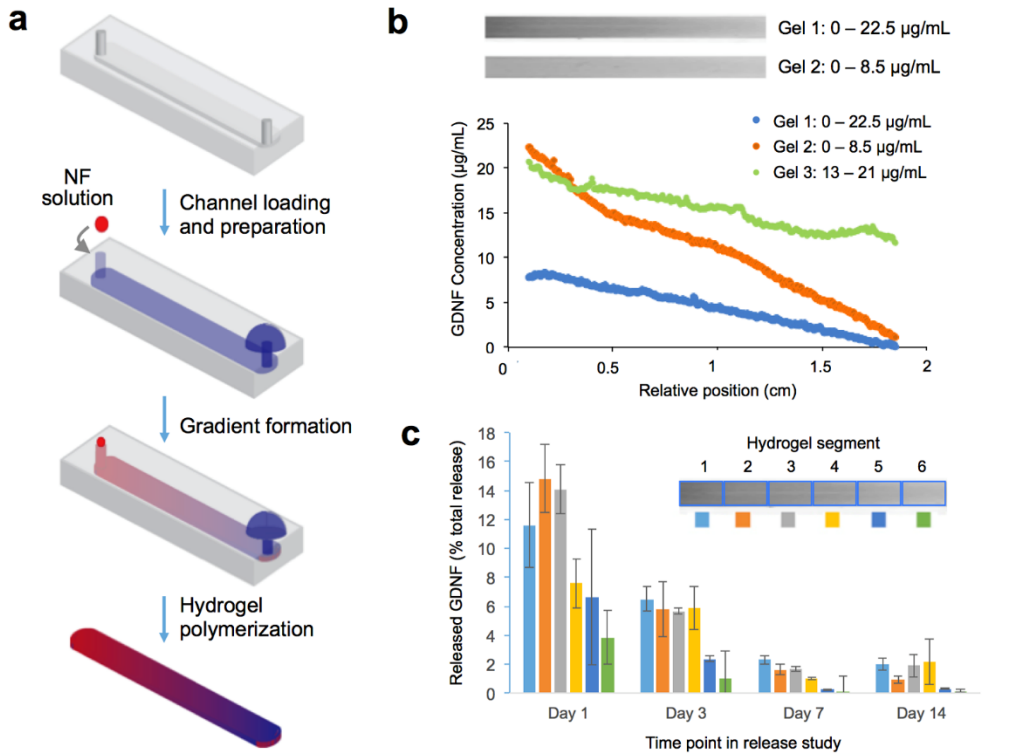

Figure 3-6: Gradient generation method and characterization.

(a) PDMS channel filled with hydrogel precursor solution, NF solution flowed into channel to form gradient, and hydrogel polymerized with UV; (b) Characterization of gradients with different GDNF loading concentration ranges; (c) GDNF release from different segments of gradient hydrogel over 14 days.

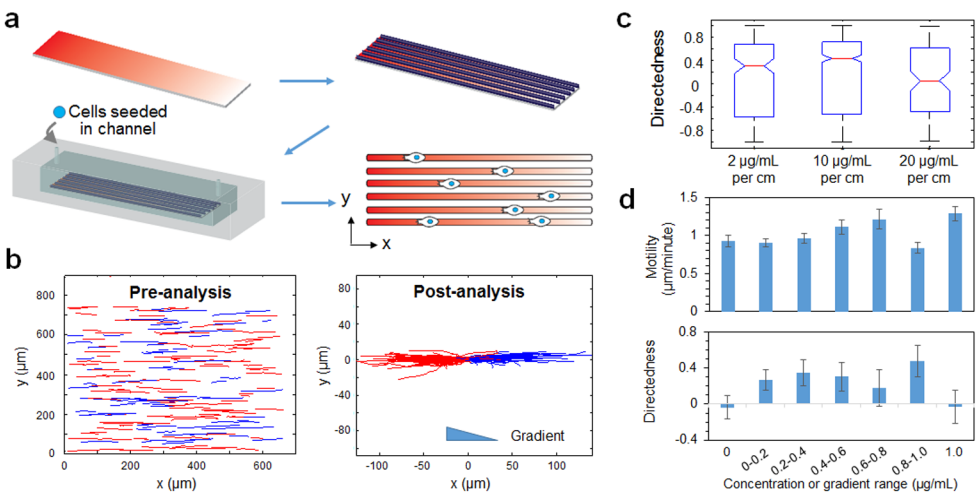

Figure 3-7: Effects of GDNF steepness and concentration range on Schwann cell motility and directedness.

(a) Schematic showing of the setup for single cell tracking. Aligned PCL fibers (1.2 µm diameter) were placed over a gelatin hydrogel loaded with different GDNF gradient patterns. This aligned fiber-hydrogel strip construct was then enclosed within a migration chamber of dimensions 4 mm by 10 mm by 0.1 mm. Cells were seeded on the substrate by flowing cell suspension in medium into the chamber. Cell migration characteristics were tracked over the entire substrate surface. (b) Cell migration characteristics between two consecutive frames were recorded and reformatted to normalize to the same point-of-origin for the convenience of analysis. (c) Migration bias of Schwann cells in response to different levels of gradient steepness. (d) Motility and directedness of Schwann cells in response to different gradient concentration ranges in the same chamber.

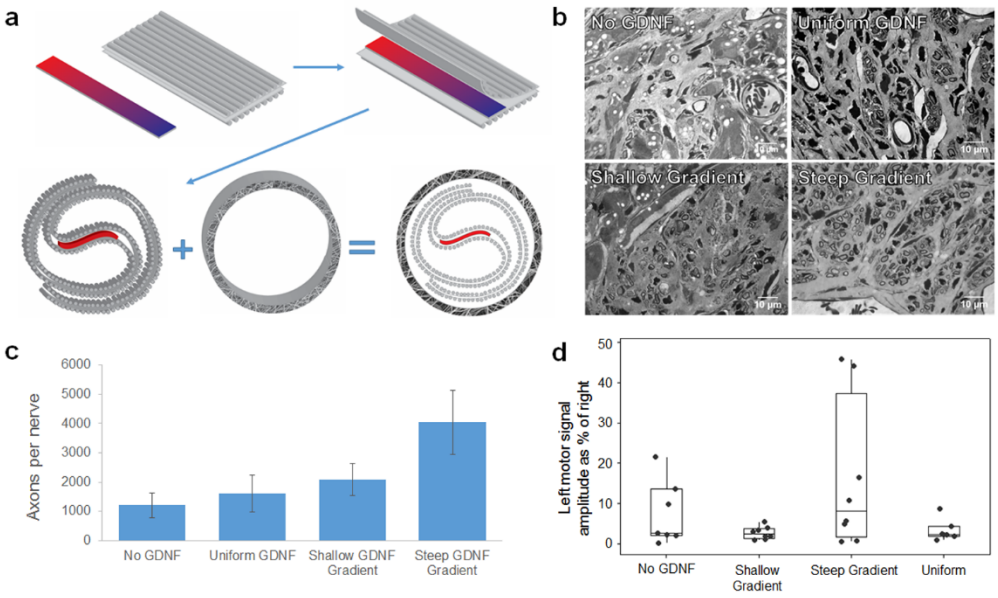

Figure 3-8: Effects of GDNF gradient presentation on nerve regeneration in a rat sciatic nerve repair model.

(a) Schematic illustration for construction of the S-shaped nerve guidance conduit incorporating aligned PCL fibers and GDNF gradient hydrogel. Nerve conduit was created by placing a hydrogel strip with a GDNF gradient between aligned PCL fiber sheets, formed into an S-shaped roll, and placed within a randomly aligned electrospun cylindrical conduit. (b) Representative *in vivo* axonal outgrowth in a 7-mm sciatic nerve gap injury in conduits without GDNF, with uniform GDNF, and with shallow or steep GDNF gradients showing highest quantity of myelinated axons in the steep gradient group. Scale bars = 10 μm. (c) Axon count in entire luminal space of each conduit group. (d) Motor signal quantification in injured leg for each conduit group compared to motor signal of opposite (healthy) leg.

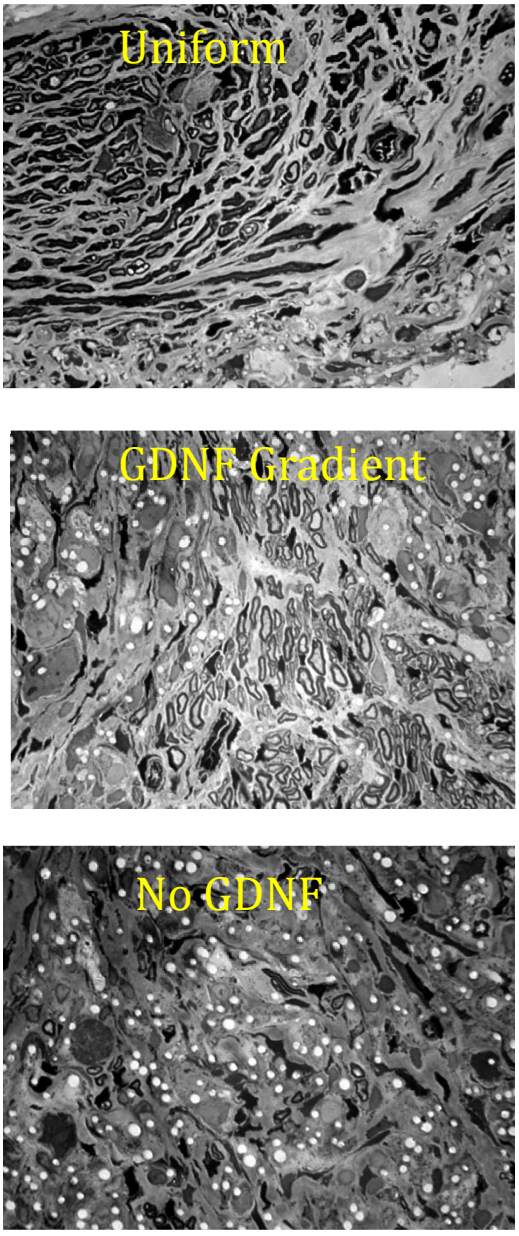

Figure 3-9: Histology images of 14 mm gap NGCs after 12 weeks in vivo.

Note the large cellular response, but lack of myelinated axons in the No GDNF group.

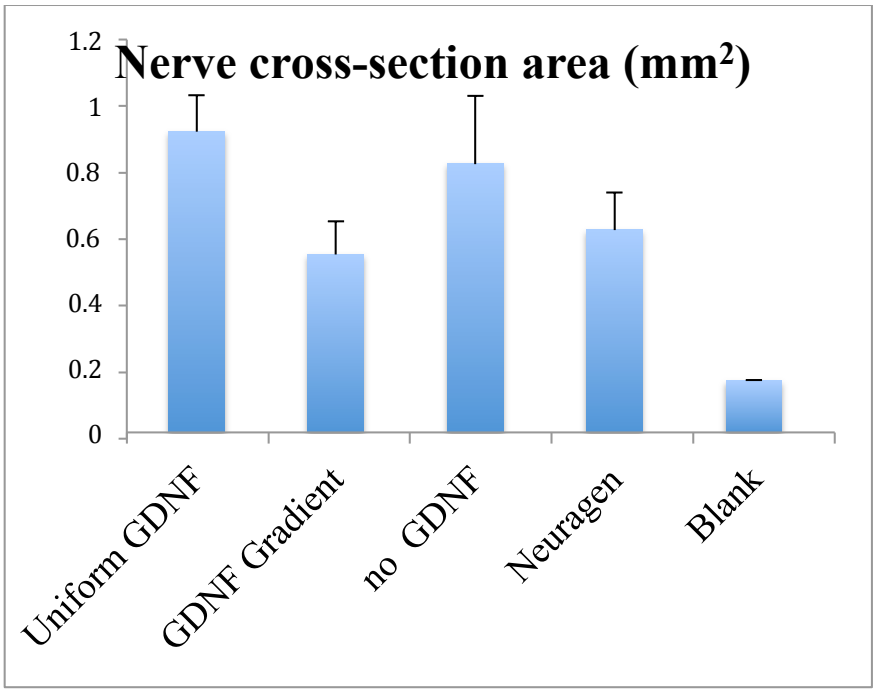

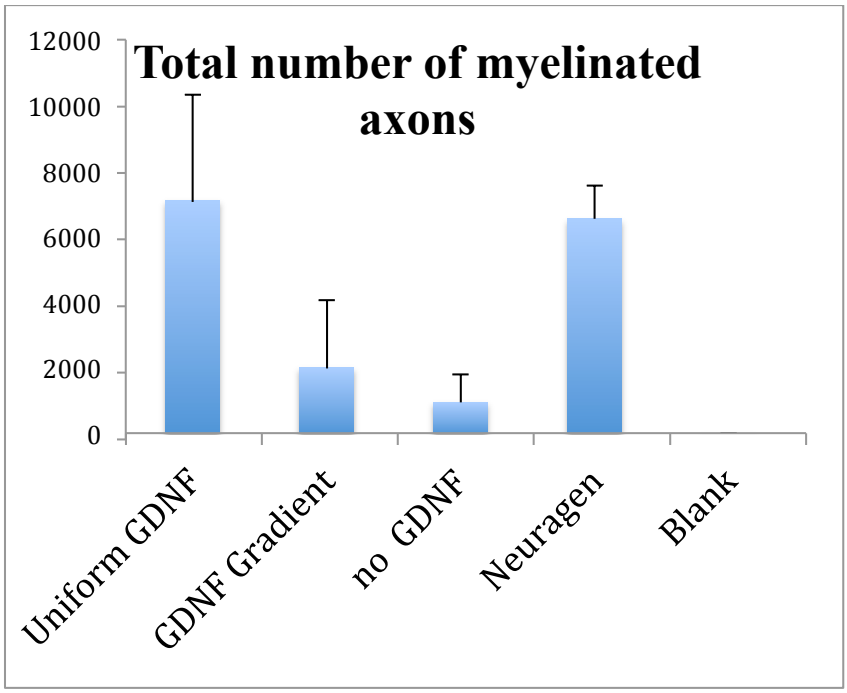

Figure 3-10: Quantification of the histological images of the 14 mm gap NGCs.

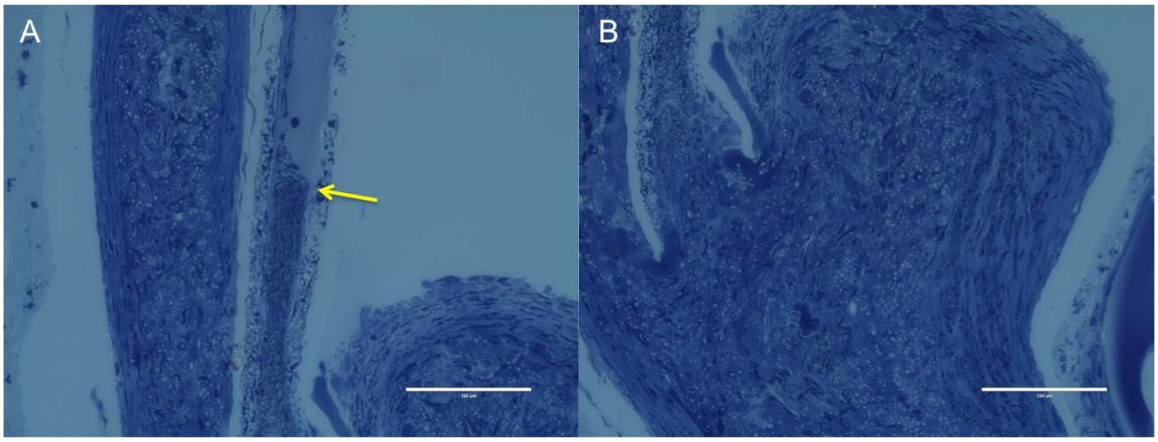

Figure 3-11: Histology image of GDNF-gradient group in 14 mm gap NGC.

A: Dense concentrations of myelinating axons can be seen in the immediate vicinity of the edge of the gradient gels (yellow arrow) in most of the subjects of the GDNF gradient group. This phenomenon was not seen in the other groups, nor in the previous gradient groups. B: The large area of dense cells often contained almost no myelinating axons in this group. The gradient gels were placed in between fiber layers and not meant to directly interact with the axons. Scalebar = 100 μm

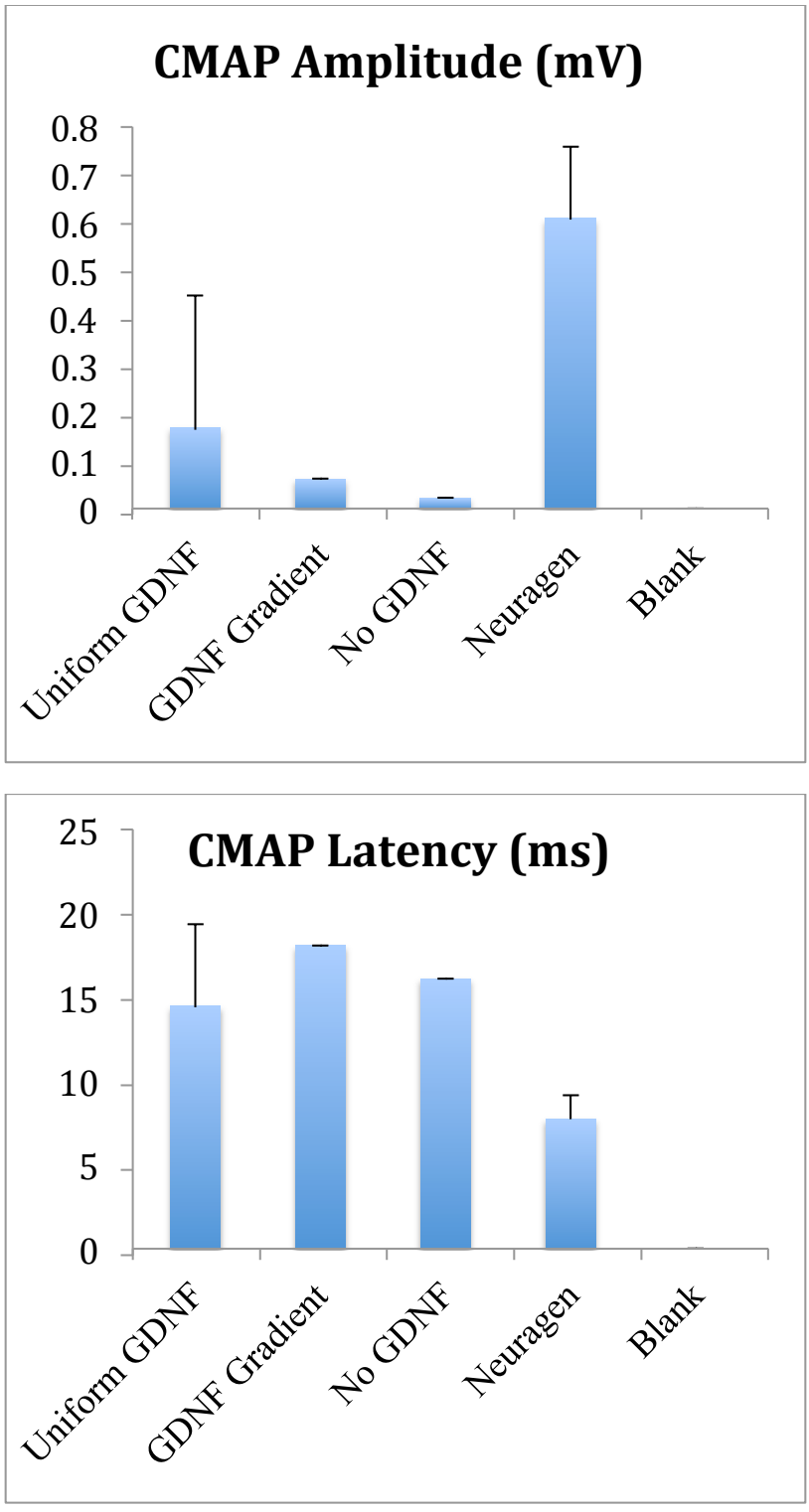

Figure 3-12: Electrophysiology results for 14 mm gap NGCs after 12 weeks in vivo

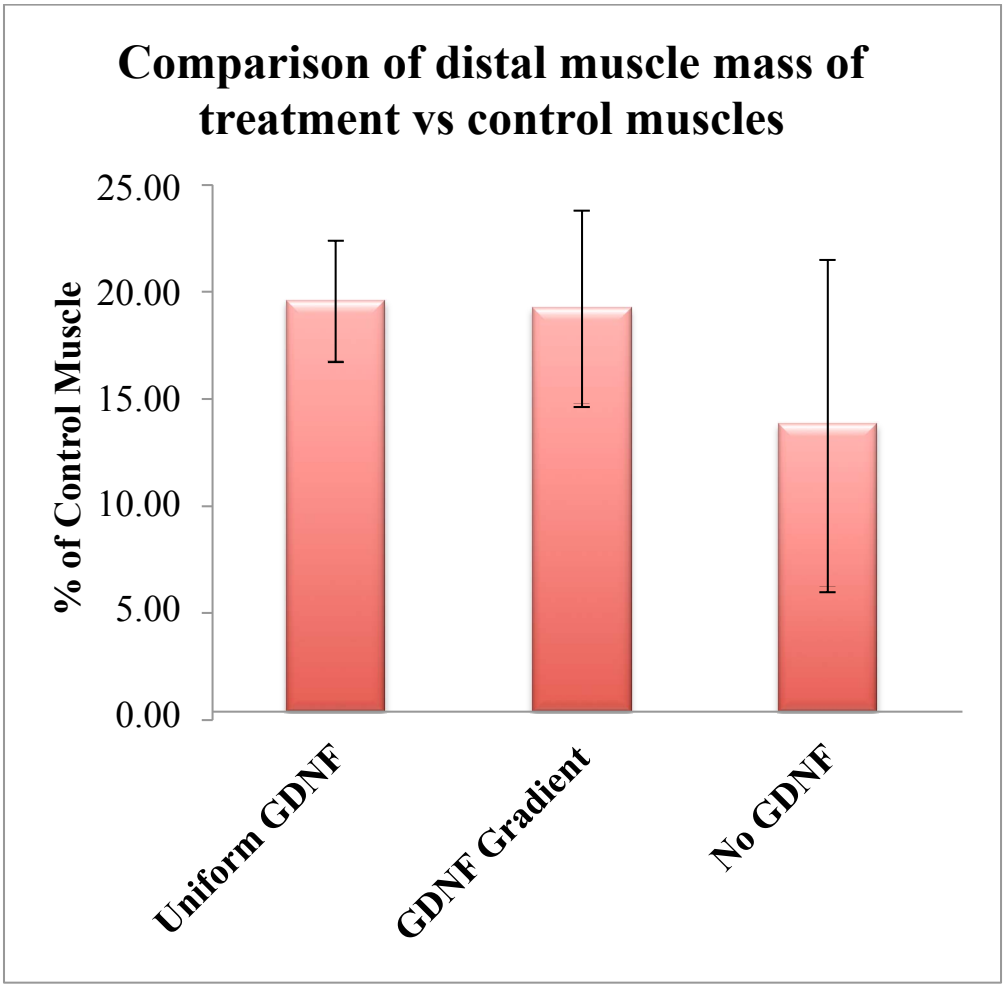

Figure 3-13: Distal muscle atrophy after 12 weeks in 14 mm gap model.

For each rat, the weights of the gastrocnemius and soleus muscles are compared between the left, treatment leg and the right, control leg. Each bar represents the average of the group. Note the greater atrophy in the GDNF-free group, which correlates with the poor number of myelinated axons seen in the histological results for this group.

Groups	# dogs (2 tubes/dog)	nerve gap (mm)	Fiber Distribution	Fiber Diameter (nm)	GDNF Loading (ng/tube)	Implantation Date
Autograft	5	20			NONE	
Neuragen	5	20			NONE	Jun-14
NGCs	5	20	S design	1200	NONE	Jun-14
NGCs	5	20	S design	1200	Uniform (600ng/tube)	Oct-14
NGCs	5	20	S design	1200	Steep Gradient 1-240	Jan-15

Table 3.2: Study design for the canine peripheral nerve injury model.

3.6 References

1. Noble, J., et al., *Analysis of upper and lower extremity peripheral nerve injuries in a population of patients with multiple injuries.*, in *J Trauma*. 1998. p. 116-122.
2. Belkas, J.S., M.S. Shoichet, and R. Midha, *Peripheral nerve regeneration through guidance tubes*, in *Neurological Research*. 2004. p. 151-160.
3. Evans, G.R., *Peripheral nerve injury: a review and approach to tissue engineered constructs.*, in *Anat. Rec.* 2001. p. 396-404.
4. Kehoe, S., X.F. Zhang, and D. Boyd, *FDA approved guidance conduits and wraps for peripheral nerve injury: a review of materials and efficacy.*, in *Injury*. 2012. p. 553-572.
5. Kim, Y.-t., et al., *The role of aligned polymer fiber-based constructs in the bridging of long peripheral nerve gaps.*, in *Biomaterials*. 2008. p. 3117-3127.
6. Bozkurt, A., et al., *The role of microstructured and interconnected pore channels in a collagen-based nerve guide on axonal regeneration in peripheral nerves.*, in *Biomaterials*. 2012. p. 1363-1375.
7. Arai, T., G. Lundborg, and L.B. Dahlin, *Bioartificial nerve graft for bridging extended nerve defects in rat sciatic nerve based on resorbable guiding filaments.*, in *Scand J Plast Reconstr Surg Hand Surg*. 2000. p. 101-108.
8. Yoshii, S., et al., *Bridging a 30-mm nerve defect using collagen filaments.*, in *J Biomed Mater Res A*. 2003. p. 467-474.
9. Clements, I., et al., *Thin-film enhanced nerve guidance channels for peripheral nerve repair*, in *Biomaterials*. 2009. p. 3834-3846.
10. Hsu, S.-h. and H.-C. Ni, *Fabrication of the microgrooved/microporous polylactide substrates as peripheral nerve conduits and in vivo evaluation.*, in *Tissue Eng Part A*. 2009. p. 1381-1390.
11. Eggers, R., et al., *Lentiviral Vector-Mediated Gradients of GDNF in the Injured Peripheral Nerve: Effects on Nerve Coil Formation, Schwann Cell Maturation and Myelination*, in *PLoS ONE*. 2013. p. e71076.
12. Tannemaat, M.R., et al., *Differential effects of lentiviral vector-mediated overexpression of nerve growth factor and glial cell line-derived neurotrophic factor on regenerating sensory and motor axons in the transected peripheral nerve*, in *European Journal of Neuroscience*. 2008. p. 1467-1479.
13. Blits, B., et al., *Rescue and sprouting of motoneurons following ventral root avulsion and reimplantation combined with intraspinal adeno-associated viral vector-mediated expression of glial cell line-derived neurotrophic factor or brain-derived neurotrophic factor.* Experimental neurology, 2004. **189**(2): p. 303-316.
14. Hoyng, S.A., et al., *A comparative morphological, electrophysiological and functional analysis of axon regeneration through peripheral nerve autografts genetically modified to overexpress BDNF, CNTF, GDNF, NGF, NT3 or VEGF*. Experimental neurology, 2014. **261**: p. 578-593.
15. Moore, A.M., et al., *Controlled Delivery of Glial Cell Line–Derived Neurotrophic Factor Enhances Motor Nerve Regeneration.* The Journal of hand surgery, 2010. **35**(12): p. 2008-2017.

16. Wood, M.D., et al., *Fibrin gels containing GDNF microspheres increase axonal regeneration after delayed peripheral nerve repair.* Regenerative medicine, 2013. **8**(1): p. 27-37.
17. Mai, J., et al., *Axon initiation and growth cone turning on bound protein gradients.* The Journal of Neuroscience, 2009. **29**(23): p. 7450-7458.
18. Laura, M., F.D. Miller, and M.S. Shoichet, *The use of immobilized neurotrophins to support neuron survival and guide nerve fiber growth in compartmentalized chambers.* Biomaterials, 2010. **31**(27): p. 6987-6999.
19. Fricke, R., et al., *Axon guidance of rat cortical neurons by microcontact printed gradients.* Biomaterials, 2011. **32**(8): p. 2070-2076.
20. Joddar, B., et al., *Spatial gradients of chemotropic factors from immobilized patterns to guide axonal growth and regeneration.* Biomaterials, 2013. **34**(37): p. 9593-9601.
21. Dodla, M. and R. Bellamkonda, *Differences between the effect of anisotropic and isotropic laminin and nerve growth factor presenting scaffolds on nerve regeneration across long peripheral nerve gaps*, in *Biomaterials*. 2008. p. 33-46.
22. Tang, S., et al., *The effects of gradients of nerve growth factor immobilized PCLA scaffolds on neurite outgrowth in vitro and peripheral nerve regeneration in rats.* Biomaterials, 2013. **34**(29): p. 7086-7096.
23. Bunge, R.P., *The role of the Schwann cell in trophic support and regeneration*, in *Journal of neurology*. 1994, Springer. p. S19-S21.
24. Fu, S. and T. Gordon, *The cellular and molecular basis of peripheral nerve regeneration*, in *Mol Neurobiol*. 1997. p. 67-116.
25. Ide, C., et al., *Schwann cell basal lamina and nerve regeneration.* Brain Research, 1983. **288**(1): p. 61-75.
26. Du, Y., et al., *Rapid generation of spatially and temporally controllable long-range concentration gradients in a microfluidic device.* Lab on a Chip, 2009. **9**(6): p. 761-767.
27. Van Den Bulcke, A.I., et al., *Structural and rheological properties of methacrylamide modified gelatin hydrogels.* Biomacromolecules, 2000. **1**(1): p. 31-38.
28. Nichol, J.W., et al., *Cell-laden microengineered gelatin methacrylate hydrogels.* Biomaterials, 2010. **31**(21): p. 5536-5544.
29. Ren, Y.-J., et al., *Enhanced differentiation of human neural crest stem cells towards the Schwann cell lineage by aligned electrospun fiber matrix.* Acta biomaterialia, 2013. **9**(8): p. 7727-7736.
30. Chew, S.Y., et al., *Aligned Protein-Polymer Composite Fibers Enhance Nerve Regeneration: A Potential Tissue-Engineering Platform.*, in *Adv. Funct. Mater.* 2007. p. 1288-1296.
31. Mackinnon, S.E. and A.R. Hudson, *Clinical application of peripheral nerve transplantation.* Plastic and reconstructive surgery, 1992. **90**(4): p. 695-699.
32. Hurtado, A., et al., *Robust CNS regeneration after complete spinal cord transection using aligned poly-l-lactic acid microfibers*, in *Biomaterials*. 2011, Elsevier Ltd. p. 6068-6079.

Chapter 4 Nanofiber-based Scaffolds for Ventral Root Avulsion Repair

4.1 Background

In the clinical treatment of traumatic spinal cord injury (SCI), there is a major unmet need for effective regeneration strategies for injuries to the conus medullaris (CM) and lumbosacral nerve roots (cauda equine (CE)) [1]. These occur in approximately 20% of all SCI cases that involve trauma to the thoracolumbar junction of the spine or to the lumbar spine [2-4]. In these cases, the lumbosacral nerve roots may be avulsed, torn, lacerated, stretched, or crushed. Automobile accidents account for the majority of CM/CE accidents [5-7]. These CM/CE injuries result in a lower motor neuron syndrome, wherein distal peripheral nerve targets, including skeletal muscles, sensory organs, and autonomic ganglia, are denervated. The paralysis of the lower extremities may result in symptoms including the loss of voluntary bladder and bowel control due to loss of the neuronal circuits responsible for bladder contractions and external sphincter control [8, 9]. Recovery of this control is ranked as one of the highest priorities among the SCI population [10]. However, there are currently no effective treatments for CM/CE injuries. In fact, CM/CE patients are often excluded from treatment trials for SCI, due to their different, predominantly lower motoneuron injury presentation.

Our collaborators in Dr. Havton's lab have developed a rat cauda equina injury model, which recapitulates several key features of the clinical CM/CE presentation. The model consists of a lumbosacral ventral root avulsion (VRA) injury, which leads to the

progressive death of motoneurons and autonomic neurons through apoptosis and necrosis [11, 12]. The Havton lab has demonstrated that surgically reimplanting the avulsed ventral roots into the lateral funiculus of the CM is neuroprotective of the axotomized neurons and promotes axonal regeneration of lesioned spinal cord axons into the reimplanted roots. This reinnervation resulted in functional recovery in the lower urinary tract with the recovery of reflexive micturition and decreased neuropathic pain [13-18]. While that work demonstrates the potential benefits to ventral root reimplantation, this technique is not directly applicable in the clinical setting, since in a trauma setting, the ventral roots will retract caudally and the injury will progress along the course of the severed roots. These complications make it difficult or impossible to directly reimplant the severed roots, requiring new tissue engineering approaches to bridge the resulting tissue gap. We propose the use of peripheral nerve grafts or biomaterial-based scaffolds to bridge the gap between the avulsed root and the CM. Peripheral nerve grafts are the current gold standard for bridging gaps in peripheral nerve injuries, with a long history of improved, if limited, functional regeneration [19]. The harvesting procedure, however, necessarily requires additional surgeries and deficits at the donor site, producing sensory and motor deficits and potentially neurologic pain and neuromas. The sensory nerve graft is used more commonly than mixed or motor nerve grafts due to decreased donor site morbidity associated with sensory nerve grafts. However, the sensory grafts are phenotypically different from motor grafts and are less supportive of motoaxonal regeneration than motor or mixed nerve grafts [20]. Our lab has been researching synthetic biomaterials for guiding the regenerating nerve over the gap without having to rely upon autologous grafts [21, 22]. This study seeks to extend our peripheral nerve

repair work to bridging the avulsed ventral root into the CM. Following studies in the rat model, the VRA regeneration work will transition to a non-human primate model, namely the rhesus macaque. These additional studies in the rhesus macaque are important because:

1) The distances from the injury site to the peripheral targets are far longer in the macaque than in the rat and are thus more comparable to human anatomy. The short distances of the rat anatomy allow the functional reinnervation of the targets such as the lower urinary tract within weeks, while requiring months or years to reach the similar targets in macaques and humans. The slower time course of regeneration in humans and macaques introduces further complications since the distal chronically denervated nerves progressively degenerate over time, losing their ability to direct and support the regenerating axons, slowing the rate and scope of any further functional regeneration [23-27];

2) Immune responses and inflammatory reactions may differ extensively between rodent species as well as between different strains of rats and mice and likely also differ between rats and primates. Inflammatory and immune reactions to nerve injury in humans are likely more similar to those in non-human primates than those in rodents [28-30];

3) Although surgical replantation of avulsed ventral roots has been performed successfully in select patients with brachial plexus avulsion injuries by surgeons in Europe, there have been no documented cases by surgeons in North America using this surgical procedure [31, 32]. The development of a primate

model represents an important intermediate step, which has provided us with a successful and reliable surgical protocol for the replantation of avulsed ventral roots directly into the spinal cord or for using an interpositional bridge such as a peripheral nerve graft or a GDNF-releasing nerve guidance conduit between the spinal cord and avulsed roots.

GDNF is chosen for its key influence upon Schwann cells as a chemoattractant, maturation inducer, as discussed previously in this dissertation. Urocortin is a member of the Corticocortin Releasing Hormone (CRH) family, which is a family of neuropeptides that regulate the pituitary-adrenal axis, modulating the stress response and the corresponding autonomic, endocrine, and behavioral functioning [33]. Urocortin-2 is a 38 amino-acid long peptide with high homology with CRH and is a selective CRHr2 (CRH-receptor 2) ligand. It is expressed in many peripheral tissues in mouse studies, being seen in the pituitary, skin, skeletal muscle, adrenal, stomach, ovary, testis, thymus, brown fat, spleen and lungs [34]. Urocortin-2 regulates fuel utilization in the periphery, modulating glucose homeostasis and metabolic functions through autocrine or paracrine mechanisms [35]. Urocortin-2 also suppresses food uptake in free feeding rats, and can either decrease or increase the firing rate of serotonergic neurons in the dorsal raphe nucleus, depending upon the concentration [36, 37]. We are exploring its use in regeneration in the ventral root due to its role in the autonomic nervous system.

4.2 Methods

4.2.1 Preparation of VRA tubes for rat model

4.2.1.1 July 2010 Preparation

The spinning solution was 14%w/v PCL (65,000 MW, Sigma #181609) in a solvent of 90% DCM (Dichloromethane, Fisher) and 10% DMF (N,N Dimethylformamide, Fisher) by weight. The solution is electrospun with a flowrate of 1mL/hr through a 27-gauge needle from a distance of 6 cm from a grounded, rapidly-rotating mandrel (240 μm-diameter steel hypotubing, 32 gauge, 28 cm in length from SmallParts). A 10 kV positive voltage is applied to the needle tip. A linear stage (Newmark Systems) moved the syringe pump back and forth across the mandrel over a distance of 24 cm for 70 passes at 5 mm/sec. Each tube was spun for 9 minutes to produce a tube with a thickness of about 780 μm. 10 tubes were prepared and subsequently lyophilized for >8 hours to remove residual solvent. The tubes were heat-treated to strengthen the tubes by soaking each tube for 14 minutes at 50°C in DI water in a 2L Erlenmeyer flask. The tubes were then cut into 2.5 cm sections and sterilized by soaking three times for 30minutes in 95% Ethanol, then strung on 75 μm wire (nitinol, SmallParts) to dry in the hood.

4.2.2 Hydrogel composition

The GDNF-free (blank) hydrogel was prepared from 1 mL of PVA stock solution (10%w/v medium molecular weight PVA in DI water (85,000-146,000 MW, Sigma

36,315-4)), 156.25 μL of Collagen Solution (bovine Advanced Biomatrix Nutragen, 6.4mg/mL) and 843.75 μL of DI water to give a final concentration of 5% PVA and 0.05% Collagen (1% of PVA mass). The GDNF-containing group had the similar hydrogel composition of 5% PVA, 0.05% Collagen, and 200 μg/mL GNDF (recombinant Human from Amgen). With an approximate loading of 1.5 μL per 2.5 cm tube, the GDNF was formulated to have 300 ng/tube. In a biosafety hood to maintain sterility, the hydrogel was loaded into a 100 μL Hamilton glass syringe, with a 33-gauge needle. In order to load the tubes while maintaining an open lumen, the tubes were loaded with the 75 μm wire in place. The wire was threaded into the 33 gauge needle, then the needle tip was inserted a few mm into the end of the 2.5 cm tube. The solution was forced through the tube, such that droplets emerged at both ends. The end-droplets were removed, and the tubes (in petri dishes) were placed on ice to prevent evaporation.

4.2.3 Freeze-thaw gelation

Each 2.5 cm tube was placed in an individual screwtop eppendorf tube during freeze-thaw with the guide-wire still inserted. The freeze-thaw cycle consisted of each of the following components: -80°C for 30 minutes, -20°C for 30 minutes, and for 4°C for 30 minutes. 8 cycles were completed in total for 18 tubes with GDNF and 18 tubes without GDNF. Following the last cycle, the tubes were lyophilized overnight, then stored at -20°C until shipment. The tubes were shipped on cold packs to Dr. Havton via FedEx Priority Overnight on 7/12/10.

Additional tubes were prepared in 2014 for replicating the earlier rat study and comparison with Urocortin-2, (synthetic peptide, Abbiotec cat #350414). The electrospinning solution was 8%w/w PCL (MW 80,000, Sigma) in 90/10 DCM/DMF, which was spun through a 27 gauge blunt needle at 0.75 mL/hr. A positive voltage of 7.5kV was applied to the needle tip, and a negative voltage of 3kV was applied to the rapidly-rotating mandrel, which was 240 μm-diameter hypotubing. The tubes were formed by coating the mandrel for 48 passes at 5mm/sec along a travel distance of 210 mm. The tubes were lyophilized, then heat-treated by immersion (while still on mandrel) in a 2L Erlenmeyer flask filled with heated RO water. The tubes were heated for 20 minutes at 50°C, 54°C, and 56°C, then for a final 10 minutes at 58°C. The tubes were cut into 2.5 cm-long sections, and 75 μm-diameter nitinol wires were threaded into each to maintain an open lumen. The tubes were sterilized via ethanol soaking for 30 minutes in 70% ethanol, then 2 hours in 100% ethanol, followed by overnight drying in the biosafety cabinet. The PVA-collagen hydrogel was prepared identically as described in the 2010 experiment, to produce tubes with blank hydrogels, GDNF hydrogels (300 ng/tube Urocortin-2. 15 tubes with blank hydrogels and 15 tubes with 300 ng/tube of GDNF were shipped overnight to Dr. Havton on 3/10/14. 15 tubes with 300 ng/tube of Urocortin-2 were shipped overnight to Dr. Havton on 7/22/14.

4.2.4 Preparation of conduits for Rhesus Macaque study

8%w/w PCL (molecular weight of 80k, Sigma) in a solvent of 90%w/w DCM and 10%w/w DMF. The solution is electrospun with a flowrate of 0.75 mL/hr through a 27

gauge needle from a distance of 6 cm from a rapidly-rotating steel mandrel. A 7.5kV positive voltage is applied to the needle tip, while a 3kV negative voltage is applied to the mandrel. A linear stage (Newmark Systems) moved the syringe pump back and forth across the steel mandrel over a distance of 22 cm at 5 mm/sec. To produce tubes with different inner diameters, the diameter of the mandrel was varied along with the number of rounds. The 1.0 mm-diameter tubes were spun onto a 1.0 mm-diameter mandrel for 48 passes. The 1.25 mm-diameter tubes were spun on a 1.25 mm-diameter mandrel for 60 passes. The 1.5 mm-diameter tubes were spun on a 1.5 mm-diameter mandrel for 70 passes. The 1.75 mm-diameter tubes were spun on a 1.75 mm-diameter mandrel for 70 passes. The tubes were then lyophilized for 48 hours to remove residual solvent. While still on the mandrel, the outer tubes were subsequently heat-treated to increase strength by soaking in hot water, 20 minutes at each of 53°C and 54°C. The tubes were then cut to 33 mm segments.

4.2.5 Inner layer spinning

To produce the inner layer of aligned fibers to guide the regenerating axons, we produced a double-layer fiber mesh, with a lower-layer of random fibers to provide mechanical support to the top layer of aligned fibers. The bottom, random layer was produced by spinning 8%w/w PCL (80k) in 90/10 DCM/DMF at 0.9 mL/hr through a 27 gauge needle 8 cm away from the grounded, target wheel. An 8kV positive voltage was applied to the needle tip, and the syringe pump was rastered over a distance of 125 mm for 2 passes at 0.1 mm/sec. The wheel rotated at 64 rpm to ensure even coverage. The

large target wheel had 6 sets of labtape pre-placed upon it, to aid in the subsequent removal of the fiber layers. The tape was laid out to produce 6 sets of double-fiber rectangles, 5 cm in height and 12.5 cm in width. After deposition of the random fiber layer, the aligned layer was spun directly on top. The spinning solution was 11%w/w PCL (80k) in 90/10 DCM/DMF, spun at 0.3 mL/hr through a blunt 32 gauge needle with 2 cm separation from the wheel surface. The wheel rotated at 1000 rpm, while the positive voltage of 5kV was applied to the needle tip. The fibers were spun for 7 passes over a distance of 115 mm at 0.1 mm/sec.

The fiber sheets were then removed with the help of the tape support. Extra caution was taken to ensure that the original geometry of the fiber sheets was kept intact, and stretching or bunching of the fibers was avoided. Each fiber sheet was placed on a frame (upside-down pipette tip box), maintaining fiber alignment and integrity, with aligned fibers facing up. A mandrel was placed along the long-axis of the aligned fibers, and a drop of PVA solution was added to the top and bottom edges of the fiber sheet to bond the fiber sheet edges to the mandrel. The mandrel then was rolled along the fiber sheet as it was cut free from the frame, transferring the fiber mesh onto the mandrel. After 2 rotations around the mandrel, the fiber-coated mandrel was cut free from the fiber sheet and inserted into the middle of the respective outer tube previously prepared. The mandrel used for each fiber sheet was slightly smaller than the inner diameter of the outer tube to allow space for the hydrogel and ease the eventual mandrel removal. The 1.5 mm outer tubes used a 1.25 mm mandrel for fiber-sheet rolling, the 1.25 mm tube used a 1.0 mm mandrel, the 1.0 mm tube used a 0.75 mm mandrel, and the 1.75 mm-tube used a 1.5

mm mandrel. The fiber sheet extended past the outer tube on both ends. The conduits (outer tube with inner mandrel with aligned fiber sheet) were sterilized with ethanol soaks, with three soaks for 30 minutes each, submerged in 70% ethanol, 100% ethanol, and 100% ethanol again. The conduits were allowed to dry overnight in the biosafety cabinet to remove residual ethanol.

The blank group used the same hydrogel formulation as the previous rat studies, with 5% PVA and 1 mg/mL Collagen. 10 mL of blank hydrogel solution was prepared with 5 mL of the 10% PVA stock, 1.695 mL of Nutragen Collagen, and 3.305 mL of sterile water. The blank hydrogels were loaded first, and used to determine the volume of hydrogel deposited into each conduit size, by weighing before and after hydrogel addition (assuming 1mg = 1μL). This allowed determination of the GDNF needed in each formulation to obtain the desired 300 ng/33 mm tube loading. The 1.5 mm tubes averaged a loading of 17.87 μL of hydrogel and needed 16.79 μg/mL of GDNF. The 1.25 mm tubes averaged a loading of 16.72 μL of hydrogel and needed 17.94 μg/mL of GDNF. The 1.0 mm tubes averaged a loading of 10.72 μL of hydrogel and needed 27.98 μg/mL of GDNF. The GDNF-containing conduits were prepared second, using the previously described concentrations of GDNF in addition to the identical PVA and collagen concentrations. The hydrogels were added to each conduit by injecting it into the region in between the outer tube wall and the fiber-sheet-wrapped mandrel. After hydrogel addition, the conduits, with the mandrels still in place, underwent freeze-thaw gelation similar to that used for the rat studies, with each cycle consisting of -80°C for 30 minutes, -20°C for 30 minutes, and for 4°C for 60 minutes for a total of 6 cycles. After gelation,

the tubes were removed from the mandrels with the help of sterile DI water and any extra nanofibers emerging from the outer wall were cut flush. The conduits were then snap frozen before lyophilization and preparation for shipment.

The final VRA nerve guides were 33 mm in length, with an inner diameter of 1 mm, 1.25 mm, or 1.5 mm to accommodate different nerve root diameters. The conduits were designed to be cut to the desired length by the surgeon (approximately 15 mm), with each supplied tube being capable of being used for two nerve roots each. 10 of each size, plus 4 of a larger 1.75 mm-diameter were prepared with blank hydrogels and shipped on 5/15/12. 11 each of the 1 mm, 1.25 mm, and 1.5 mm nerve conduits, each containing 300ng/tube GDNF were shipped to Dr. Havton on 6/12/12.

4.2.6 Rat study design

Study design: In adult female rats, a unilateral ventral root avulsion (VRA) injury was performed. Under general gas anesthesia (isoflurane), following a lumbar laminectomy and opening of the dura mater, the injury included avulsion of the L6 and S1 ventral roots from the surface of spinal cord. These ventral roots normally carry efferent axons from motoneurons innervating the pelvic floor and axons from preganglionic parasympathetic neurons. The primary locations for the cell bodies of these somatic motor and autonomic neurons are the L6 and S1 spinal cord segment. A biodegradable nerve guidance conduit (NGC) was next surgically implanted into the rat spinal cord. Each NGC either released GDNF or was empty (control). A 1-2 mm

longitudinal incision was made into the lateral funiculus at the L6/S1 level of the spinal cord, and the NGC was surgically implanted into the incision. A suture was placed at the distal end of the NGC to prevent any entry of axons from the periphery. Next, the muscle and skin were closed in layers and the subjects allowed to recover.

4.2.7 Rhesus macaque study design

A total of five experimental groups were included in the studies: 1) Unilateral L6-S3 ventral root avulsion (VRA) injury and no root repair (n=5 subjects); 2) unilateral L6-S3 ventral root avulsion (VRA) injury followed by direct implantation of avulsed ventral roots into the spinal cord (n=5 subjects); 3) unilateral L6-S3 VRA injury followed by root repair using a GDNF-releasing nerve guidance conduit to bridge between the spinal cord and each avulsed root (n=4 subjects); 4) unilateral L6-S3 VRA injury followed by acute root repair using a nerve guidance tube without release of neurotrophic factor to bridge between the spinal cord and each avulsed root (n=5 subjects); 5) unilateral VRA injury followed by acute root repair using an intercostal nerve graft to bridge between the spinal cord and each avulsed root (n=5 subjects). The nerve guidance tubes and peripheral nerve graft were all approximately 1.5 cm in length to facilitate direct comparisons between the groups. All animals were studied for 2 months (n=1) or 18 months (n=3).

The adult rhesus macaques underwent a unilateral L6-S2 VRA injury followed by root repair using nerve guidance conduits or intercostal nerve grafts as a tissue bridge between the spinal cord and avulsed ventral roots. The four-level VRA injury resulted in partial or complete denervation of ipsilateral hind limb muscles and denervation of the

ipsilateral side of external sphincter muscles. The affected lumbosacral spinal cord segments also include motoneurons of Onuf's nucleus, which innervate the external anal and urethral sphincter muscles and are typically located within the L7 and S1 segments of the spine [38, 39]. Throughout the course of the studies, we performed functional and imaging assessments of the effect of root replantation. For this purpose, assessments of hind- limb function and locomotion were also performed pre-operatively and monthly during the full post-operative course of the studies. EMG recordings of the external anal sphincter were performed pre-operatively, within the first week post-operatively and subsequently every three months for the duration of the study. MRI studies of the lumbar spine were performed pre-operatively and post-operatively at 6 weeks and 18 months after the VRA injury and replantation. At the end of the study period, fluorogold was injected into the midline-positioned external anal sphincter muscle and the B subunit of the cholera toxin (CT-B) was injected into the medial gastrocnemius muscle bilaterally to retrogradely label the motoneurons that have successfully reinnervated the peripheral targets. Five days after tracer injections, all animals underwent intravascular perfusion with a 4% paraformaldehyde solution to preserve spinal cord and nerve root tissues for morphological analysis.

Throughout the study period, a combination of behavioral, locomotor, MR imaging, and EMG studies were performed at multiple time points. At the end of the experiments, anatomical studies were also performed. The different studies and outcome measures were performed as below: For behavioral assessments of hind limb and treadmill locomotor function, established protocols of the California Primate Spinal Cord

Injury Consortium at CNPRC/UC Davis were used [40, 41]. Treadmill locomotor studies provided spatial and temporal features of the gait pattern. For this purpose, we used detailed video recordings and measured 1) cycle duration, 2) stride length, 3) stance duration, and 4) swing duration for each animal at different treadmill speeds. EMG studies of the external anal sphincter muscle were performed pre-operatively, within the first week post- operatively, and subsequently every three months for the duration of the study to provide detailed information on sacral reflex function, as EMG activity was induced by rectal glass probes for brief anal distention to induce an EMG burst using an established protocol for data analysis of 1) burst duration, 2) firing frequency during burst, and 3) area under the curve measurements of integrated signals [42]. MR imaging studies were performed pre-operatively and at 6 weeks and 18 months post-operatively. Signal intensity and cross sectional area measurements of ventral roots were performed using both T1 and T2, with and without contrast administration. MRI signal intensity and area measurements for the right and left L5 -S1 ventral roots were compared and expressed as a ratio of the means. Postoperative MRI studies also confirmed the segmental levels that were lesioned by ventral root avulsion injury.

Anatomical studies took place at the end of the study period and included stereological counts of ChAT immunoreactive neurons in the L7 and S1 segments to assess for neuro-degeneration and protection. Stereological counts of L7 and S1 segment neurons, retrogradely labeled with FG and CT-B from the external anal sphincter and medial gastrocnemius muscles, respectively, determined the degree of reinnervation of peripheral target muscles. Stereological counts of myelinated fibers in the avulsed

replanted and intact roots determined the extent of Wallerian degeneration and axonal regeneration. Electron microscopic studies of nerve roots determined the G ratio of myelinated fibers in replanted and intact roots to assess for the degree of myelination after injury and repair. Ultrastructural studies also determined the presence of and quantity of non-myelinated fibers, which are not readily visible on toluidine blue light microscopic preparations.

4.2.8 Spine surgery

Under general isoflurane anesthesia, the subject was in the prone position and the skin over the lumbar spine was prepped and draped. A skin incision was made and the spinous processes of L1-L5 were exposed. The left-sided facet joints of L1-2 to L4-5 were exposed. A high-speed drill was used to thin the vertebral levels of L1-5 on the left side. Next, the exposed dura mater was opened and held with a 4-0 vicryl and the spinal cord was slightly rotated to expose the ventral aspect. The conus medullaris was turned and the L6, L7, S1, and S2 ventral roots were identified using anatomical landmarks and normal caliber differences between the individual roots. The roots were individually avulsed from the surface of the spinal cord. A 2-3 mm biopsy of the tip of each avulsed root was preserved in aldehyde fixative for later morphological studies. For root replantation purposes, a small stab incision was made using a #11 scalpel blade at each avulsed segmental level and the avulsed L6-S2 ventral roots were individually inserted into their original segmental levels. The replanted roots were also attached to the leptomeninges using a 10-0 prolene. The dura was closed with a 7-0 prolene. Next, the

spinal incision was closed with interrupted 2-0 vicryl followed by running 3-0 vicryl. The skin was closed with 4-0 vicryl and the subject was allowed to recover from anesthesia. Note that in a subset of animals, the L6-S2 VRA injury was performed without the root replantations, but all other procedures were identical in this series.

In a subset of animals, an intercostal nerve graft was used for bridging the gap between the spinal cord and the avulsed ventral roots. For this purpose, the left T11 rib was identified and exposed. The T11 intercostal nerve was next identified and a 4 cm segment of the nerve was isolated. The intercostal nerve was divided into 4 equal-length segments, each approximately 1 cm long. The nerve grafts were anastomosed to the avulsed ends of the ventral roots using a 10-0 prolene. The opposite end of the nerve grafts were implanted into small incisions made into the lateral side of the spinal cord at each avulsed segment and the graft secured to the leptomeninges using a 10-0 prolene. The dura and surgical incision were next closed in a fashion identical to the procedure used after direct root replantations.

In a subset of animals, GDNF-releasing or non-releasing nerve guidance tubes were used to bridge a gap between the avulsed lumbosacral ventral roots and the spinal cord. The nerve guidance tubes were anastomosed to the avulsed ends of the L6 and L7 ventral roots using a 10-0 prolene suture. The opposite end of the nerve grafts were implanted into small longitudinal incisions made into the lateral side of the spinal cord at each avulsed segment and each tube was placed into the lateral funiculus of the L6 or L7 segments. secured to the leptomeninges using a 10-0 prolene suture. The dura and

surgical incision were next closed in a fashion identical to the procedure used after direct root replantations.

4.3 Results

4.3.1 Rat VRA conduit production

The nanofiber mesh was essentially random in orientation due to the slow rotation of the mandrel relative to the electrospinning jet whip speed. The fibers were approximately 675 nm in diameter with interfiber pores of ~1 to 5 μm. The completed conduits can be observed in Fig. 4.3. During heat-treatment, the outer diameter of the tubes decreased from about 780-850 μm to less than 750 μm in diameter. The fibrous nature of the nanofibers was maintained, with some neighboring fibers melting together, however. During gelation, the PVA-collagen solution changed from a clear, but slightly cloudy liquid to an opaque white solid. After gelation and lyophilization, the guide wires were very difficult to remove, unlike the prototypes, which received only a few freeze-thaw cycles and no lyophilization. The wires could be removed, but only after soaking in PBS and with great force exerted via forceps. Future tubes will be produced with the wires removed after gelation but before lyophilization. For the 2014 rat VRA tubes, the tubes were processed identically through the gelation stage. Prior to lyophilization, the tubes were dipped into 70% ethanol, which allowed the guide wire to be removed. The tubes were then lyophilized as before. 16 GDNF-loaded tubes and 16 blank-hydrogel tubes were shipped to Dr. Havton.

4.3.2 Macaque VRA NGC production

This design shares elements from both the rat VRA NGCs but also the peripheral nerve NGCs from the previous chapter. Like the rat VRA NGCs, the larger rhesus macaque tubes contain an electrospun PCL nanofiber outer wall and PVA-collagen hydrogel for releasing GDNF (Fig. 4.8). Unlike the rat VRA NGCs, however, the macaque VRA NGCs contained an aligned nanofiber component lining the conduit lumen. The aligned fiber layer had an average fiber diameter of 576nm ±182nm with an angular standard deviation of 6° off-axis, showing excellent alignment (Fig. 4.9). The GDNF-releasing PVA layer was injected between the outer wall and the aligned fibers, and can be seen in the SEM image. The PVA layer likely expands considerably into its hydrated state in use. The PVA layer can be seen throughout the circumference of the lumen, providing even delivery of the GDNF. In sections of the NGC it can be seen within the aligned layer itself, which may reduce the guidance cue slightly. The SEM images also verify that the outer wall retained its fibrous nature after heat-treatment.

4.3.3 Preliminary rat VRA results

The pilot rat studies show that the surgeons can manipulate the NGCs and implant them into the spine, a nontrivial concern for a tube with features only hundreds of microns in size (Fig 4.4). Once implanted into the rat spine, the NGCs were able to attract and guide regenerating axons into the conduit (Fig 4.5). The GDNF-releasing NGCs contained considerably higher numbers of myelinated axons (Fig 4.5, 4.6). The relative lack of

myelinated axons in the GDNF-free group is unsurprising, as that group lacked either chemoattractants or topographical guidance to attract and guide the cells, particularly since the tubes could not benefit from trophic cues from the distal root stump. The tubes were ligated to ensure that no periphery axons were able to enter the distal stump and confuse the analysis. Thus, it is notable that such robust myelination is possible in these conduits. The myelinating Schwann cells were not pre-seeded into the NGCs nor were they natively present in the lateral funiculus. Schwann cells, however, have been observed to migrate into the lateral funiculus immediately after trauma, where they may be able to sense and migrate towards the GDNF-releasing NGC [43]. The Schwann cell response, and hence the myelinated axon count, would be potentially greater if the root is reattached to the distal end of the NGC to provide a simpler path into the conduit.

4.3.4 Preliminary Rhesus Macaque VRA results

Dr. Havton et al have shown that they have established reliable procedures for inducing VRA injury in the rat or macaque and repairing those injuries with intercostal nerve grafts (Fig. 4.1, 4.2). The initial results from one macaque at 2 months showed promise, as the NGC had excellent biocompatibility and did not induce infection or complications (Fig. 4.10). The connection between the avulsed roots and the NGC remained intact (Fig. 4.11). At 2 months, axons can be seen in great numbers growing into the NGC, though at this stage no myelinated axons were detected (Fig. 4.12). The initial results are also positive from the first animals so far analyzed after the full 18 month study (Fig. 4.13). The structural integrity of the NGC and its connections were maintained over this

timespan. PCL is a slowly degrading polymer, but it may be starting to degrade at this timepoint. Several hundred myelinated axons can be seen in the NGC lumen as well as blood vessels and connective tissue. Further analysis (both histological and functional) of the treatment groups and control groups will be forthcoming shortly.

4.4 Discussion

This study shows the clear potential of nanofiber-based scaffolds for improving regeneration after ventral root avulsion injuries. The biocompatibility and efficacy were seen in both rat and non-human primate models, indicating that this strategy is likely to be successfully translated to clinical use in humans. One recent study employed a PLGA scaffold with four channels to reconnect with 4 avulsed roots [44]. The use of the scaffold resulted in a higher frequency of roots with at least one bridged axon (73%) versus either direct implantation into the ventral cord (30%) or muscle fascia used as a negative control (18%). However, very few axons were able to regenerate across the scaffold per root, in insufficient numbers to elicit functional recovery. Our superior results may be attributed to several factors, including a better scaffold material stiffness match (a block of PLGA is much stiffer than electrospun PCL and the native nerve and CM), better topographical guidance by means of the aligned nanofibers in the macaque study or nanofiber topography and narrow lumen in the rat study, a semi-porous scaffold outer wall as compared to the nonporous PLGA, and especially the inclusion of growth factors such as GDNF. Growth factors have been shown to be effective in guiding and supporting

regenerating axons into the avulsed ventral root, such as seen in one study in which a collagen gel with ASCs transiently transfected to overexpress GDNF and BDNF [45].

The most recent VRA-related studies in the literature are heavily focused upon improving the motoneuron survival following avulsion. While the NGCs described here elute out GDNF, which can be neuroprotective, our main innovation is providing a permissive substrate to encourage the outgrowth of the surviving motoneurons into the nerve root. Potentiating reconnection to the ventral root may itself benefit motoneuron survival—Su et al showed that direct reimplantation of the severed roots improved both the survival and regeneration of motoneurons as compared to peripheral nerve grafts or no reimplantation [46]. Our conduit design should thus work synergistically with the neuroprotective agents to keep the neurons alive and successfully redirected to their distal targets. Subcutaneous injection of Erythropoietin (EPO) has been shown to improve motoneuron survival, as have intraperitoneal injection of lithium chloride [47, 48]. Li et al showed the counterintuitive result that preconditioning the ventral root through a crush injury a week prior to avulsion results in significantly higher motoneuronal survival after an avulsion injury, possibly through the neuroprotective effect of the heat shock protein 27 that was released during the rush injury [49]. Chew et al explored the use of Minocycline and Riluzole to improve motoneuronal survival. While the drugs (via intraperitoneal injection) did ease the tactile and thermal hypersensitivity that causes great pain in VRA patients by reducing astrocyte activation, the drugs did not have any neuroprotective effect [50]. In addition to biochemical means, researchers are also

exploring the use of mesenchymal stem cells, which have been shown to improve motoneuron survival, axonal regeneration, and muscle innervation [51, 52].

4.5 Conclusion

These studies indicate that synthetic scaffolds can recruit and guide axons from the spine after ventral root avulsion, a key step in promoting motoneuronal survival and necessary for any form of functional recovery. GDNF has proven to be a powerful growth factor to potentiate this regeneration, though this study does not indicate whether GDNF's primary mode of action is affecting the axons directly or rather indirectly through its effects on Schwann cells. These results in the non-human primate indicate that synthetic conduits are likely to be able to guide axons in humans, and with further optimization they may be able to provide much desired functional regeneration to an underserved patient population.

4.6 Figures

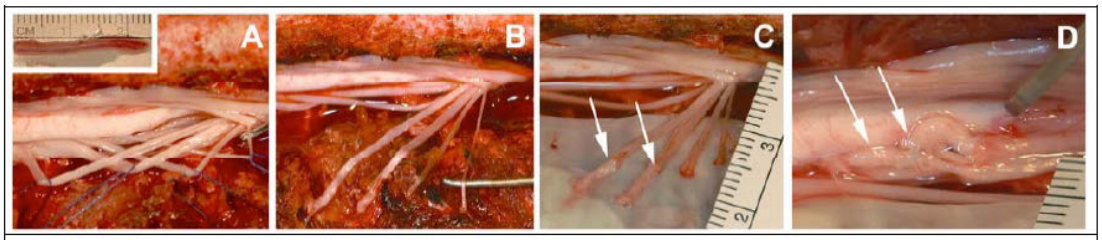

Figure 4-1: Nerve grafts for lumbosacral VRA repair in Rhesus Macaque.

Intra-operative images of VRA injury and replantation using an intercostal nerve graft to bridge between the avulsed roots an the spinal cord. A: Four consecutive ventral roots of the L6, L7, S1, and S2 segments are identified A (inset): Harvested T11 intercostal nerve graft. B: The L6, L7, S1, and S2 ventral roots (left-to-right) are avulsed from the surface of the spinal cord. C: An approximately 8 mm long intercostal graft segment was attached to the avulsed end of the L6 and L7 ventral roots using microsurgical techniques and 10-0 Prolene sutures. D: The free end of the intercostal nerve graft segments are implanted into the lateral funiculus of the spinal cord and the implanted graft is attached to the leptomeninges using a 10-0 Prolene suture.

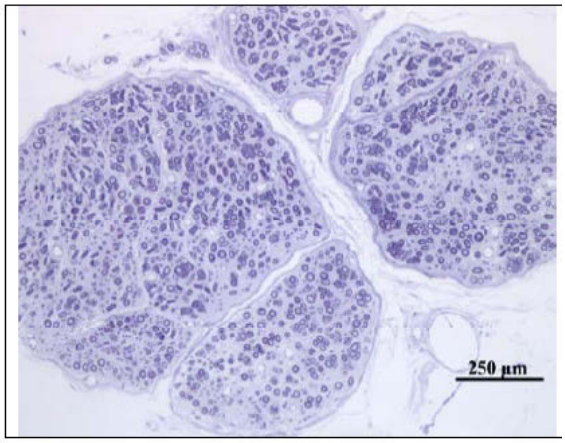

Figure 4-2: Histology image of nerve graft for VRA repair in Rhesus Macaque.

Light microscopic studies of plastic embedded and toluidine blue stained intercostal nerve graft, which was used as a bridge between the conus medullaris and the avulsed L7 ventral root after a unilateral L6-S2 ventral avulsion injury in a rhesus macaque. These studies were performed at 18 months after the root repair. Note the large number of regenerating axons in nerve graft and fibers demonstrating myelination. Stereological studies demonstrate a total of 2,606 small and large myelinated fibers in graft. The studies demonstrates the feasibility of using a mixed nerve bridging graft to overcome a tissue gap caused by a proximal ventral root injury for long-term studies in the non-human primate.

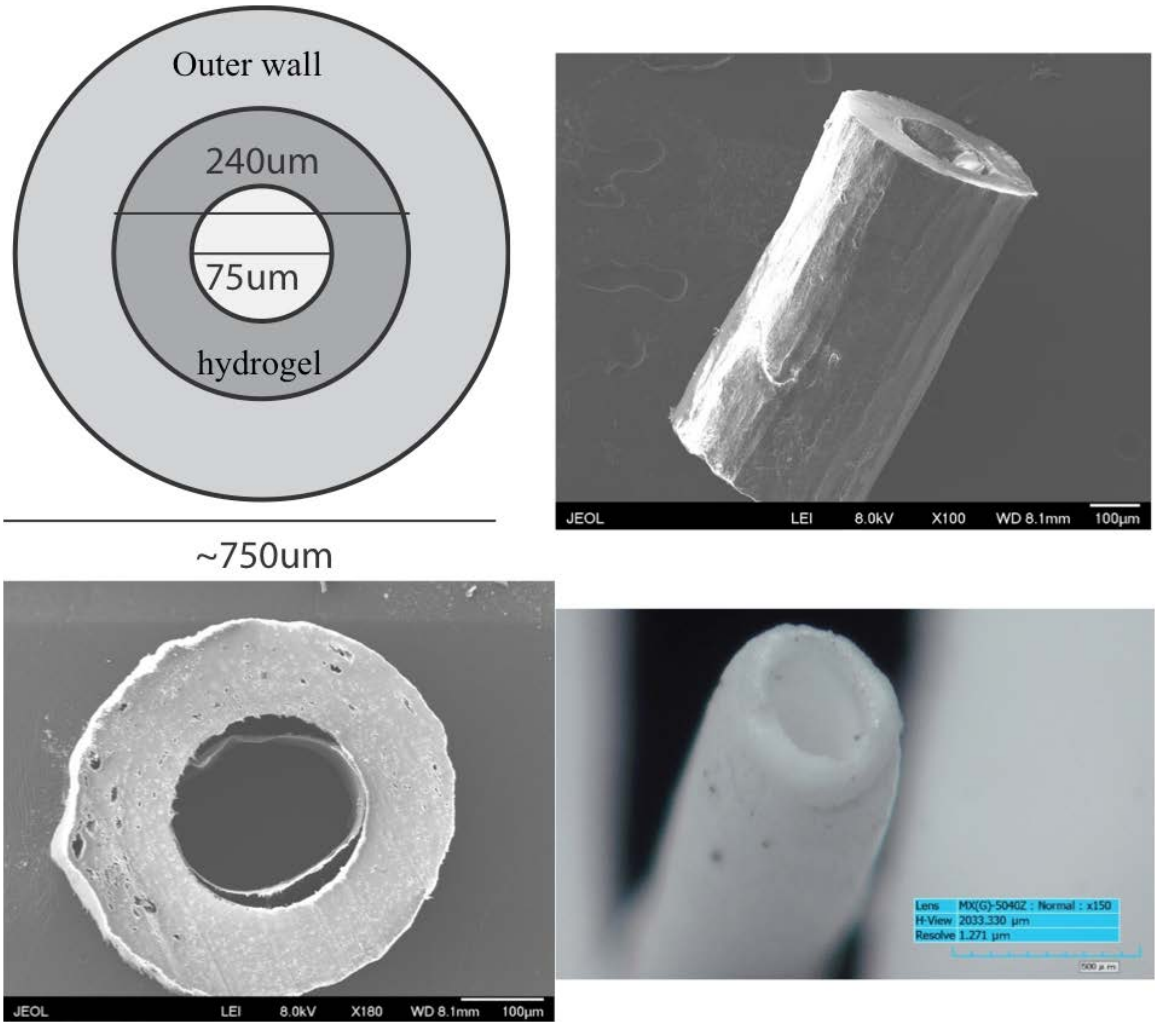

Figure 4-3: Design and Physical Appearance of NGC for Rat VRA Repair

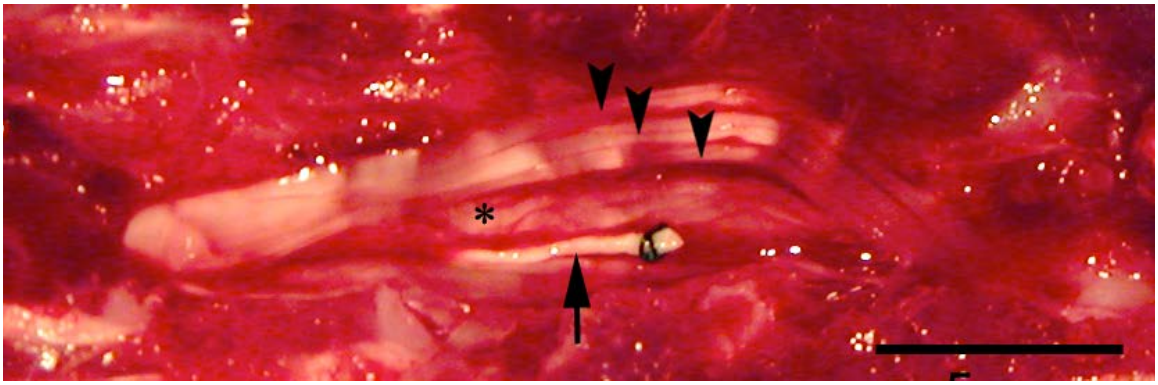

Figure 4-4: VRA repair with NGC in rat model.

The arrow indicates the NGC – note suture at the distal end of NGC, ligated to prevent entry of axons from the periphery; The arrow heads indicate dorsal lumbosacral roots; The star sign indicates the lateral surface of the spinal cord; The scale bar = 2 cm.

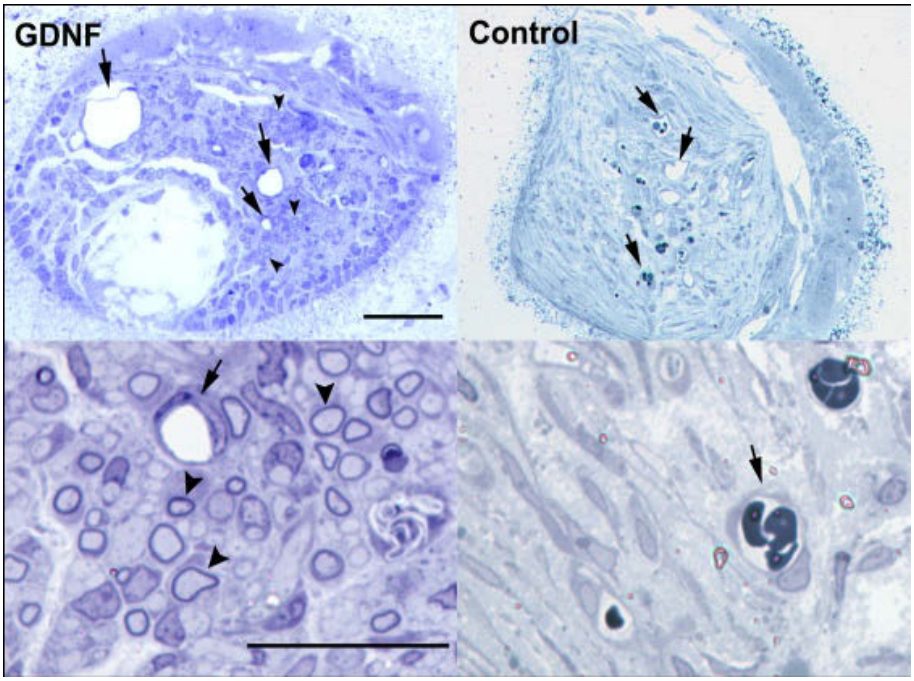

Figure 4-5: GDNF NGCs support axonal regeneration in rats after VRA injury.

GDNF-releasing NGCs were surgically implanted into the rat spinal cord of after a lumbosacral VRA injury. Many regenerating axon were present in the GDNF-releasing NGCs (n=3) compared to control NGCs (n=5) at 4 weeks after surgery Electron microscopy (see below) shows myelinated and non-myelinated axons in NGCs with GDNF. Note about a ten-fold difference in the number of regenerating myelinated axons between GDNF and control groups. Scale bar = 50 μm for upper and 25 μm for lower micrographs.

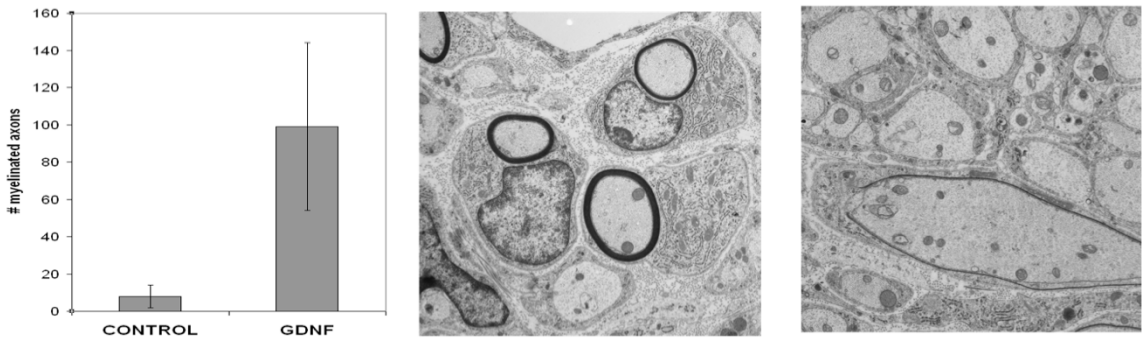

Figure 4-6: Enhanced axonal regeneration in rat VRA model in GDNF-NGCs.

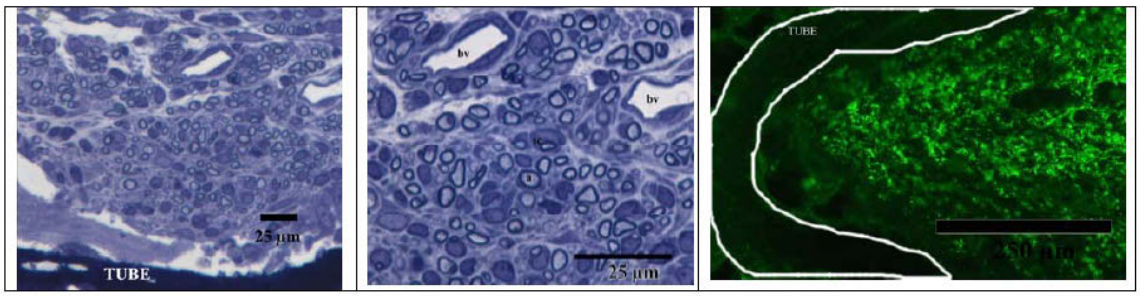

Figure 4-7: GDNF NGC tube at 4 weeks after rat VRA repair.

Toluidine blue stained section at 4 weeks after surgical implantation into the rat lumbar spinal cord after a L5-S2 ventral root avulsion injury (left). Note many regenerating axons in close association with inner wall of tube. High magnification of the same nerve guidance tube shows presence of myelinated axons, Schwann cells, and blood vessels (middle). Immunohistochemistry for neurofilament marker, RT-97, shows presence of axons in close association with inner wall of the nerve guidance conduit in its implanted location in the lumbar spinal cord (right).

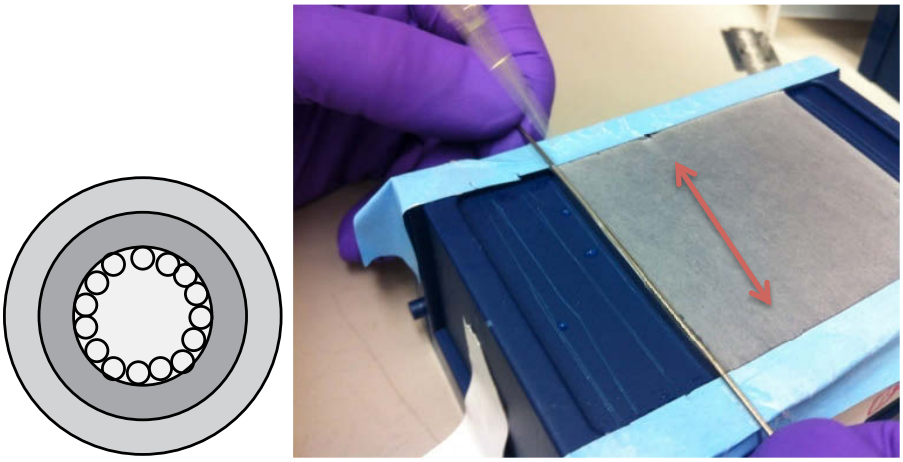

Figure 4-8: Design of GDNF-NGCs for VRA Repair in Rhesus Macaque Model.

Left: This design shares elements from both the rat VRA NGCs but also the peripheral nerve NGCs from the previous chapter. Like the rat VRA NGCs, the larger rhesus macaque tubes contain an electrospun PCL nanofiber outer wall and PVA-collagen hydrogel for releasing GDNF. Unlike the rat VRA NGCs, however, the macaque VRA NGCs contain an aligned nanofiber component lining the conduit lumen. Right: Image of the process of forming the inner aligned fiber layer, as the mandrel is being wrapped with the dual layer fibers (the top layer seen here is aligned in the orientation indicated in the arrow.

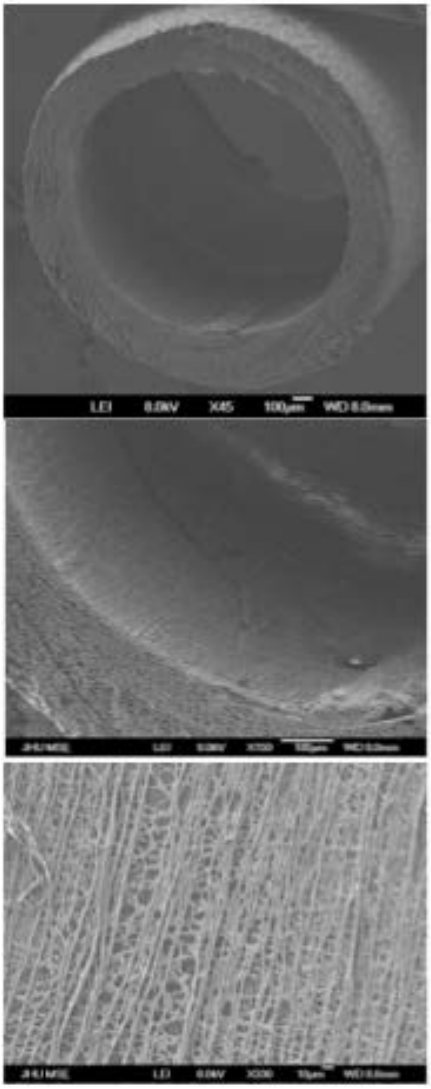

Figure 4-9: Physical Appearance of NGC for Primate VRA Repair Model.

Top: SEM transverse cross-section of GDNF-containing NGC. Middle: Higher magnification image of NGC wall. Note fibrous, semi-permeable nature of outer wall and the location of the hydrogel layer between outer wall and inner wall shrunken from hydrated state. Bottom: Dual-layer nanofiber sheet from NGC lumen, with aligned nanofibers on top of random nanofibers. The webbed structures between random-nanofibers are composed of the GDNF-releasing dehydrated hydrogel component.

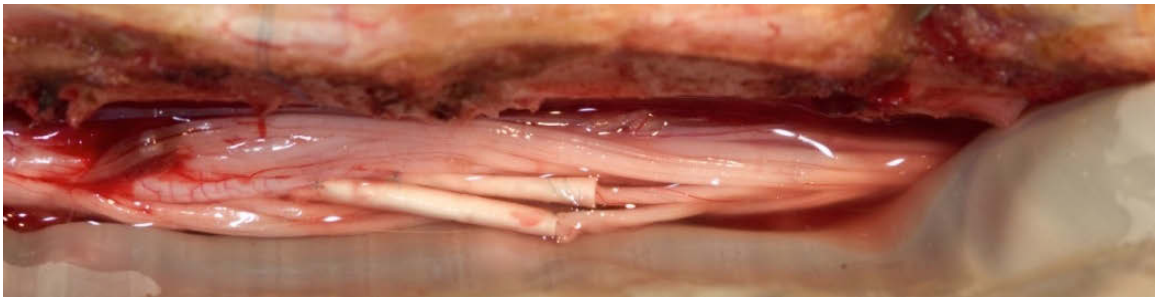

Figure 4-10: Translation of the Use of GDNF Nerve Guidance Conduits to Rhesus Macaques For Long-Term Studies of Axonal Regeneration.

The repaired ventral roots in adult rhesus macaques, a lumbar laminectomy and dura opening was followed by a unilateral avulsion injury of the L6-S3 ventral roots. Next, GDNF-releasing NGCs were surgically placed as a bridge between the spinal cord and the avulsed L6 and the L7 ventral roots. The proximal end of each NGCs was placed into the lateral funiculus of the L6 or L7 segments. The avulsed tip of L6 and L7 ventral roots was placed into the lumen of the NGC and secured with a fine suture. Next, the dura was closed and the paraspinous muscles, fascia, and skin closed in layers. All subjects were allowed to recover and studied for 2 months (n=1) or 18 months (n=3). The procedures were tolerated well and the NGCs were identified and in original surgical position at the end of the study periods (see next slide).

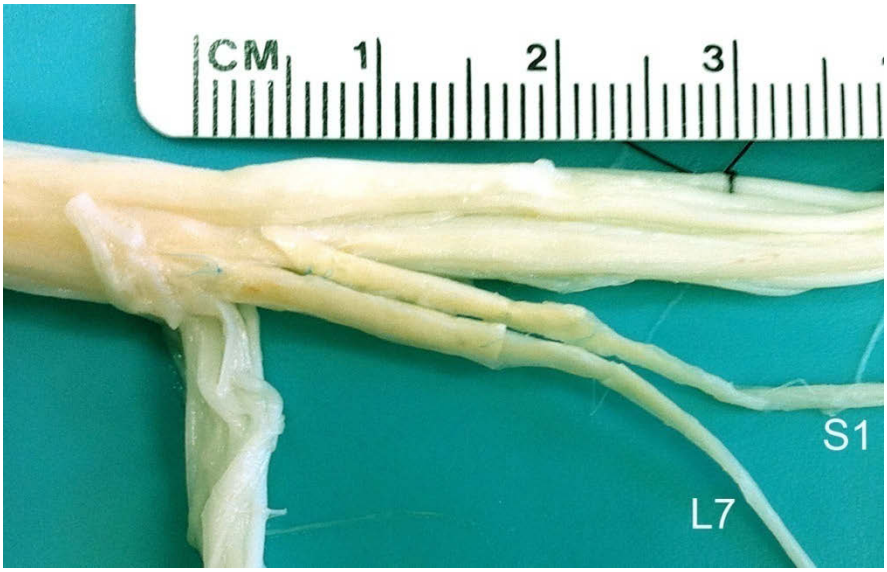

Figure 4-11: Physical appearance of GDNF-NGC after 2 months.

Note intact placement of NGCs and avulsed VRs in conduits after 2 months in the rhesus macaque.

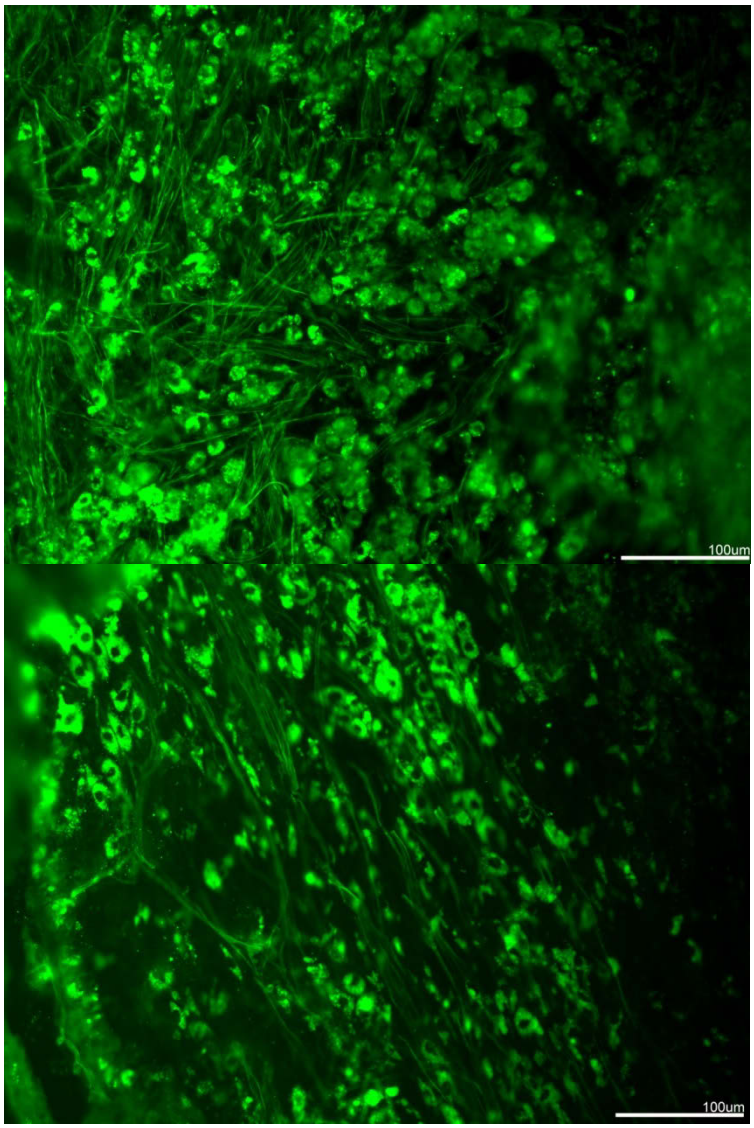

Figure 4-12: Axonal regeneration within GDNF-NGC at two months.

At two months after initial VRA and repair surgery using GDNF-releasing NGCs, spinal cord and nerve root tissues were studied morphologically with Immunohistochemistry. Beta-III-tubulin (in green) shows regenerating axons in NGCs near CNS/PNS interphase. No myelinated axons were detected inside the NGCs, however.

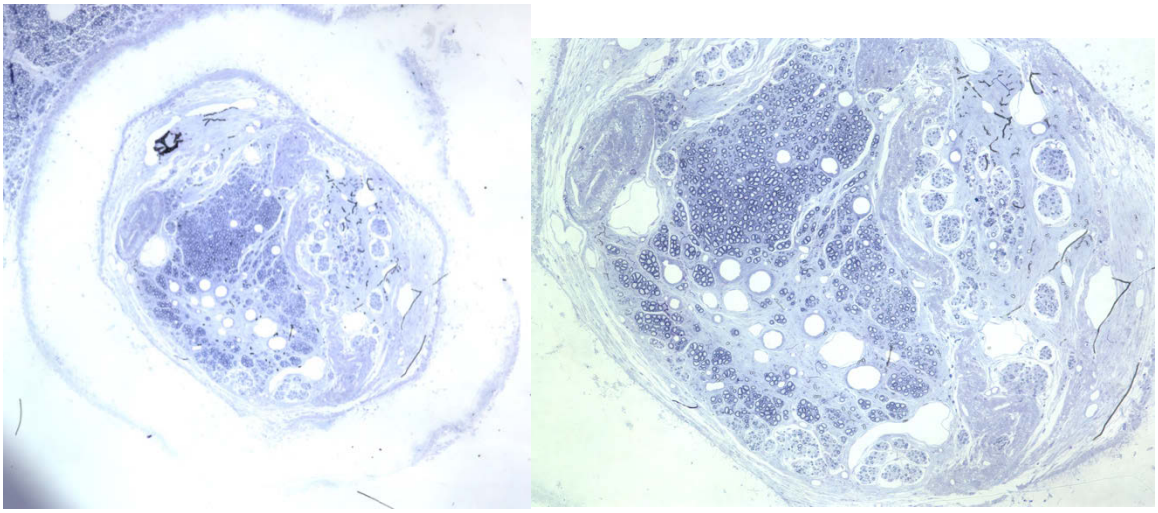

Figure 4-13: Successful axonal regeneration within GDNF NGCs at 18 months.

Light micrographs of NGCs at 18 months after a unilateral L6-S3 VRA injury and surgical placement of GDNF-releasing NGCs as a bridging graft between the spinal cord and the avulsed L6 and L7 ventral roots in an adult female rhesus macaque. Note the well-preserved integrity of NGC and presence of several hundred myelinated axons. Also note the presence of several Blood vessels and connective tissues in NGC. Two additional rhesus macaques that underwent the same procedure show similar extensive signs of axonal regeneration in side of GDNF-releasing NGCs at 18 months post-operatively.

4.7 References

1. Carlstedt, T. and L. Havton, *The longitudinal spinal cord injury: lessons from intraspinal plexus, cauda equina and medullary conus lesions.*, in *Handb Clin Neurol*. 2012. p. 337-354.
2. Maynard, F.M., et al., *International standards for neurological and functional classification of spinal cord injury.* Spinal cord, 1997. **35**(5): p. 266-274.
3. Dobkin, B.H. and L.A. Havton, *Basic Advances and New Avenues in Therapy of Spinal Cord Injury*, in *Annu. Rev. Med.* 2004. p. 255-282.
4. Hoang, T.X. and L.A. Havton, *Novel repair strategies to restore bladder function following cauda equina/conus medullaris injuries*, in *Progress in brain research*. 2006. p. 195-204.
5. Moschilla, G., S. Song, and T. Chakera, *Post-traumatic lumbar nerve root avulsion.*, in *Australas Radiol*. 2001. p. 281-284.
6. Hans, F.J., M.H. Reinges, and T. Krings, *Lumbar nerve root avulsion following trauma: balanced fast field-echo MRI*, in *Neuroradiology*. 2004. p. 144-147.
7. Monga, P., et al., *Traumatic Lumbar Nerve Root Avulsion: Evaluation Using Electrodiagnostic Studies and Magnetic Resonance Myelography*, in *J Trauma*. 2004. p. 182-184.
8. Pavlakis, A.J., et al., *Neurourologic findings in conus medullaris and cauda equina injury.*, in *Arch. Neurol.* 1983. p. 570-573.
9. Beric, A. and J.K. Light, *Function of the conus medullaris and cauda equina in the early period following spinal cord injury and the relationship to recovery of detrusor function.*, in *The Journal of urology*. 1992. p. 1845-1848.
10. Anderson, K.D., *Targeting Recovery: Priorities of the Spinal Cord-Injured Population*, in *J Neurotrauma*. 2004. p. 1371-1383.
11. Hoang, T.X., et al., *Autonomic and motor neuron death is progressive and parallel in a lumbosacral ventral root avulsion model of cauda equina injury*, in *J. Comp. Neurol.* 2003. p. 477-486.
12. Ohlsson, M. and L.A. Havton, *Complement activation after lumbosacral ventral root avulsion injury*, in *Neurosci Lett*. 2006. p. 179-183.
13. Hoang, T.X., *Functional Reinnervation of the Rat Lower Urinary Tract after Cauda Equina Injury and Repair*, in *Journal of Neuroscience*. 2006. p. 8672-8679.
14. Hoang, T.X., et al., *Acute implantation of an avulsed lumbosacral ventral root into the rat conus medullaris promotes neuroprotection and graft reinnervation by autonomic and motor neurons*, in *Neuroscience*. 2006. p. 1149-1160.
15. Bigbee, A.J., T.X. Hoang, and L.A. Havton, *At-level neuropathic pain is induced by lumbosacral ventral root avulsion injury and ameliorated by root reimplantation into the spinal cord*, in *Experimental Neurology*. 2007. p. 273-282.
16. Chang, H.-Y. and L.A. Havton, *Re-established micturition reflexes show differential activation patterns after lumbosacral ventral root avulsion injury and repair in rats*, in *Experimental Neurology*. 2008. p. 291-297.
17. Chang, H.-Y. and L.A. Havton, *Surgical implantation of avulsed lumbosacral ventral roots promotes restoration of bladder morphology in rats*, in *Experimental Neurology*. 2008, Elsevier Inc. p. 117-124.

18. Havton, L.A. and T. Carlstedt, *Repair and rehabilitation of plexus and root avulsions in animal models and patients*, in *Current Opinion in Neurology*. 2009. p. 570-574.
19. Deumens, R., et al., *Repairing injured peripheral nerves: bridging the gap.* Progress in neurobiology, 2010. **92**(3): p. 245-276.
20. Hoke, A., et al., *Schwann cells express motor and sensory phenotypes that regulate axon regeneration.*, in *Journal of Neuroscience*. 2006. p. 9646-9655.
21. Chew, S., et al., *The effect of the alignment of electrospun fibrous scaffolds on Schwann cell maturation*, in *Biomaterials*. 2008. p. 653-661.
22. Chew, S.Y., et al., *Aligned Protein-Polymer Composite Fibers Enhance Nerve Regeneration: A Potential Tissue-Engineering Platform.*, in *Adv. Funct. Mater.* 2007. p. 1288-1296.
23. Fu, S.Y. and T. Gordon, *Contributing factors to poor functional recovery after delayed nerve repair: prolonged axotomy.*, in *J. Neurosci.* 1995. p. 3876-3885.
24. Fu, S.Y. and T. Gordon, *Contributing factors to poor functional recovery after delayed nerve repair: prolonged denervation.*, in *J. Neurosci.* 1995. p. 3886-3895.
25. Hoke, A., et al., *A decline in glial cell-line-derived neurotrophic factor expression is associated with impaired regeneration after long-term Schwann cell denervation.*, in *Experimental Neurology*. 2002. p. 77-85.
26. Midha, R., et al., *Regeneration into Protected and Chronically Denervated Peripheral Nerve Stumps*, in *Neurosurgery*. 2005. p. 1289-1299.
27. Furey, M.J., et al., *Prolonged target deprivation reduces the capacity of injured motoneurons to regenerate.* Neurosurgery, 2007. **60**(4): p. 723-733.
28. Sroga, J.M., et al., *Rats and mice exhibit distinct inflammatory reactions after spinal cord injury*, in *J. Comp. Neurol.* 2003. p. 223-240.
29. Popovich, P.G., P. Wei, and B.T. Stokes, *Cellular inflammatory response after spinal cord injury in Sprague-Dawley and Lewis rats.*, in *J. Comp. Neurol.* 1997. p. 443-464.
30. Kigerl, K.A., V.M. McGaughy, and P.G. Popovich, *Comparative analysis of lesion development and intraspinal inflammation in four strains of mice following spinal contusion injury*, in *J. Comp. Neurol.* 2005. p. 578-594.
31. Carlstedt, T., et al., *Spinal nerve root repair and reimplantation of avulsed ventral roots into the spinal cord after brachial plexus injury.*, in *Journal of Neurosurgery*. 2000. p. 237-247.
32. Carlstedt, T., et al., *Return of function after spinal cord implantation of avulsed spinal nerve roots.*, in *Lancet*. 1995. p. 1323-1325.
33. Wang, X., et al., *Urocortin-Deficient Mice Display Normal Stress-Induced Anxiety Behavior and Autonomic Control but an Impaired Acoustic Startle Response*, in *Molecular and Cellular Biology*. 2002. p. 6605-6610.
34. Yamauchi, N., et al., *Distribution of Urocortin 2 in Various Tissues of the Rat*, in *J Neuroendocrinol*. 2005. p. 656-663.
35. Kuperman, Y. and A. Chen, *Urocortins: emerging metabolic and energy homeostasis perspectives*, in *Trends in Endocrinology & Metabolism*. 2008. p. 122-129.

36. Ohata, H. and T. Shibasaki, *Effects of urocortin 2 and 3 on motor activity and food intake in rats*, in *Peptides*. 2004. p. 1703-1709.
37. Staub, D.R., F. Spiga, and C.A. Lowry, *Urocortin 2 increases c-Fos expression in topographically organized subpopulations of serotonergic neurons in the rat dorsal raphe nucleus*, in *Brain Research*. 2005. p. 176-189.
38. Roppolo, J.R., I. Nadelhaft, and W.C. de Groat, *The organization of pudendal motoneurons and primary afferent projections in the spinal cord of the rhesus monkey revealed by horseradish peroxidase.*, in *J. Comp. Neurol.* 1985. p. 475-488.
39. Vanderhorst, V.G., et al., *Monosynaptic projections from the nucleus retroambiguus to motoneurons supplying the abdominal wall, axial, hindlimb, and pelvic floor muscles in the female rhesus monkey.* Journal of Comparative Neurology, 2000. **424**(2): p. 233-250.
40. Courtine, G., *Kinematic and EMG Determinants in Quadrupedal Locomotion of a Non-Human Primate (Rhesus)*, in *Journal of Neurophysiology*. 2005. p. 3127-3145.
41. Courtine, G., *Performance of locomotion and foot grasping following a unilateral thoracic corticospinal tract lesion in monkeys (Macaca mulatta)*, in *Brain*. 2005. p. 2338-2358.
42. Holmes, G.M., et al., *External anal sphincter hyperreflexia following spinal transection in the rat.*, in *J Neurotrauma*. 1998. p. 451-457.
43. Jasmin, L., et al., *Schwann cells are removed from the spinal cord after effecting recovery from paraplegia.* The Journal of Neuroscience, 2000. **20**(24): p. 9215-9223.
44. Grahn, P.J., et al., *Implantation of cauda equina nerve roots through a biodegradable scaffold at the conus medullaris in rat.*, in *Spine J*. 2014. p. 2172-2177.
45. Pajenda, G., et al., *Spatiotemporally limited BDNF and GDNF overexpression rescues motoneurons destined to die and induces elongative axon growth*, in *Experimental Neurology*. 2014, Elsevier Inc. p. 367-376.
46. Su, H., et al., *Ventral root re-implantation is better than peripheral nerve transplantation for motoneuron survival and regeneration after spinal root avulsion injury.* BMC surgery, 2013. **13**(1): p. 21.
47. Li, K., et al., *Erythropoietin Attenuates the Apoptosis of Adult Neurons After Brachial Plexus Root Avulsion by Downregulating JNK Phosphorylation and c-Jun Expression and Inhibiting c-PARP Cleavage*, in *J Mol Neurosci*. 2015.
48. Fu, R., et al., *Lithium enhances survival and regrowth of spinal motoneurons after ventral root avulsion.*, in *BMC Neurosci*. 2014. p. 84.
49. Li, L., Y. Zuo, and J. He, *Preconditioning crush increases the survival rate of motor neurons after spinal root avulsion.* Neural regeneration research, 2014. **9**(5): p. 540.
50. Chew, D.J., T. Carlstedt, and P.J. Shortland, *The Effects of Minocycline or Riluzole Treatment on Spinal Root Avulsion–Induced Pain in Adult Rats*, in *The Journal of Pain*. 2014. p. 664-675.

51. Spejo, A.B., et al., *Neuroprotective effects of mesenchymal stem cells on spinal motoneurons following ventral root axotomy: Synapse stability and axonal regeneration*, in *Neuroscience*. 2013. p. 715-732.
52. Torres-Espín, A., et al., *Neuroprotection and Axonal Regeneration After Lumbar Ventral Root Avulsion by Re-implantation and Mesenchymal Stem Cells Transplant Combined Therapy*, in *Neurotherapeutics*. 2013. p. 354-368.

Chapter 5 Nanofiber-Hydrogel Composite for Soft-Tissue Regeneration

5.1 Background

5.1.1 Soft Tissue Reconstruction.

Devastating soft tissue losses from tumor extirpation, trauma, aging, or congenital malformation affect millions of people each year. The loss of tissues including skin, fat, and muscle lead to major functional and aesthetic disturbances that are difficult to treat by conventional means. As an example, over 300,000 partial mastectomies are performed in the United States each year, leading to disfiguring breast scars from the loss of breast soft tissue. Existing options for soft tissue restoration have significant drawbacks. Autologous tissue flaps requires moving soft tissues from another part of the body in lengthy surgical procedures that leave donor-site deficits [1, 2]. Prosthetic implants are prone to foreign-body response leading to fibrosis and encapsulation [3, 4]; Fat grafting involving placement of adipocytes harvested during liposuction is limited to small volumes and is hampered by poor graft survival [5, 6]. Finally, injectable hydrogel soft tissue fillers can be used, but these are suitable only for smaller defects and the volume restoration they provide is transient [7, 8]. A new generation of tissue engineering solutions has been proposed to focus on using hydrogel scaffolds as templates to regenerate soft tissues such as adipose tissue at the site of reconstruction.

5.1.2 Current Tissue Engineering Approaches to Soft Tissue Reconstruction

Adipose-derived stem cells (ASCs) have been identified in wound beds surrounding soft tissue defects [9]. They can be differentiated into soft tissues such as fat, when supported with a suitable matrix microenvironment. Therefore strategies to fill the repair site with functional materials have the potential to enable the regeneration of new tissue using the endogenous ASCs. Hydrogels have been widely studied as a scaffold matrix for the regeneration of tissue defects due to their three-dimensional (3D) nature and elastic properties, which are similar to those of soft tissues. Various methods have been used to generate hydrogel scaffolds with moduli similar to that of native fat tissues (~2 kPa) while maintaining their volume and shape against physical stress from the surrounding tissue [10, 11]. This requires higher crosslinking density and smaller average pore size, leading to low cellular infiltration and poor regeneration [12-14]. *The ability for hydrogel scaffolds to promote cellular infiltration is the key to successful soft tissue restoration*. Lack of vascular infiltration is responsible for the failure of large-volume fat grafting and other tissue engineering attempts. No currently available materials can fill the volume lost in soft tissue defects while promoting early vascularization and ASC differentiation to regenerate soft tissue.

5.1.3 Hydrogel Matrix to Promote Vascularization

Over the past few years, Li and Wen have developed a hyaluronic acid (HA) hydrogel conjugated with laminin-derived loop peptide (CCRRIKVAVWLC, 10 μM)

with optimized pore size and modulus (10 – 100 Pa) for stem cell transplantation [14]. They have shown that this hydrogel supports robust neural stem cell (NSC) migration and neurite sprouting from the differentiated cells. In a rat controlled cortical injury (CCI) model for traumatic brain injury, this hydrogel, when injected on day 3 after the CCI injury, promoted significant vasculature network formation filling the lesion site (> 10 mm) at 4 weeks to 6 months post implantation. This improved angiogenesis was attributed to the ability of this hydrogel to retain and present tissue-secreted growth factors, particularly vascular endothelial growth factor (VEGF). Literature reports also revealed that small HA degradation fragments of 3–10 disaccharide units were potent regulators of endothelial cell proliferation, migration, tubule formation, and angiogenesis [15]. In a recent study, we have tested the effectiveness of this HA hydrogel to deliver human fetal tissue derived-NSC spheroids in a brain lesion site after CCI injury. This HA hydrogel delivered robust vascular formation inside the scaffold matrix following transplantation. Regenerated blood vessels grew into the lesion and penetrated through the implanted matrix, and supported the survival and growth the neuronal progenitors. Even though these studies are not for adipose tissue regeneration, these results confirmed the unique ability of this optimized HA hydrogel composition in promoting host vascular ingrowth. More importantly, the hydrogel matrix is sufficiently porous to allow robust cell migration inside the hydrogel matrix. However, using this HA hydrogel directly for soft tissue reconstruction is not feasible, as its mechanical property is not sufficiently high to maintain the integrity of the implantation site—the surrounding adipose tissue has a modulus of more than 10-times higher. Increasing crosslinking density to improve its modulus will make it poorly permeable for cell infiltration and migration. *A new strategy*

is needed to increase the mechanical property without significantly decreasing the average pore size of the bulk hydrogel.

5.1.4 Scaffold Design for Soft Tissue Restoration

The composite concept has been widely used as a material-reinforcement mechanism. For example, adding hydroxyapatite particles into hydrogel can increase its stiffness, and the composite tensile modulus increases even more for elongated particles [16, 17]. Electrospun nanofiber meshes have been used widely as a tissue engineering substrate due to their topographical similarity to the native ECM. Of particular interest, the decellularized ECM of adipose tissue is highly fibrous and porous in nature (Fig. 5.1g) [18]. Several recent studies have attempted to recapitulate the fibrous components by introducing fragmented poly(lactide) (PLA) or chitosan fibers to a polyethylene glycol (PEG), polyacrylamide, or alginate hydrogel [19-21]. The fragmented fibers are mixed with hydrogel precursor solutions and incorporated into hydrogel during the gelation process to create a 3D architecture. These fiber-embedded hydrogels have shown improved mechanical properties over the corresponding hydrogels. However, there has been no report on testing host cell infiltration *in vivo*. In addition, these hydrogels are non-degradable and require adhesive ligands for adipocyte adhesion and differentiation.

5.1.5 Nanofiber-Hydrogel Composite Design

To achieve fiber-reinforcement effect while maintaining high porosity in the hydrogel phase, we propose an electrospun fiber-hydrogel composite that offers superior properties compared to other scaffolds. Beyond *blending* nanofibers and a hydrogel matrix that we have reported previously [19], we introduce here interfacial bonding between fiber surfaces and the hydrogel crosslinking network (Fig. 5.1). Such a *composite design* will not only *allow stronger mechanical reinforcement from the solid fiber component*, but also allow *independent tuning of bulk mechanical properties and the average pore size/porosity of the hydrogel phase*, *enabling both optimal cell infiltration properties and structural integrity*. We also expect that fibers may be employed as preferred cell adhesion substrates for ASCs and endothelial progenitors, therefore acting as a guide to support cell migration and ASC differentiation.

5.1.6 Innovation

The key innovation is the nanofiber-hydrogel composite design with interfacial bonding between nanofiber surfaces and the hydrogel network (Fig. 5.1a). This engineered composite has the potential to drastically improve the mechanical property of the hydrogel without significantly decreasing the average pore size in the hydrogel phase. The introduction of interfacial bonding can offer superior mechanical strengthening effect comparing to just physical blending of the two components. This study will map out the range of mechanical properties (compression and shear moduli) attainable with electrospun polycaprolactone (PCL) fiber-HA hydrogel composites in contrast to blends. The second innovation is the demonstration of such a nanofiber-hydrogel composite to

restore soft tissue defects. Our preliminary characterization demonstrates that the composite shares structural characteristics with adipose tissue (Fig. 5.1) [7, 22]. We hypothesize that this composite offers structural integrity and mechanical properties important for soft tissue regeneration. This study will also demonstrate the versatility and efficiency of composites comparing to hydrogels.

The successful completion of this project will deliver an off-the-shelf solution for the restoration of missing soft tissue volume, particularly for larger defects where establishing vascular network, maintaining tissue repair site integrity, promoting cell migration and organization, and recruiting host cells are all crucial to a sustainable tissue restoration. The extensive clinical track record for the materials components used in this composite design, i.e. HA hydrogel and biodegradable polyester fibers, together with our preliminary data on tissue compatibility, suggests superior tissue compatibility and a straightforward regulatory approval path for clinical translation.

5.2 Methods

Thiolated hyaluronic acid (HA) was purchased from ESI BIO (Alameda, CA). Poly(ethylene glycol) diacrylates was purchased from Laysan Bio, Inc (Arab, AL).The followings were obtained from Sigma; poly(e-caprolactone), ethylamino-maleimide, acrylic acid, Toluidine blue O, N-hydroxysuccinimide (NHS), cysteine, bovine serum albumin (BSA), acetic acid and Triton™ X-100. Dulbecco's modified eagle medium

(DMEM), fetal bovine serum (FBS), penicillin/streptomycin, Alexa Fluor® 568 Phalloidin and 4',6-diamidino-2-phenylindole (DAPI) were purchased from Invitrogen Life Technologies. Ethyl(dimethylaminopropyl) carbodiimide (EDC) was obtained from AnaSpec, Inc. (Fremont, CA). All other chemicals and reagents were of analytical grades.

5.2.1 Electrospinning of PCL nanofibers for rheology experiments

In order to fabricate two different diameters of PCL fibers, 11.0 and 8.5 % (w/v) PCL solution were prepared in a mixture of dichloromethane and dimethylformamide (9:1, v/v) and a mixture of chloroform and methanol (3:1, v/v), respectively. Each homogenous PCL solution was loaded a syringe with a metallic needle of 27 G. Then, electrospinning was performed with following parameters; 1.0 ml/h of a feeding rate, 15 kV of an applied positive voltage for a metallic needle, and 12 cm of a distance between the end of a needle to a ground. Morphology of fibers was observed using a field-emission scanning electron microscope (FESEM, JEOL 6700F) and a diameter of fibers was measured with FESEM images using ImageJ software (US National Institutes of Health, Bethesda, MD).

5.2.2 Electrospinning for in vivo composites

Spinning conditions: 16%w/v PCL (95% 45.000 Mn PCL, 5% 80,000 Mn PCL, both from Sigma) in a solvent mixture of dichloromethane and dimethylformamide (9:1, w/w). The fibers were spun at a rate of 5.25ml/hour through a blunt 27gauge needle

separated 10 cm from the face of the grounded wheel, spinning at 1000 rpm. The applied voltage was 15kV and the electrospinning pump was rastered back and forth across the 85 mm travel distance for 140 passes at 2 mm/sec (about 4 hours). The fiber sheet was then cut into 14cm-diameter individual sheets for functionalization.

5.2.3 Preparation of surface-functionalized fibers with MAL

In order to surface-functionalize on fibers with MAL, the fiber surface was first modified with carboxyl groups by grafting poly(acrylic acid) (PAA) according to the literature with a minor modification [23]. Briefly, fibers were plasma-treated under 280 mmHg with oxygen atmosphere at room temperature for 10 minutes to induce free radicals on a surface of fibers. Then 70 mg of fibers in 10 ml of 3 or 10 % (v/v) acrylic acid solution in 0.5 mM $NaIO_3$ was exposed to UV (36 mW/cm^2, DYMAX Light Curing Systems 5000 Flood, Torrington, CT) for 90 seconds for photo-polymerization of PAA on fibers surface (PAA-fibers). After incubating PAA-fibers at room temperature for 20 minutes, PAA- fibers were washed with 20 ml of deionized water three times to remove unreacted acrylic acid. After completely air-drying PAA-fibers, a density of carboxyl groups on PAA-fibers were determined by toluidine blue O (TBO) assay with the assumption that TBO interacts with a carboxyl group on fibers at 1:1 of molar ratio [J Biomed Mater Res 2003, 67, 1093-1104]. Briefly, PAA-fibers (1 x 1 cm^2) were completely immersed in 1 ml of 0.5 mM TBO solution in 0.1 mM of NaOH (pH 10) after soaking 20 μL of 50% (v/v) ethanol and reacted with gentle shaking at room temperature for 5 h. After washing them with 0.1 mM NaOH (pH 10), adsorbed TBO on a surface of

PAA-fibers was desorbed using 1 ml of 50 % (v/v) acetic acid with vigorous shaking at room temperature for 1 hour. Then an optical density of supernatant was measured at 633 nm using a microplate reader (BioTek Synergy2, Winooski, VT). TBO in 50 % (v/v) acetic acid was used as a standard.

PAA-fibers were ground to prepare fiber fragments using a cryogenic mill (Freezer/Mill 6770, SPEX SamplePrep, Metuchen, NJ) with following parameters; 10 cycles of 1 min for milling and 3 minutes for cooling in liquid nitrogen. After collecting PAA-fiber fragments into a 50-ml conical tube, PAA-fiber fragments were completely dispersed in 10 ml of a mixture of isopropylacohol and distilled water (1:1, v/v) to be modified with aminoethyl-MAL on a surface of fibers. Briefly, NHS and EDC were added to the PAA fibers to activate carboxyl groups of the PAA on the fibers. the molar ratios of both NHS and EDC were 4-to-1 as compared to the carboxyl groups to ensure complete conjugation. The activation was performed with gently shaking at room temperature. After 1 hour, aminoethyl-MAL was added into the carboxyl groups-activated fibers with 1 to 2 of molar ratio of carboxyl groups to aminoethyl-MAL. Then the reaction was performed with gently shaking at room temperature for 12 hours. Surface-functionalized fibers with MAL were lyophilized after washing with distilled water three times. Here, a density of MAL on fibers was on the assumption that all of carboxyl groups on a surface of fibers were completely substituted by MAL.

5.2.4 Preparation of fiber-HA hydrogel composites

For preparing a fiber-HA hydrogel composite, thiolated HA and PEGDA were completely dissolved in PBS (pH 7.4) to the desired concentration of 12.5 mg/mL and 100 mg/mL, respectively. MAL-fibers with the desired concentration of 25 mg/mL were completely dispersed in PBS (pH 7.4). The suspension of nanofibers, HA, PEG-DA, and PBS are then serially added to reach the formulation's desired final concentration. After homogenous mixing the composite precursor solution, for rheological studies, 100 μL of the composite precursor solution was poured into a mold (ϕ = 8 mm) and incubated at 37 °C for 2 h for gelation. For compression studies, 200 μL of precursor solution is added to a cylindrical Teflon mold (ϕ = 6.35 mm, h = 6.35 mm) and incubated as above. In order to observe morphology of cross-section of a fiber-HA hydrogel composite and HA hydrogel using FESEM, a composite and HA hydrogel were dehydrated by serial ethanol washing (10 min each at 50%, 70%, 80%, 90%, 100%, and 100% Ethanol) before either critical point drying (Samdri-795, Tousimis, Rockville, MD) or chemical drying (HDMS). The samples were freeze-fractured in liquid nitrogen to reveal the internal pore structure. The structure was sputter coated with a 10-nm layer of platinum (Hummer 6.2 Sputter System, Anatech UDA, Hayward, CA), then imaged with a field-emission SEM (JEOL 6700F, Tokyo Japan).

For preparation of the composites for the in vivo animal studies, the thiolated HA was reconstituted to 12.5 mg/mL in PBS. The PEG-DA was dissolved to 100 mg/mL in PBS. The MAL-fibers were re-suspended to 25 mg/mL in sterile PBS. The fibers were first combined with the HA solution and allowed to react for 10 minutes before being combined with the PEG-DA to obtain the desired final concentrations. The suspension

was then immediately pipetted into the cylindrical Teflon molds (McMaster-Carr, Robbinsville, NJ), with 300 μL into cylindrical molds 11.125 mm in diameter and 3mm in height for the in vivo samples. The gels were then placed into the 37°C incubator to gel overnight.

In order to confirm the effect of interfacial bonding between thiol groups of HA and MAL on fibers, MAL on fibers was quenched using cysteine for preparing a quenched fiber-HA hydrogel composite. Briefly, 1 mg of fibers was dispersed in 1 ml of cysteine solution in PBS (pH 8.0) for a molar ratio of MAL to cysteine was 1 to 2. After quenching the MAL with gentle shaking at room temperature for 12 hours, MAL-quenched fibers were washed with 1 ml of distilled water five times to remove unreacted cysteine and lyophilized.

5.2.5 Mechanical properties of fibers-HA hydrogel composites

Compressive test. The hydrogel precursor suspension was pipetted into the cylindrical Teflon molds (McMaster-Carr, Robbinsville, NJ), with 200 μL into cylindrical molds 6.35 mm in diameter and 6.35 mm in height for compression testing. The gels were then placed into the 37°C incubator to gel overnight. The gels were removed from their molds and immediately tested via unconfined uniaxial compression between two parallel plates with the Endura TEC mechanical tester ELF 3200 Series, BOSE ElectroForce, Eden Prairie, MN). The samples were compressed to 50% strain, with the elastic modulus determined from the slope of the linear portion of the stress-

strain curve from 10% to 20% strain. The samples were tested three times each, and three samples were tested per group for determining the average compressive modulus. In order to measure compressive modulus of rehydrated fiber-HA hydrogel composites, the composites were lyophilized and rehydrated with 1 ml of PBS (pH 7.4) at 37 °C for 24 h. For fatigue-testing, the compression samples were repeatedly cycled from 0% to 25% strain at 0.1 Hz.

Rheological test. Shear storage modulus (G′) of various fiber-HA composites were measured using an oscillating rheometer (ARES-G2 Rheometer, TA Instruments, New Castle, DE) with a parallel plate (ϕ = 8 mm). Oscillatory frequency sweep was employed to monitor variation of G' from 1 Hz to 10 Hz with constant strain of 10 %.

5.2.6 Migration of hASCs in fiber-HA hydrogel composites

Human adipose-derived stem cells (hASCs) were cultured in high glucose DMEM containing 10 % of FBS, 1 % of penicillin/streptomycin, and 1 ng/ml of bFGF. The culture medium was exchanged three times per week for optimal growth. In order to prepare hASC spheroids, 50 μL of hASCs solution (5.6 x 10^5 cells/ml) was poured into a casted micro-molded agarose gel (MicroTissues® 3D Petri Dish® micro-mold spheroids, 96-holes) to prepare hASCs spheroids and incubated with gently shaking at 37 °C for 24 hours.

HA and PEGDA were completely dissolved in PBS (pH 7.4) with final concentration of 4.5 and 2.5 mg/ml for HA and 5.0 mg/ml for PEGDA. Fibers pre-wetted with 20 μL of 50 % (v/v) ethanol were completely dispersed in PEGDA with final concentration of 10.0 mg/ml, then HA added into a mixture of fibers and PEGDA. 30 μL of composite precursor solution was poured into each well of a 96-well tissue culture plate and incubated to crosslink at 37 °C for 1 hour to avoid reaching hASCs spheroids on a surface of tissue culture plate. Then, 50 μL of composite precursor solution with 3 to 5 of hASCs spheroids was poured into the each well. After crosslinking at 37 °C for 1 hour, 200 μL of fresh media were added into the each well and the media were exchanged every other day. In order to observe migrated cells from hASCs spheroids inside the composites, F-actin and nuclei of hASCs were stained with Alexa Flour® 568 Phalloidin and DAPI, respectively. Briefly, after 4 days of cultivation, the composites with hASCs spheroids were fixed with 100 μL of 4 % (v/v) paraformaldehyde at room temperature for overnight. Then, after washing three times with PBS (pH 7.4), the composites were incubated with 100 μL of 1 % (w/v) BSA in PBS to inhibit non-specific staining at 4 °C for overnight and washed three times with PBS. Subsequently, the composites were incubated with 100 μL of 0.1 % (v/v) Triton-X 100 in PBS at room temperature for 1 hours. After washing three times with PBS, 100 μL of 160 nM Alexa Fluor® 568 Phalloidin was added into each composites and incubated at room temperature for 4 hours. Then, after removing the supernatant, the composites were incubated with 100 μL of 0.5 μg/ml DAPI at room temperature for 1 hour. After washing three times with PBS again, the migrated hASCs were observed using confocal laser scanning microscope

(CLSM, Carl Zeiss LSM780, Germany) at ex. 561 nm and em, 570-600 nm for Alexa Fluor® 568 Phalloidin, and ex. 405 nm and em. 385-420 nm for DAPI.

5.2.7 Performance of a fiber-hydrogel composite in vivo

The thiolated HA was reconstituted to 12.5 mg/mL in PBS. The PEG-DA was dissolved to 100 mg/mL in PBS. The MAL-fibers were re-suspended to 25 mg/mL in sterile PBS. The fibers were first combined with the HA solution and allowed to react for 10 minutes before being combined with the PEG-DA to obtain the desired final concentrations. The suspension was then immediately pipetted into the cylindrical Teflon molds (McMaster-Carr, Robbinsville, NJ), with 300 μL into cylindrical molds 11.125 mm in diameter and 3 mm in height. The gels were then placed into the 37°C incubator to gel overnight. The two formulations were selected so as to match the 2kPa stiffness of fat tissue. The HA-alone formulation was 10 mg/mL PEG-DA and 9 mg/mL HA-SH, and the HA-fiber composite formulation was 5 mg/mL PEG-DA, 5 mg/mL HA-SH, and 12.5 mg/mL dispersed nanofibers.

To study the biocompatibility of the composite nanomaterial scaffolds, the scaffolds were implanted under the inguinal fat pads of Sprague-Dawley rats and observed for varying lengths of time. Under volatile anesthesia, two 1 cm incisions were made bilaterally, just proximal to the inguinal crease. Following blunt dissection of subcutaneous tissues, the inguinal fat pad was exposed. It was elevated with meticulous hemostasis using electrocautery and with careful preservation of feeding vessels.

Scaffolds were implanted under the fat pad on the right side of the animal. The left side received no implant and served as sham surgery control. Both sides were closed in a standard layered fashion. Animals were observed for 7, 14, 30, and 90 days. At timepoints for collection, animals were sacrificed and the inguinal fat pad with and without scaffolds was exposed and fixed in 4% PFA. The specimens were imbedded and sectioned for standard hematoxylin and eosin staining.

5.2.8 Statistical analysis

All the results are expressed in mean values and the standard deviation. The statistical significance between a pair of groups was determined by conducting a One Way ANOVA with SigmaPlot 12.0 software (SPSS); a value of $p < 0.05$ was considered statistically significant.

5.3 Results

5.3.1 Design of a fiber-HA hydrogel composite.

The fibers could form the fibrous architecture that can often be seen in the native extracellular matrix, aiding cell migration and reinforcing the initially-low mechanical properties of the hydrogel. By introducing interfacial bonding between the hydrogel and fibers (Fig. 5.1a, b), the composite is strengthened without decreasing the average pore size and porosity (Fig. 5.1) that would significantly hinder cell migration. We also expected that the mechanical properties could be tuned by controlling the density of the

interfacial bonding between the hydrogel and the surface of fibers. Here, we prepared surface-functionalized fibers with maleimide (MAL) to introduce the interfacial bonding with thiolated hyaluronic acid (HA-SH) (Fig. 5.1). The surface of electrospun poly(ε-caprolactone) (PCL) fibers was treated with O_2 plasma to induce free-radicals onto its surface before grafting poly(acrylic acid) (PAA). The carboxyl groups was activated by coupling reagents, NHS and EDC, then N-(2-aminoethyl)maleimide was reacted to the activated carboxyl groups (Fig. 5.8). Subsequently, MAL-functionalized fibers were introduced to hydrogel precursor solution composed of HA-SH and PEGDA for fabricating a fiber-hydrogel composite. The thiol groups of the HA were employed to form a gel by reacting with both the MAL groups on the fibers and the DA groups of the PEG linker. Interestingly, a cross-section of a fiber-hydrogel composite showed a fibrous 3D structure with a high porosity (Fig. 5.1), compared to a cross-section of HA hydrogel with a similar crosslinking density. The resulting composites showed even distribution of nanofibers across both the width and height of the composite, enabling isotropic reinforcement. Also, a rehydrated fiber-HA hydrogel composite showed 99.34 % of volume recovery after lyophilization while HA hydrogel showed 70.17 % of volume recovery (Fig. 5.1d).

5.3.2 Compressive modulus of a fiber-HA hydrogel composite.

First, we verified that the composite had its maximal stiffness (under shear) when the reactive groups were equal on a molar basis. The thiol groups on the HA can react with either the MAL groups on the nanofibers or the acrylate groups on the PEG-DA, so

when the molar ratio of SH to (DA+MAL) was approximately 1 to 1, the gels showed an optimal shear storage modulus. Therefore, we maintained this ratio for all of our subsequent studies. The gels underwent unconfined compression testing to evaluate the elastic modulus of HA hydrogel and fiber-HA hydrogel composites (Fig. 5.2). The reinforcing effect of the functionalized nanofibers can be seen in the compressive stress when strained to 50% (Fig 5.2a). The compressive stress was 3.1-fold greater in the 1.0-μm fiber group than the hydrogel-only group, showing the effect of mechanical reinforcement. The 286-nm fiber group showed even more pronounced reinforcement effect with a compressive stress of 4.2-fold higher at the 50% strain. Interestingly, the stiffening effect of the 286-nm fibers was greatly reduced to only 1.3-fold over the hydrogel when the maleimide groups were quenched prior to gelation, confirming that the interfacial bonding of the fiber to the hydrogel is crucial to the reinforcement effect of the functionalized fibers. Moreover, when the 286-nm fibers were not functionalized before forming the composite, the reinforcement effect was disappeared, resulting in composites barely stiffer than the hydrogel alone. The same reinforcement effect can be seen when formulating stiffer gels by formulating composites with higher concentrations of HA and PEG-DA (Figure 5.2). The interfacial bonding also shows a dose-response in its stiffening of the composite gel, as adding progressively more maleimide groups to the nanofiber surface results in progressively stiffer materials providing more evidence of the importance of the interfacial bonding. The composites were also tested for changes in mechanical properties before and after dehydration and rehydration. The gels, with and without functionalized nanofibers of two different maleimide densities, were mechanically tested under compression. The gels were then lyophilized, then allowed to

rehydrate fully and tested for compression again. All samples maintained their stiffness after rehydration, indicating that the composites may be suitable for use clinically as a lyophilized product. While the HA-alone gel seemingly maintained its stiffness, the gel itself had compacted significantly during the dehydration-rehydration process, unlike the fiber-containing groups. The composite gels were also subjected to cyclic loading to test for fatigue-effects, with representative traces shown in figure 5.5. With repeated loading to 25% strain, the composite gels maintained their stiffness over time and were consistently stiffer than the hydrogel alone.

5.3.3 Shear storage modulus of a fiber-HA hydrogel composite.

In addition to the higher compression modulus, the Fiber-HA hydrogel composites showed a significantly higher shear storage modulus than the HA hydrogel alone (Fig. 5.3a). The shear storage modulus of a composite with 286-nm fibers was higher than that of a composite with 686-nm fibers (Fig. 5.3c). We also confirmed that the shear storage modulus of the composites increased by increasing the maleimide surface density on the 286-nm fibers, similarly to the modulus under compression testing (Fig. 5.3d). By introducing fibers with 62 nmol/mg MAL on its surface, the composite showed a 1.3-fold increase in its shear storage modulus compared to that of the HA hydrogel alone. Moreover, the shear storage modulus of a composite with 147 nmol/mg MAL on its fibers was increased 1.8-fold over the modulus of the 62nmol/mg MAL group, showing a clear dose response to the corresponding 2.4-fold increase in the MAL surface density on the fibers. When the MAL groups on the fibers were quenched prior to

gelation, the shear storage modulus correspondingly decreased compared to that of the unquenched fibers, similarly to what was seen in the compression testing. Additionally, the shear storage modulus of the composites was maintained when the frequency increased to 10 Hz while both the HA hydrogel alone and the composite with quenched fibers showed diminishing shear storage moduli at 10 Hz than those at 1Hz. The shear storage modulus of the composites was increased with increasing MAL surface density on fibers regardless of surface area (diameter) of fibers, indicating that the previously observed effect of fiber diameter on stiffness may have been a function of maleimide density (Fig. 5.3d). A linear regression was obtained from the correlation between the MAL surface density and shear storage modulus with R^2=0.93. Moreover, the composites showed a dose response to fiber loading, as the shear storage modulus of the composites increased with an increasing weight ratio of functionalized fibers to hydrogel components (Fig. 5.4).

5.3.4 Cell migration in a fiber-HA hydrogel composite in vitro.

We hypothesized that the fiber-HA hydrogel composite enhances cell migration compared to HA hydrogel because of (i) a higher porosity of the composite with a larger pore size, providing a spatiality for cell migration when they have the same mechanical properties and (ii) an ECM-mimicked fibrous architecture in the composite, allowing to intrinsically guide cell migration. Therefore, for demonstrating our hypothesis, we seeded spheroids of human adipose-derived stem cells (hASCs) as a model cell and a mimicked tissue chunk inside HA hydrogel and composites, then the hASCs spheroids

were cultured for 27 days (Fig. 5.6). ASCs were chosen due to their presence in fat tissues and importance in both angiogenesis and adipocyte formation. Although the composites have the similar Young's modulus, 1.9 kPa, to the HA hydrogel, the pore size of the composites is 2.08-fold bigger than that of HA hydrogel (Fig. 5.11). Hence, we obviously observed that hASCs migrated 3-dimensionally inside the composites (Fig. 5.6b-e) because the bigger pores can accommodate to migrate the cells, while hASCs maintained their spheroid shape without any cell migration in HA hydrogel (Fig. 5.6a). In particular, the cell migration was magnificently enhanced when the fibers were modified with the cell adhesion peptide, RGD, for the composite (Fig. 5.6c). However, in the in vivo setting, diffusion of factors into the composite from the local milieu should provide additional adhesive cues, lessening this difference. In some instances, partial fibers slightly formed a cluster during gelation due to hydrophobic interaction between PCL fibers, and it was observed bodies of cells preferentially grabbing the fibers clusters inside the composites (Fig. 5.6d and e). Furthermore, at the same HA and PEG-DA concentrations (Fig. 5.14), the composites showed enhanced cell migration as compared to the fiber-less group, showing that the nanofibers themselves could intrinsically help guide cell migration regardless of the porosity.

5.3.5 Tissue response and host tissue infiltration

To determine the therapeutic potential of these composite implants, we tested them *in vivo* in a rat fatpad model. The formulations of the implant groups were formulated to achieve the same initial 2 kPa stiffness as the composite gel and the target

adipose tissue. Thusly, the formulation of the HA-gel alone implant had a higher concentration of both thiolated HA and PEG-DA in order to match the stiffness of the fiber-composite group. Despite the higher concentrations, the HA-alone implants were unable to maintain their shape and volume over the course of the study. Under gross observation after 4weeks, the HA-alone implants were stretched out and significantly smaller in volume. Considering their gross appearance and their histological lack of infiltration, the HA-alone system cannot be optimized to be able to encourage cell infiltration and maintain a predetermined shape. The fiber-gel composite implants, however, well maintained their original shape under gross observation after 90 days in vivo. Remarkably, however, under histological observation the composites had been so thoroughly infiltrated that the border between implant and native tissue had become difficult to determine.

We have developed a soft tissue defect model in Lewis rats, where the inguinal fat pad is exposed and elevated using microsurgical techniques and the pre-shaped composites are placed underneath.. Even though this does not directly demonstrate the ability of such a composite for restoring large defects, it will establish the proof-of-principle and confirm all essential functionalities of the composite design, and lay the foundation for larger animal model to test the large defect restoration in more clinically relevant models.

In a pilot study, we implanted PCL nanofiber-HA hydrogel composites and HA hydrogels with similar moduli under the inguinal fat pad of 8–12 week old male Lewis

rats (n = 3 per time point). Both the HA hydrogel and composite groups showed good tissue compatibility at days 14 and 30 after transplantation (Fig. 5.7, POD 14, similar observations at POD 30. POD = Post-Operative Date). Histology at POD 30 did not show higher level of inflammatory response than sham surgery group. H&E and Masson's trichrome staining showed septation and cellular infiltration by native fat through the composite, capillary formation around the perimeter, and regeneration of glandular as well as adipocyte portions of native fat (Fig. 5.7). HA hydrogel control on the other hand, lacked cellular infiltration and formed a thin sheet of fibrotic tissue and foreign body response. This HA hydrogel was prepared with 2 kPa to ensure sufficient mechanical property. This result highlights the importance of porosity of the scaffold for cell infiltration.

At an early time point (2 weeks), mesenchymal cells from the wound bed were found infiltrating the material suggesting that the material has sufficient porosity to enable native cellular ingrowth (dark pink staining in Fig. 5.7). Importantly, cellular ingrowth was achieved even in the absence of exogenous growth factors. The presence of cells infiltrating the material rather than merely surrounding it, distinguishes this composite nanomaterial from other alloplastic materials in current use. The latter materials are walled off by fibrous capsule and are therefore less desirable for soft tissue reconstruction. At later time points (4 weeks), cellular ingrowth is even more apparent with the appearance of vacuolar areas that may represent nascent adipocyte differentiation.

5.4 Discussion

Hydrogels have been widely studied as a filler material for regeneration of tissue defects due to its 3D hydrated environment and high porosity, which facilitate cell migration. However, hydrogels have proven to be poor substitutes for volumetric defects, because the relatively weak mechanical properties of the hydrogel are insufficient to maintain its volume for the entire period of tissue regeneration, as the hydrogel can be easily degraded and collapsed by body fluids and internal and external stresses. To improve the mechanical properties of the hydrogel, the main strategies in the field have been to (i) increase the concentration of hydrogel precursors, (ii) increase the density of the crosslinking network inside the hydrogel, and to (iii) introduce reinforcing materials such as by embedding hydroxyapatite particles or laminating with fiber sheets [17, 24, 25]. Unfortunately, these very strengthening strategies inherently reduced the average pore size and porosity of the resulting hydrogel, preventing cells from being able to migrate into these hydrogels. Therefore, we sought to strengthen hydrogels by a new mechanism that would still retain the high porosity than allows for rapid cellular infiltration. We designed a composite material by introducing functionalized nanofibers that could strengthen the overall hydrogel composite while leaving the hydrogel phase largely intact, including porosity. The resulting fiber-hydrogel composite improves upon previous soft tissue composites because of two key components. Firstly, the nanofibers needed to be uniformly dispersed at a high loading level within the hydrogel to achieve isotropic strengthening. The tissue-engineering field has generally utilized electrospun

nanofibers as flat sheets or mats of fibers. These are then typically made into composites by impregnating the mats with a hydrogel precursor solution.

This greatly constrains the dispersion of the nanofibers throughout the hydrogel and limits the geometry of the composites to 2D sheets or tubes. While these geometries are useful for certain applications such as nerve repair or wound dressings, they are poor choices for repairing volumetric defects. By cryomilling the fiber sheets, we were able to reduce the average fiber length to the sufficiently short length that allow them to remain in suspension in aqueous solutions. Thus, we can easily pipette them into our hydrogel precursor solutions, creating a uniform dispersion of nanofiber fragments throughout the hydrogel volume before gelation. The solution can then be directly used as an injectable formulation, or added to molds to form scaffold gels of any arbitrary geometry, unlike the limited planar geometry of most electrospun nanofiber meshes. The composite structure of dispersed fibers within a hydrogel also recapitulates the fibrous architecture of the extracellular matrix (Fig 5.1g), providing adhesion sites that may aide cell migration within the composite.

Secondly, simply dispersing the nanofibers within the hydrogel is insufficient to form a strong composite. Our data indicates that merely including the nanofibers themselves provides very little improvement in the elastic modulus of the composite, with improvements occurring only when interfacial bonding is introduced. The interfacial bonding is necessary because without forming a strong linkage between the hydrogel and fiber components, the water and hydrogel components could slide past the fiber

components without transferring the loads to the stiffer material. Furthermore, the interface between such disparate materials could lead to delamination and failure in the composite. Further, PCL's initial hydrophobicity makes it difficult to disperse in aqueous solutions, as the fibers preferentially clump together and form clots that fall out of suspension. Plasma treatment and subsequent functionalization with carboxylic acid groups and amine groups greatly increases the hydrophilicity of the fibers and allows dispersion. The dramatic increase in mechanical properties only occurred when interfacial bonding occurred between the maleimide groups on the fiber surfaces and the thiol groups on the hyaluronic acid molecules. This covalent-strength bonding transfers loads more efficiently to the fibers during compression or tension, leading to a stiffer, stronger material. Moreover, the composites show a strong trend of increasing elastic moduli with increasing maleimide density, emphasizing its primacy in the strengthening mechanism, as well as the tunable nature of the reinforcement.

In this study, we were able to tune the mechanical properties of the fiber-hydrogel composite by various factors including the total surface area of fibers, the density of the functional maleimide groups on the fiber surface, and the amount of fibers loaded into the hydrogel. *Firstly,* composites with smaller diameter of fibers showed a higher compressive and shear storage modulus than those of composites with bigger diameter of fibers (Fig 5.2a and Fig. 5.3c). Similarly, in the literature, a single ultra-high molecular-weight polyethylene (UHMWPE) fiber (~25 μm), which was plasma activated using glutaraldehyde, showed approximately 2.36-fold increase of interfacial shear strength in a poly(vinyl alcohol) hydrogel compared to it of a UHMWPE fiber bundle of 60 [26].

Therefore, it is possible that decreasing the fiber diameter and thus increasing the fiber specific surface area may be an effective in improving the mechanical properties of the composite. However, each fiber group had a slightly different MAL surface density on the fibers (approximately 10-15 nmol/mg), so we cannot definitively determine the effect of surface area of fibers alone. Hence, *secondly*, composites were fabricated with the same diameter fibers, but with various MAL surface densities on the fibers (Fig. 5.3). The compression and shear storage moduli of composites were increased with increasing MAL surface density on the fibers. We have confirmed that a composite without the interfacial bonding showed only a slight enhancement of its compressive modulus (Fig. 5.2) by using fibers modified through the PAA step (carboxyl groups on fibers), but not the further MAL conjugation steps. We additionally confirmed the importance of the interfacial bonding by quenching the MAL groups on the fibers with cysteine prior to gelation. The cysteine conjugates to the maleimide group and prevents interfacial bonding between the fibers and hydrogel, which allows us to isolate just the effect of interfacial bonding, since the fibers were otherwise processed identically to the interfacial-bonding groups. Interestingly, the mechanical properties of the composites with the MAL-quenched fibers were dramatically diminished (Fig. 5.2a and Fig. 5.3b), with the MAL-quenched fiber group showing a lower compressive modulus than that of HA hydrogel-alone when the concentration of HA was 10mg/ml (Fig. 5.2). It is possible that the MAL-quenched fibers weakened the overall composite by delaminating easily at the interface of the fibers and hydrogel, as is seen in previous studies [26]. Also, the fibers without functional groups may be acting as an alien substance that inhibits gelation compared to a pure hydrogel composed of one component or without any alien substance

during gelation [21, 27]. Furthermore, we verified a significant correlation between shear storage modulus and the density of the interfacial bonding by composites with various MAL surface densities (Fig. 5.3c). These studies provide strong evidence that the mechanical properties of hydrogel could be reinforced and tuned by the interfacial bonding. Thirdly, the shear storage modulus of the composites was enhanced with an increasing weight ratio of fibers to hydrogel (Fig. 5.4). Thereby, it was confirmed that the weight ratio was another variable that can be used to tune the mechanical properties of a fiber-hydrogel composite. However, here, we confirmed that with increasing fiber loading, the shear storage modulus increases began to level off and even slightly decreased above 0.6 of the weight ratio. One possibility for this saturation effect may be that the density of interfacial bonding of a composite was diminished by how the excess fibers with MAL reacted with a large fraction of the thiol groups of HA, preventing them from reacting with the PEGDA for gelation. Considering that the highest shear storage modulus of the HA hydrogel was obtained with an equimolar amount of each functional group of HA-SH and PEGDA as well as the decreasing shear storage modulus with excess amounts of either HA-SH or DA (Fig. 5.9a), the excess MAL on the fibers with the increasing amount of fibers could disrupt the SH-to-DA bonding inside a composite.

Generally, implanted biomaterials have to withstand numerous internal and external stresses during regeneration of the tissue defect. Although the stress is not severe and continuous, we performed stress resistance tests under a repeating condition and a high frequency (10 Hz) to mimic such stresses (Fig. 5.5 and Fig. 5.3). Both the HA hydrogel and fiber-HA hydrogel composite withstood without any damage or reduction

of their mechanical strength during repeating compressive strain. Noticeably, composites with the interfacial bonding retained their shear storage modulus at 10Hz of frequency, whereas the shear storage modulus of the HA hydrogel and the composite without the interfacial bonding were diminished at 10Hz. This trend indicates that the interfacial bonding with the dispersed fibers is crucial to the reinforcement of the composite's mechanical properties. In addition, the fiber-HA composites maintained their dimensions and their Young's moduli after being subjected to lyophilization and subsequent rehydration, while the HA-alone gel shrank substantially under the same process (Fig. 5.1c and Fig 5.5). This shape, volume, and stiffness maintenance after dehydration and rehydration is an important feature for clinical translation of this technology, as having a lyophilized form of the composite would make it easier to sterilize and store the commercial product.

For soft tissue reconstruction, the ideal implanted scaffold would immediately fill the defect void, but would also serve as a substrate for the body's own cells to grow into the scaffold, proliferate and differentiate into the proper tissue phenotype, eventually replacing the artificial scaffold with normal, healthy tissue. Thus, it is critically important that relevant cells would be able to migrate within the hydrogel or composite scaffold To determine the potential for relevant cell types to migrate within the scaffolds, we seeded hASC spheroids inside HA hydrogels and fiber-HA hydrogel composites and evaluated their cell migration. The hASCs could not migrate inside the HA hydrogel-alone because the HA hydrogel was too soft to serve the traction forces for cell migration (Fig. 5.6a) [28]. Interestingly, although shear storage modulus of the composites was similar to that

of the HA hydrogel, the hASCs were able to significantly migrate away from a spheroid inside the composites (Fig. 5.6). One hypothesis is that the fibers inside a composite may be providing adhesion sites to guide cell migration similarly to the fibril components of the native ECM of adipose tissue. We previously have demonstrated that aligned and random fibers can be a critical factor for cell adhesion, proliferation, differentiation, and migration in various cell types [29-33]. Especially, it was observed that cells recognized fibers as a guide matrix, as their cytoskeletons aligned with and followed along the underlying fibers [30, 31]. However, the diameter of the fibers inside the composites did not affect the migrating cells, as they migrated robustly in composites with either 1000-nm or 286-nm nanofibers (Fig. 5.14).

The porosity and cell migration effects seen in benchtop testing and in vitro cell culture translated into profound differences during in vivo testing of the composites. The hydrogels formulated to fat-mimicking 2 kPa stiffness without fibers had a porosity too low for cellular infiltration. The cellular response was to wall off the hydrogel with a thick layer of collagen, with the lack of infiltration or remodeling typical of a foreign body response. The nanofiber-hydrogel composite, however, had sufficient porosity to facilitate cellular ingrowth, vascularization, and cellular remodeling without the foreign body response. This offers the prospective of permanently filling the volumetric defect in the body with what will ultimately be the body's own tissue. The results were even more pronounced in the injectable formulation, which can form a tighter interface with the host tissue and showed signs of robust adipogenesis (Fig. 5.15).

5.5 Conclusion

The dispersion of functionalized nanofibers within a hydrogel forms a composite structure with the combined strengths of the two components. The interfacial bonding between the nanofibers and the hydrogel components is critical to making a strong composite, while maintaining high porosity and pore size to facilitate tissue and cell ingrowth. The resulting composite properties can be easily tuned by varying the fiber diameter, fiber loading level, maleimide density level, and the loading levels of the hydrogel components. This allows for lower crosslinking and higher porosity at a targeted overall stiffness, increasing cellular infiltration and subsequent tissue remodeling. The fibers themselves may also directly improve cellular migration by providing adhesion sites similar to that seen in the native ECM. The resulting composite implant can be tuned to match the stiffness of native fat tissue, yet remain permeability for cellular infiltration and remodeling. This novel composite is strong enough to immediately fill a volumetric defect of any arbitrary shape. The composite implant then serves as a permissive scaffold for the body's own cells to infiltrate into the composite, form blood vessels, and differentiate into cells like adipocytes. The scaffold will be slowly degraded away during tissue remodeling, until the initial defect void has been replaced fully by normal, healthy tissue. The composite structure has great potential for reconstructive and aesthetic surgery potential.

5.6 Figures

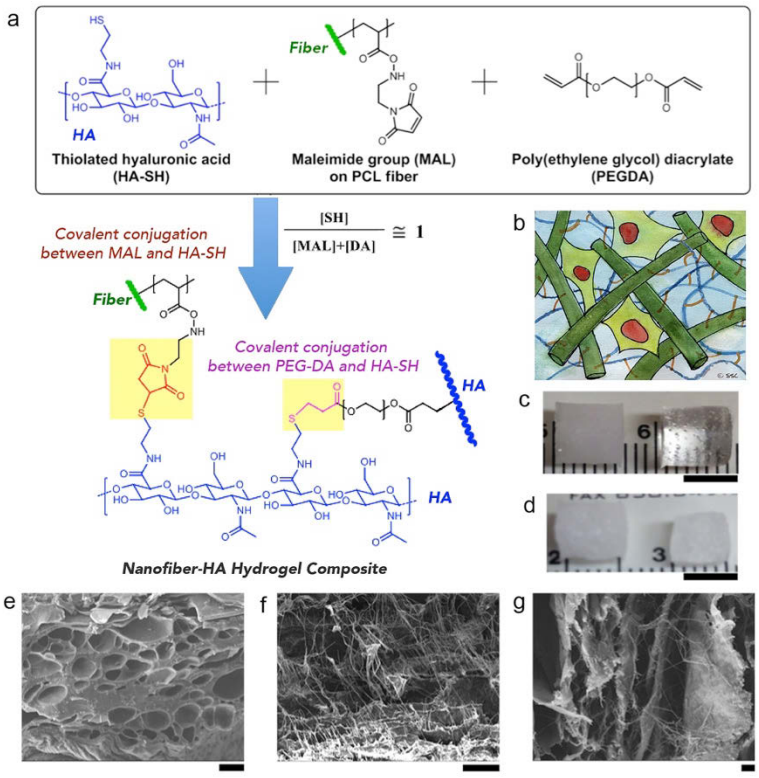

Figure 5-1: Design of a novel, ECM-mimicking fiber-hydrogel composite

(a) Synthesis scheme for the polycaprolactone (PCL) fiber-HA hydrogel composite; (b) Schematic illustration of the composite structure with interfacial bonding between PCL fibers and HA chain network; (c) Optical images showing the general appearance of a freshly prepared, cylindrical fiber-HA hydrogel composite (left) and a HA hydrogel (right) with the same dimensions (scale bar = 5 mm); (d) Optical images of the same set of samples after lyophilization and rehydration; (e–g) SEM images of cross-section of an HA hydrogel (scale bar = 40 m), a PCL fiber-HA hydrogel composite (scale bar = 100 m) and a decellularized native fat tissue (scale bar = 10 m).

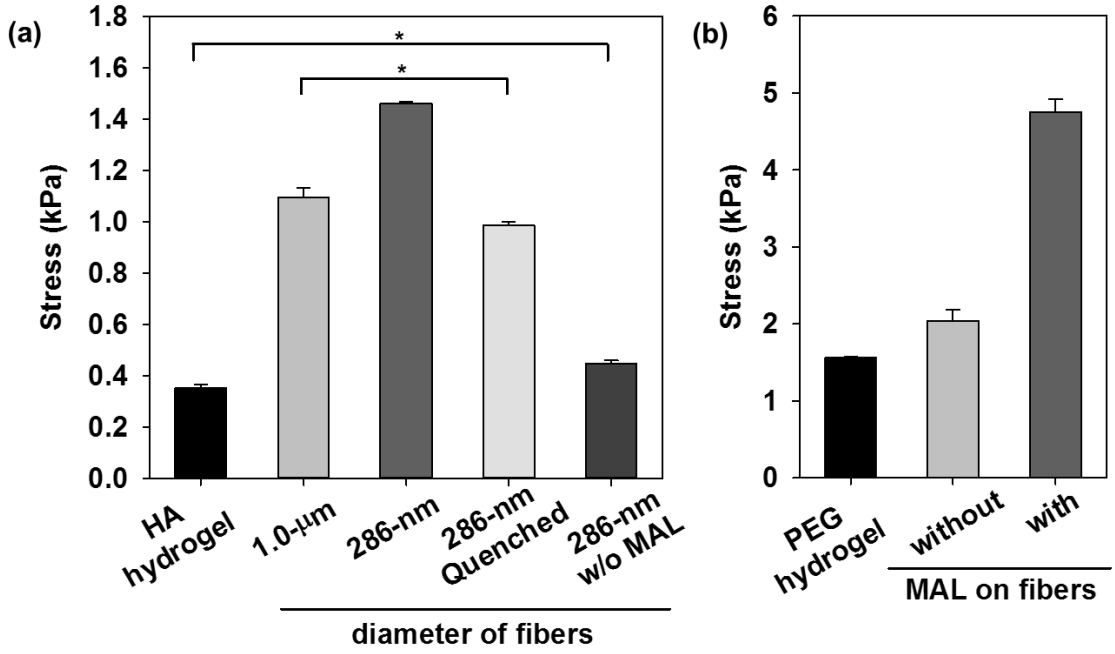

Figure 5-2: Effect of the fiber diameter and the interfacial bonding on reinforcing compressive modulus of (a) HA hydrogel and (b) PEG hydrogel.

(a) HA hydrogel and composites were prepared based on 4.5 mg/ml of HA. (b) PEG hydrogel and composites were prepared based on 30 mg/ml of PEGSH and 20 mg/ml of PEGDA, and 1.0-mm PCL fibers were used to synthesize the fiber-PEG hydrogel composites. The values of stress were measured at 50 % of strain. $*p < 0.05$ (Student-*t* test).

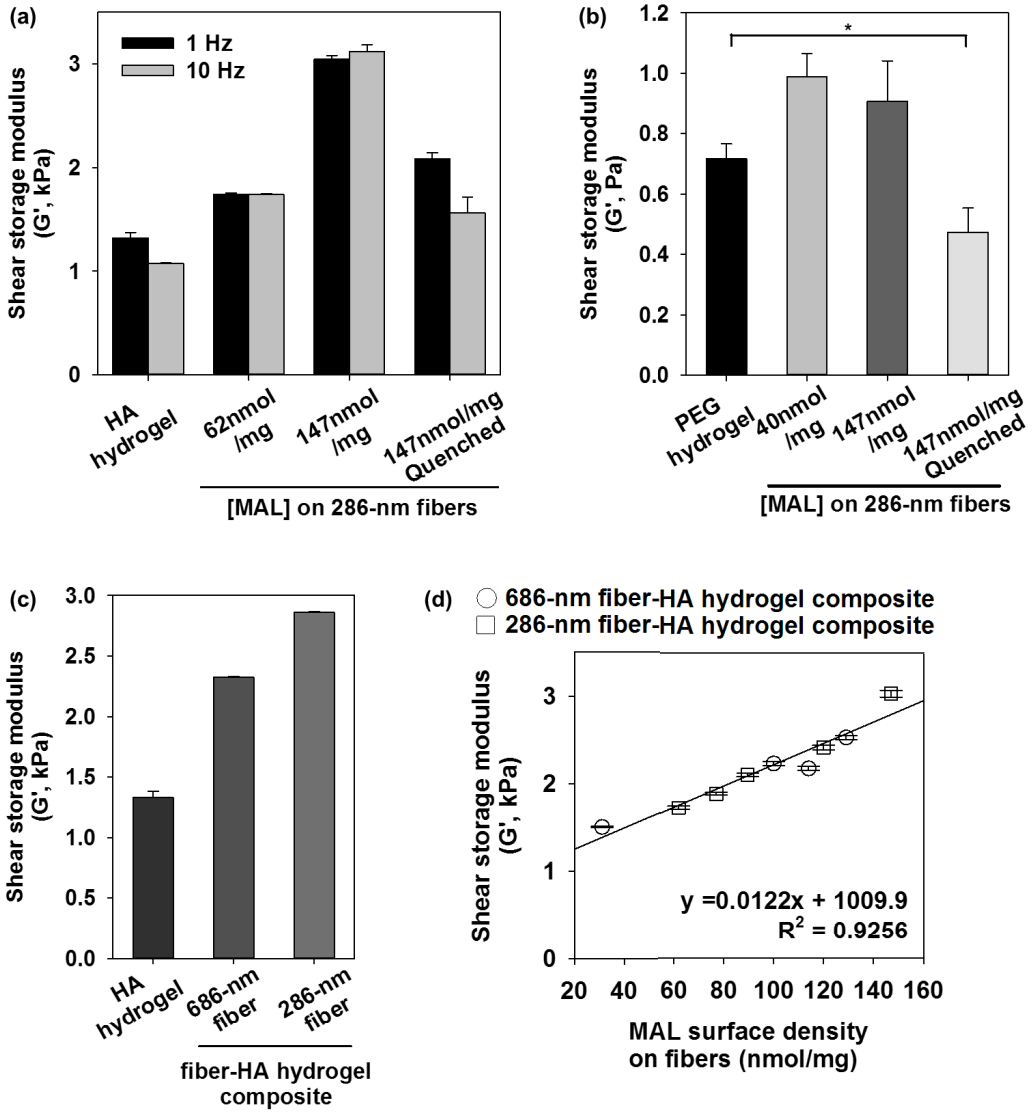

Figure 5-3: Effect of the interfacial bonding density and the fiber diameter on reinforcing shear storage modulus of HA hydrogel (a, c and d) and PEG hydrogel (b).

The values of shear storage modulus were measured at 1-Hz frequency in (b) through (d). *$p < 0.05$ (Student-t test).

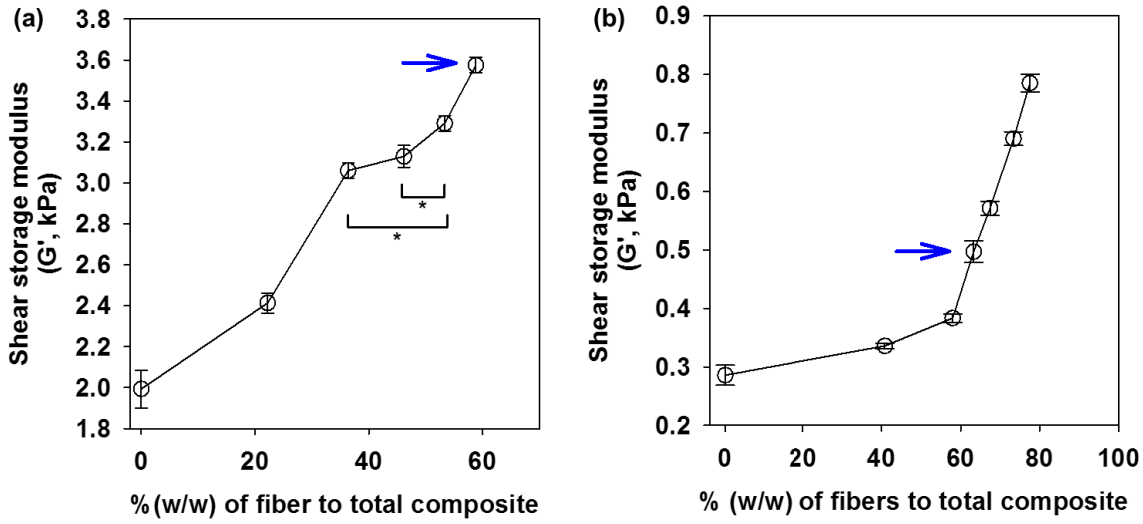

Figure 5-4: Effect of fiber-loading on shear storage modulus of HA hydrogel.

The HA hydrogel and composites were synthesized using a 10-mg/ml (a) and 4.5-mg/ml (b) of HA. Shear storage moduli are measured at 1-Hz frequency. Blue arrows indicate conditions for both composites with a 1 to 2 of molar ratio of SH groups to (DA+MAL) groups. *$p < 0.05$ (Student-*t* test).

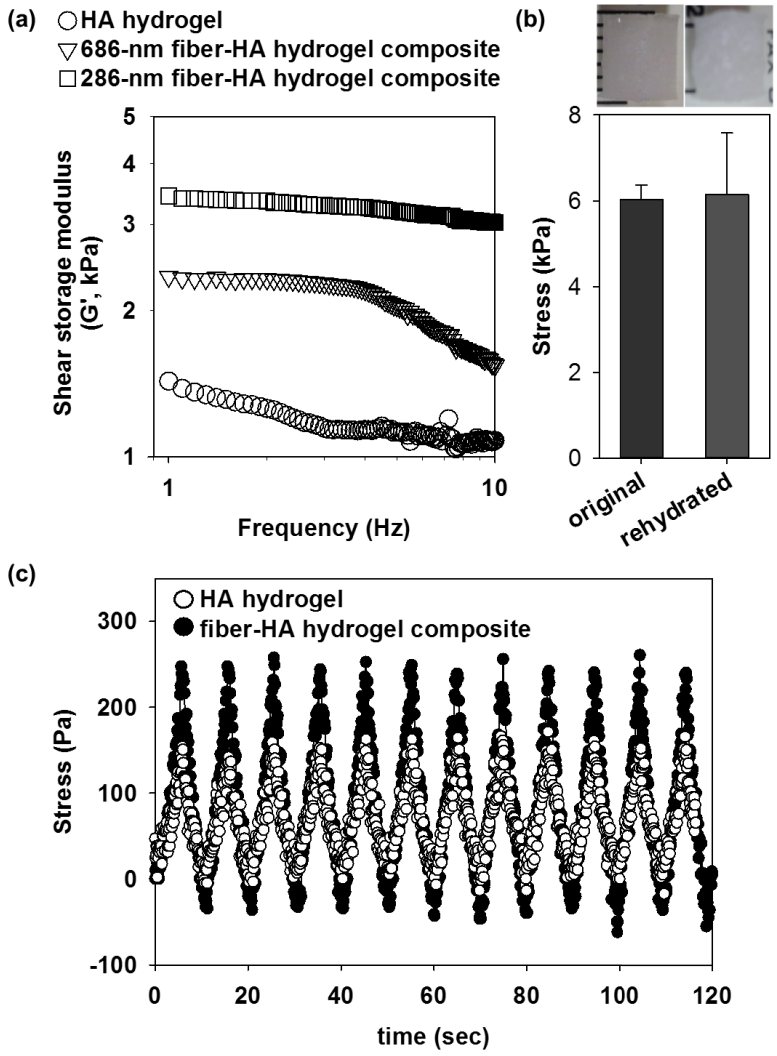

Figure 5-5: Mechanical strength of the fiber-HA hydrogel composite under different frequencies (a), rehydration (b), and cyclic loading (c).

(a) Shear storage modulus of the HA hydrogel and the composites measured against different frequencies of shear loading; (b) Comparison for the compressive stress of the composites before and after rehydration (strain = 40%); (c) Compressive stresses of an HA hydrogel and the corresponding composite measured against cyclic loading (strain = 25%).

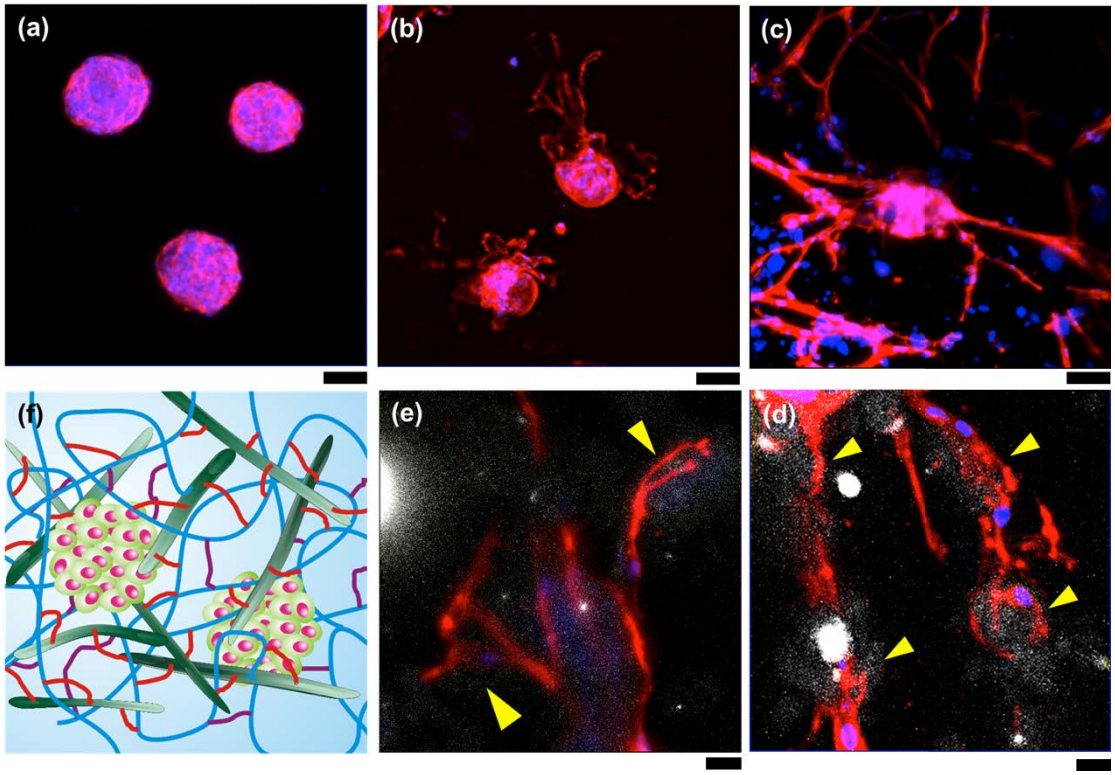

Figure 5-6: Migration ability of human adipose-derived stem cells (hASCs) in HA hydrogel and composite

(a), nanofibers-HA hydrogel composite (b, e) and RGD-nanofibers-HA hydrogel composite (c, d) on Day 27. The HA hydrogel control and the two composites were selected to exhibit similar compressive moduli of around 1.9 kPa. Yellow arrows in (d) and (e) indicate cells adhering to fibers or fibers clusters. F-actin and nuclei of hASCs were stained with Alexa Fluor® 568 Phalloidin (red) and DAPI (blue), respectively. Nanofibers were labeled with Alexa Fluor® 647 (white). (f) Schematic illustration of hASCs spheroids in the composite structure with interfacial bonding between PCL fibers and HA chain network. Scale bars = 100 μm (a–c) and 20 μm (d–e).

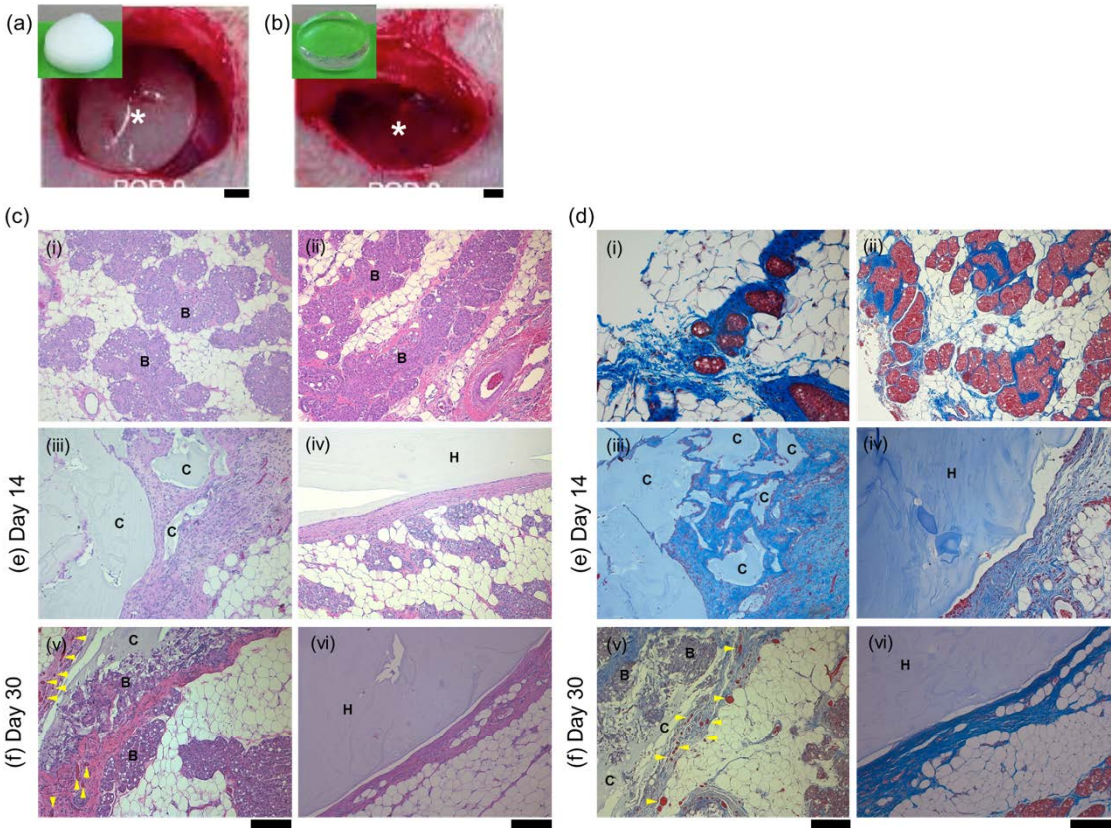

Figure 5-7: Tissue regeneration mediated by the implanted fiber-HA hydrogel composite and HA hydrogel in 30 days.

(a, b) Macroscopic images of the composite (a) and the HA hydrogel (b) before (insets) and after implantation under the inguinal fat pad (scale bar = 2 mm). White stars indicate the implanted matrices. (c, d) H&E and Masson's trichrome stained-images of (i) native fat tissue, (ii) healed tissue after sham surgery, (iii, v) the fiber-HA hydrogel implanted tissue, and (iv, vi) the HA hydrogel implanted tissue on Day 14 and Day 30. Blue staining in panel (d) from Masson's trichromatic staining indicates total collagen in examined tissue. In the images, H = HA hydrogel, C = fiber-HA hydrogel composite, B = brown adipose tissue, yellow arrow = blood vessel. Scale bar = 200 mm.

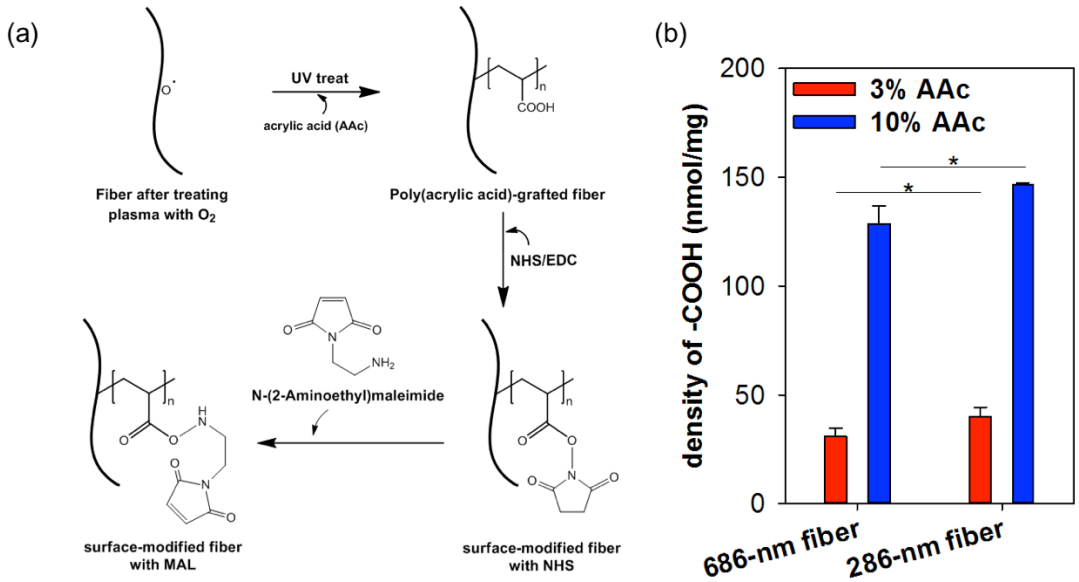

Figure 5-8: Conjugation scheme for functionalizing fiber surface

(a) Schematic diagram of preparing surface-modified fibers with MAL *via* PAA-grafting method; (b) Average densities of carboxyl groups on fibers after the PAA-grafting with 3 and 10 % (v/v) of acrylic acid (*$p < 0.05$, n = 6).

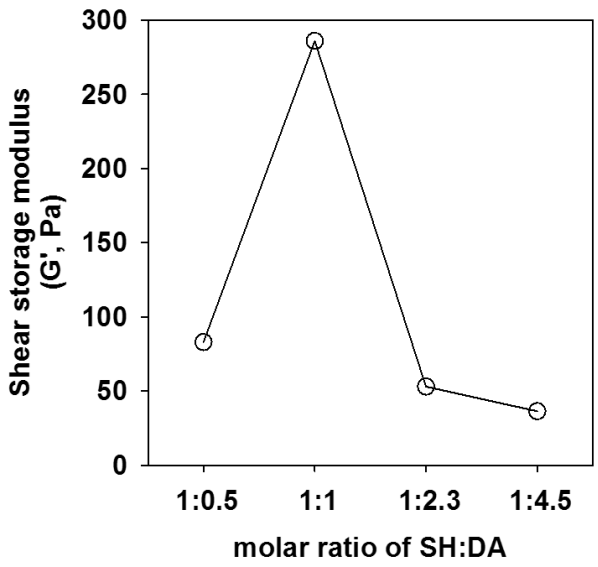

Figure 5-9: (a) Shear storage moduli of HA hydrogel with various molar ratios of SH to DA prepared with 4.5 mg/ml HA-SH.

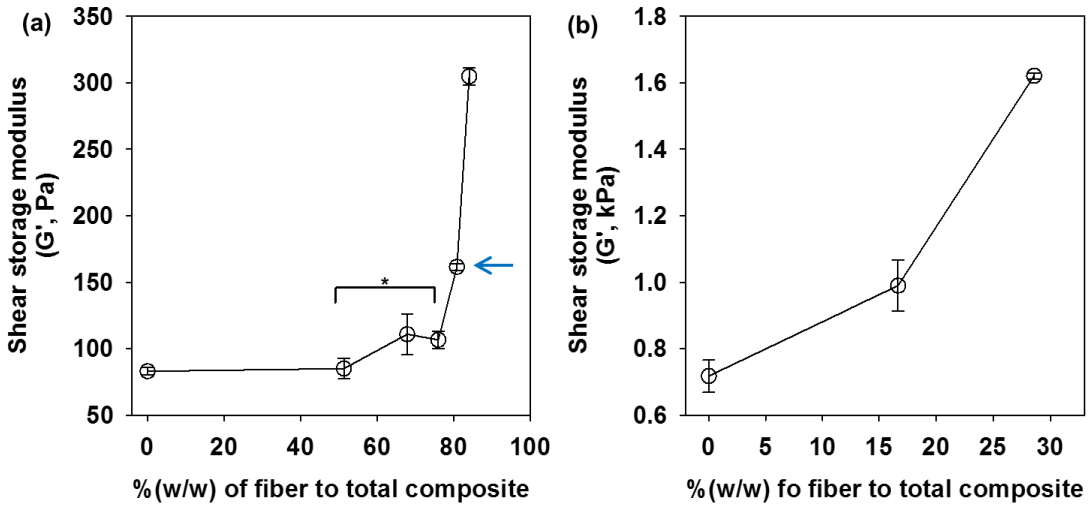

Figure 5-10: (a) Shear storage moduli of fiber-HA hydrogel composites prepared from various amount of fibers.

The average diameter of fibers is 686 nm, MAL surface density on the fibers was 100 nmol/mg, and the composites were prepared with 4.5 mg/ml of HA-SH and 5 mg/ml of PEGDA. Blue arrows indicate 1 to 2 of molar ratio of SH groups to (DA+MAL) groups. (b) Shear storage moduli of fiber-PEG hydrogel composites with various amounts of loaded fibers. *$p < 0.05$ (n = 3).

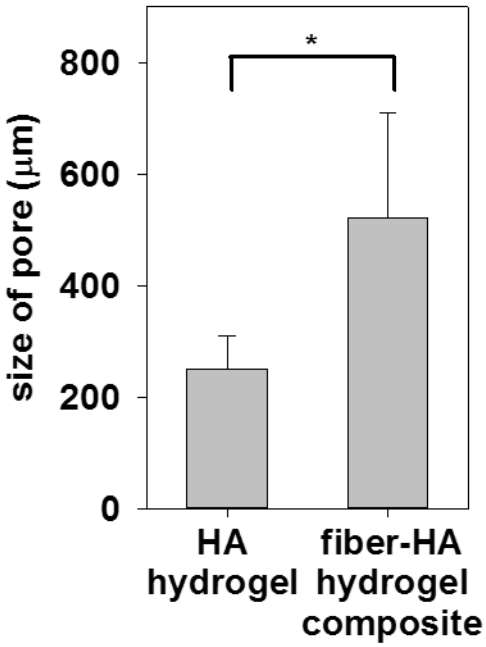

Figure 5-11: Pore Sizes of hydrogels used in rat studies.

The average pore size of HA hydrogel and nanofiber-HA hydrogel composite were estimated based on the SEM images of their cross-section (*$p < 0.05$).

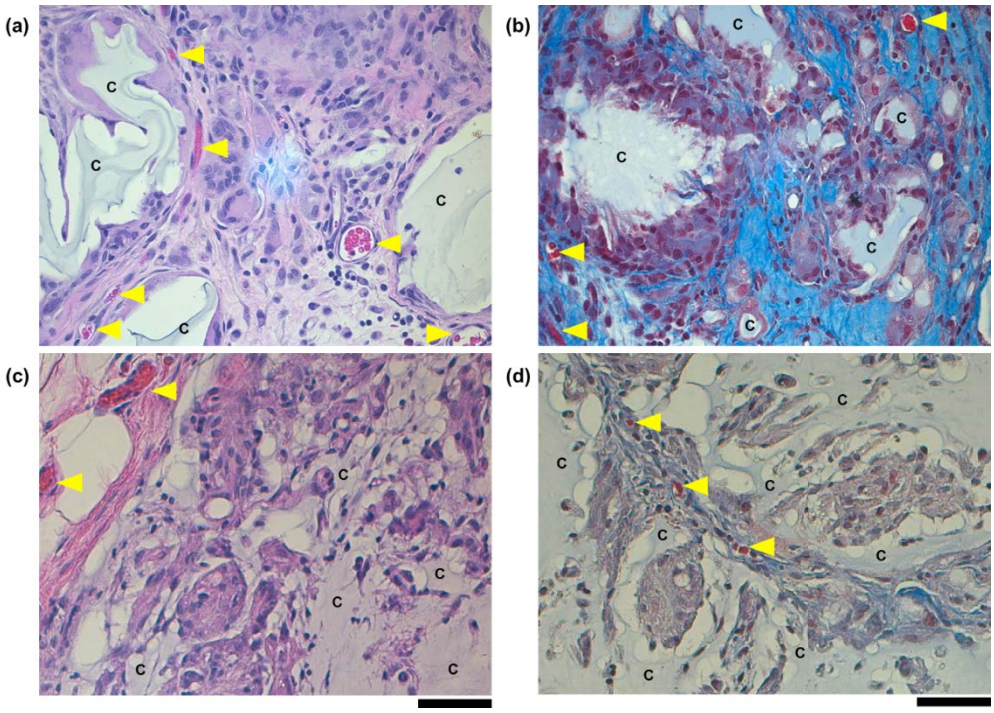

Figure 5-12: Cell infiltration and tissue in-growth through the fiber-HA hydrogel composite on Day 14 (a, b) and Day 30 (c, d).

The sectioned tissues were stained by H&E (a, c) and Masson's Trichrome (b, d) for total collagen (blue). Labels: C = fiber-HA hydrogel composite, yellow arrow = blood vessel. Scale bar = 50 mm.

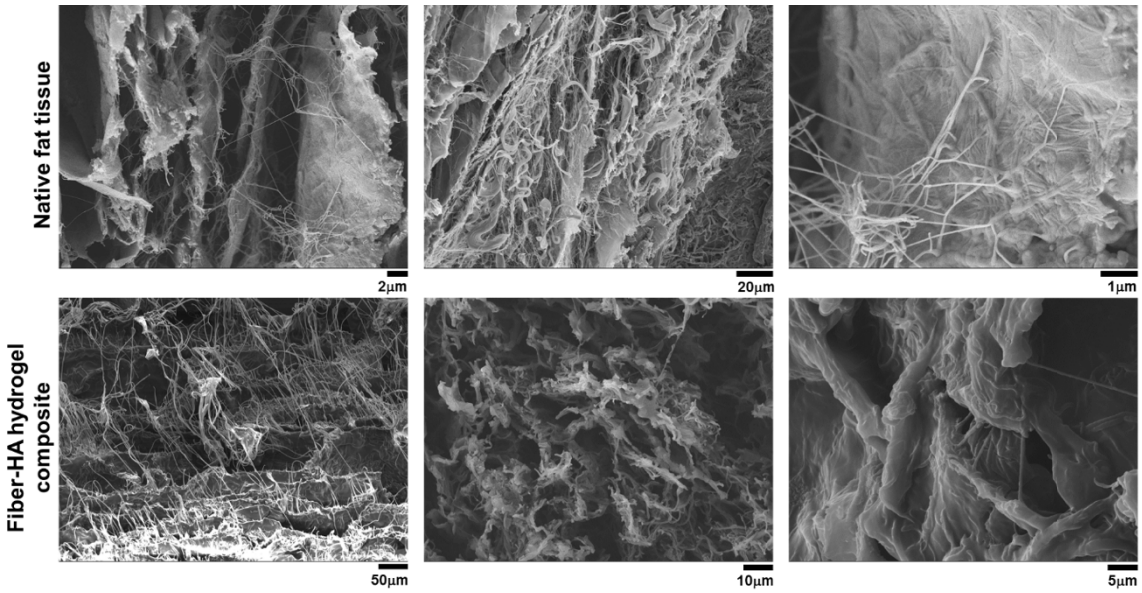

Figure 5-13: SEM images of decellularized fat tissue (upper panel) and the fiber-HA hydrogel composite (lower panel).

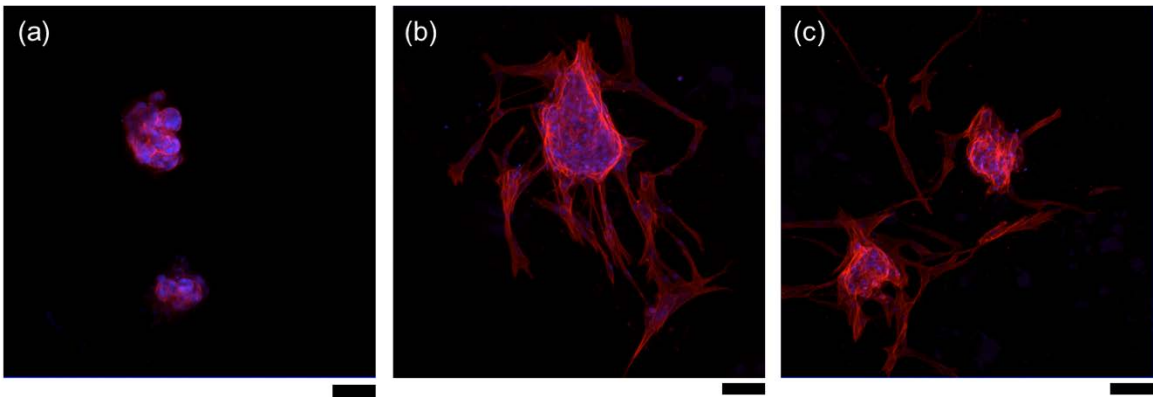

Figure 5-14: Migration ability of hASCs in HA hydrogels

(G' = 24.85 ± 2.92 Pa) (Panel a), 1.0-mm fiber-HA hydrogel composite (G' = 32.29 ± 2.16 Pa) (Panel b), and 286-nm fiber-HA hydrogel composite (G' 39.56 ± 1.26 Pa) (Panel c) on Day 4. The HA hydrogel was fabricated with 2.5 mg/ml of HA-SH and 5.0 mg/ml of PEGDA, and the composites were fabricated with 2.5 mg/ml of HA, 5.0 mg/ml of PEGDA and 10 mg/ml fibers. Scale bar = 100 mm.

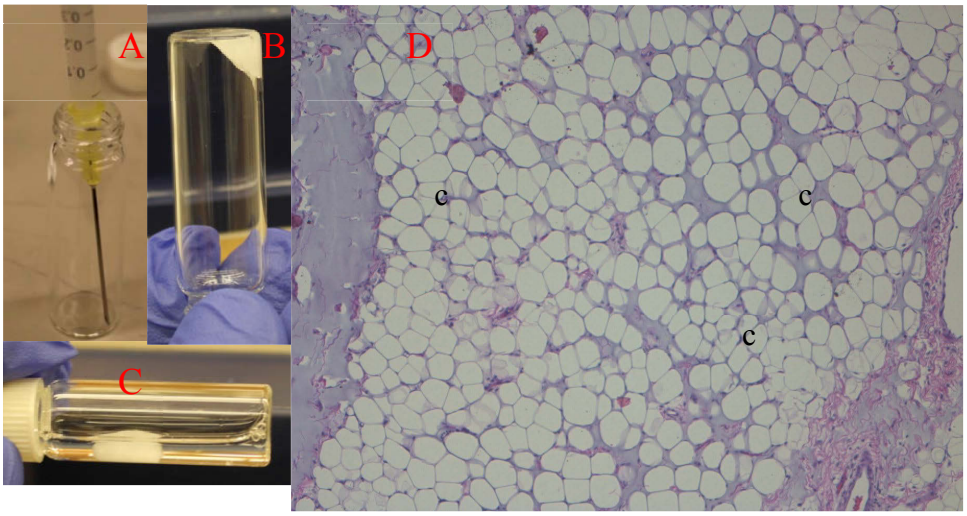

Figure 5-15: A. Injectable Formulation.

The fiber-hydrogel composite can be formulated for injectable applications. B. The injectable composite is stable immediately after injection. C. The injectable composite remains non-dispersive in water with shape and volume retention. Cell infiltration and tissue in-growth through the injectable fiber-HA hydrogel composite on Day 30, showing extensive cellular remodeling and adipocyte formation. The sectioned tissues were stained by H&E. Labels: c = fiber-HA hydrogel composite

5.7 References

1. LoTempio, M.M. and R.J. Allen, *Breast Reconstruction with SGAP and IGAP Flaps*, in *Plast. Reconstr. Surg.* 2010. p. 393-401.
2. Patel, K.M., et al., *Management of Massive Mastectomy Skin Flap Necrosis Following Autologous Breast Reconstruction*, in *Ann Plast Surg*. 2012. p. 139-144.
3. Calobrace, M.B. and P.J. Capizzi, *The biology and evolution of cohesive gel and shaped implants.* Plast Reconstr Surg, 2014. **134**(1 Suppl): p. 6S-11S.
4. Tsoi, B., et al., *Safety of tissue expander/implant versus autologous abdominal tissue breast reconstruction in postmastectomy breast cancer patients: a systematic review and meta-analysis.* Plast Reconstr Surg, 2014. **133**(2): p. 234-49.
5. Kakagia, D. and N. Pallua, *Autologous Fat Grafting In Search of the Optimal Technique.* Surgical innovation, 2014. **21**(3): p. 327-336.
6. Largo, R.D., et al., *Efficacy, safety and complications of autologous fat grafting to healthy breast tissue: a systematic review.* J Plast Reconstr Aesthet Surg, 2014. **67**(4): p. 437-48.
7. Young, D.A., et al., *Injectable hydrogel scaffold from decellularized human lipoaspirate*, in *Acta Biomaterialia*. 2011, Acta Materialia Inc. p. 1040-1049.
8. Varma, D.M., et al., *Injectable carboxymethylcellulose hydrogels for soft tissue filler applications*, in *Acta Biomaterialia*. 2014, Acta Materialia Inc. p. 4996-5004.
9. Salibian, A.A., et al., *Stem cells in plastic surgery: a review of current clinical and translational applications.* Arch Plast Surg, 2013. **40**(6): p. 666-75.
10. Alkhouli, N., et al., *The mechanical properties of human adipose tissues and their relationships to the structure and composition of the extracellular matrix.*, in *Am. J. Physiol. Endocrinol. Metab.* 2013. p. E1427-35.
11. Sommer, G., et al., *Multiaxial mechanical properties and constitutive modeling of human adipose tissue: a basis for preoperative simulations in plastic and reconstructive surgery.* Acta Biomater, 2013. **9**(11): p. 9036-48.
12. Ryu, J.H., et al., *Catechol-functionalized chitosan/pluronic hydrogels for tissue adhesives and hemostatic materials.* Biomacromolecules, 2011. **12**(7): p. 2653-9.
13. Khetan, S., et al., *Degradation-mediated cellular traction directs stem cell fate in covalently crosslinked three-dimensional hydrogels*, in *Nat Mater*. 2013. p. 458-465.
14. Li, X., et al., *Engineering in situ cross-linkable and neurocompatible hydrogels.*, in *J Neurotrauma*. 2014. p. 1431-1438.
15. Slevin, M., *Angiogenic Oligosaccharides of Hyaluronan Induce Multiple Signaling Pathways Affecting Vascular Endothelial Cell Mitogenic and Wound Healing Responses*, in *Journal of Biological Chemistry*. 2002. p. 41046-41059.
16. Yusong, P., X. Dangsheng, and C. Xiaolin, *Mechanical properties of nanohydroxyapatite reinforced poly(vinyl alcohol) gel composites as biomaterial*, in *J Mater Sci*. 2007. p. 5129-5134.
17. Wu, G., et al., *In vitro behaviors of hydroxyapatite reinforced polyvinyl alcohol hydrogel composite.* Materials Chemistry and Physics, 2008. **107**(2-3): p. 364-369.

18. Young, D.A., et al., *Injectable hydrogel scaffold from decellularized human lipoaspirate.* Acta Biomaterialia, 2011. 7(3): p. 1040-1049.
19. Coburn, J., et al., *Biomimetics of the extracellular matrix: an integrated three-dimensional fiber-hydrogel composite for cartilage tissue engineering*, in *Smart structures and systems*. 2011, NIH Public Access. p. 213.
20. Zhou, C. and Q. Wu, *A novel polyacrylamide nanocomposite hydrogel reinforced with natural chitosan nanofibers.* Colloids Surf B Biointerfaces, 2011. 84(1): p. 155-62.
21. Shin, Y.M., et al., *Engineered ECM-like microenvironment with fibrous particles for guiding 3D-encapsulated hMSC behaviours.* Journal of Materials Chemistry B, 2015. 3(13): p. 2732-2741.
22. Christman, K.L. and D.A. Young, *Decellularized and delipidized extracellular matrix and methods of use*. 2012, Google Patents.
23. Jiang, X., G.T. Christopherson, and H.-Q. Mao, *The effect of nanofibre surface amine density and conjugate structure on the adhesion and proliferation of human haematopoietic progenitor cells.* Interface focus, 2011. 1(5): p. 725-733.
24. Katayama, Y., et al., *Coil-reinforced hydrogel tubes promote nerve regeneration equivalent to that of nerve autografts.* Biomaterials, 2006. 27(3): p. 505-518.
25. Xu, W., J. Ma, and E. Jabbari, *Material properties and osteogenic differentiation of marrow stromal cells on fiber-reinforced laminated hydrogel nanocomposites*, in *Acta Biomaterialia*. 2010, Acta Materialia Inc. p. 1992-2002.
26. Holloway, J.L., et al., *Interfacial optimization of fiber-reinforced hydrogel composites for soft fibrous tissue applications.*, in *Acta Biomaterialia*. 2014. p. 3581-3589.
27. Choi, J.S. and H.S. Yoo, *Pluronic/chitosan hydrogels containing epidermal growth factor with wound adhesive and photo crosslinkable properties.* Journal of Biomedical Materials Research Part A, 2010. 95(2): p. 564-573.
28. Placone, A.L., et al., *Human astrocytes develop physiological morphology and remain quiescent in a novel 3D matrix*, in *Biomaterials*. 2015, Elsevier Ltd. p. 134-143.
29. Chua, K.-N., et al., *Stable immobilization of rat hepatocyte spheroids on galactosylated nanofiber scaffold.* Biomaterials, 2005. 26(15): p. 2537-2547.
30. Chua, K.-N., et al., *Surface-aminated electrospun nanofibers enhance adhesion and expansion of human umbilical cord blood hematopoietic stem/progenitor cells.* Biomaterials, 2006. 27(36): p. 6043-6051.
31. Christopherson, G.T., H. Song, and H.-Q. Mao, *The influence of fiber diameter of electrospun substrates on neural stem cell differentiation and proliferation*, in *Biomaterials*. 2009, Elsevier Ltd. p. 556-564.
32. Lim, S.H., et al., *The effect of nanofiber-guided cell alignment on the preferential differentiation of neural stem cells.*, in *Biomaterials*. 2010. p. 9031-9039.
33. Ren, Y.-J., et al., *Enhanced differentiation of human neural crest stem cells towards the Schwann cell lineage by aligned electrospun fiber matrix.* Acta biomaterialia, 2013. 9(8): p. 7727-7736.

Curriculum Vitae

Russell Martin
Born December 6th, 1982 in Mountain View, CA

EDUCATION

PhD, Materials Science & Engineering
Johns Hopkins University
August, 2015
GPA 3.87/4.0

Bachelor of Science, Chemical Engineering
Stanford University, Stanford CA
December 2005

PUBLISHED WORK

- "Nanofiber-based tissue engineering scaffolds for repairing injured nerves and soft tissues" PhD dissertation submitted August 2015

- "Signaling Cue Presentation and Cell Delivery to Promote Nerve Regeneration." . Krick K, Tammia M., **Martin R.**, Hoke A, Mao HQ. *Current Opinions in Biotechnology,* 2011, Vol 22, Issue 5, p. 741-746.

- "Formulation and Characterization of Orally Dissolving Thin Films containing the German cockroach Blatella germanica (Bla g 2) Allergen" Chen Q., **Martin R**., Hoag S., Wood R., Mao H.Q., & Keet, C. (2014). Int J Pharma Sci 4(5), 730-735

- "Differentiation of human ESCs to retinal ganglion cells using a CRISPR engineered reporter cell line." Sluch, V. et al. In submission

- "Hydrogel delivery of neurotrophic factor gradients promotes directional Schwann cell migration and enhanced peripheral nerve regeneration." Krick K.**, Martin R** (co first author). Huang, Y.J., Mi, R, Searson, P, Khademhosseini, A., Hoke, A., Mao, H.Q. In submission

- "Novel nanofiber-hydrogel composite for soft tissue repair." Under preparation

- "The effects of fiber diameter on primary Schwann cell migration." Under preparation

- "Macrophage polarizing nerve wrap for peripheral nerve repair." Under preparation

- "Heat-Stable Measles Vaccine Produced by Spray Drying". *Vaccine*, 2010. Vol 28, Issue 5. p. 1275-1284. Satoshi Ohtake, Russell A. Martin, Luisa Yee, Dexiang Chen, Debra D. Kristensen, David Lechuga-Ballesterosa and Vu Truong-Le

- "Biophysical characterization of rotavirus serotypes G1, G3, and G4" *Human Vaccines*, 2010, Vol. 6, Issue 5, p. 390-398. Reza Esfandiary, Luisa Yee, Satoshi Ohtake, Russell A. Martin, Vu L. Truong-Le, David Lechuga-Ballesteros, David Moore, Sangeeta B. Joshi and C. Russell Middaugh

- "Live attenuated bacterial vaccine: A preformulation study facilitated by a biophysical approach". *Human Vaccines*, 2009, Volume 5 Issue 7. Yuhong Zeng, Haihong Fan, Gary Chiueh, Binh Pham, Russ Martin, David Lechuga-Ballesteros, Vu L. Truong, Sangeeta B. Joshi and C. Russell Middaugh.

- "Using spectroscopic and microscopic methods to probe the structural stability of human adenovirus type 4." *Human vaccines* 6, no. 2 (2010): 202-211. He, Feng, Sangeeta B. Joshi, David D. Moore, Heather E. Shinogle, Satoshi Ohtake, David Lechuga-Ballesteros, Russell A. Martin, Vu L. Truong-Le, and C. Russell Middaugh.

PATENTS

- Issued:
  - US 8268354 B2: "Sonic Low Pressure Spray Drying". Vu Truong, Binh Pham, Luisa Yee, Satoshi Ohtake, **Russell Martin**.
  - US8637090 B2: "Gallium Formulation For The Treatment And Prevention of Infectious Diseases". Satoshi Ohtake, David Lechuga-Ballesteros, Vu Truong-Le, Luisa Yee, Binh V. Pham, **Russell Martin**, Atul Saxena.
- Under Review:

- US 12/880,213 “Formulation for room temperature stabilization of a live attenuated bacterial vaccine”. Vu Truong-Le, Satoshi Ohtake, Gary Chieuh, **Russell Martin**, Atul Saxena, Binh V. Pham, David Lechuga-Ballesteros.
- US 20110243988 A1: “Methods And Compositions For Stabilization Of A Virus Vaccine”. Satoshi Ohtake, Vu Truong-Le, Luisa Yee, **Russell Martin**, David Lechuga-Ballesteros
- US 14/400,856. “Orally dissolving thin films containing allergens and methods of making and use”
- US 61/977,881. “Device and method for a nanofiber wrap to minimize inflammation and scarring”
- US 62/038,030. “Composite Nanomaterials to Promote Soft Tissue Regeneration”

SKILLS AND TRAINING

- Development of biomaterial scaffolds for tissue engineering, including materials for bone, nerve, fat, ocular, and muscle tissues.
- Development of a wide range of electrospun materials
- Translation of academic research into scalable, FDA-compliant manufacturing
- Overseen the work of production operators and undergraduate researchers
- Experienced in the handling and testing of bacteria, mammalian cells, and viruses via agar plating, TCID, optical density, HPLC, and FFA (Fluorescent Focus Assay)
- Experienced with numerous analytical techniques, such as Differential Scanning Calorimetry, Karl-Fischer Moisture Content titration, Atomic Absorption Spectroscopy, HPLC, ELISA, BET Surface Area analysis.
- Excellent lab technique. Experienced in chemical and powder handling and processing. Experienced in working in a cleanroom environment
- Trained on and experienced with pharmaceutical and medical device quality regulations: ISO 13485:2003, cGMP, GLP
- Extensive computer experience, including experience programming in C++ and knowledge of Microsoft Office, Matlab, Origin, and Minitab

PRIOR PROFESSIONAL EXPERIENCE

ARIDIS PHARMACEUTICALS San Jose, CA August 2007 – August 2009

Aridis develops vaccines, specializing in formulating thermally-stable, solid-state forms of biologically active vaccines, composed of bacteria or live attenuated virus. Aridis is also developing a therapeutic antibody for *Pseudomonas Aeruginosa* and a broad-spectrum anti-infective.

Research Associate

- Co-inventor on a submitted patent for a novel nozzle for spray-drying resulting from work that optimized a Spray-Drying process for stabilizing biologically active samples
- Project lead on creating a testing protocol for determining Gallium concentrations in tissue samples using Graphite-Furnace Atomic Absorption Spectroscopy
- Coauthor on paper in *Human Vaccines* on Salmonella-based vaccine development describing formulation optimization
- Developed formulations and process conditions for the following live-attenuated-virus vaccines: Rotavirus, Measles, Adenovirus, and Filovirus
- Created an auto-count program using MIT's CellProfiler to drastically decrease the man-hours needed to count cells in FFA images.
- Developed formulations for our anti-infective candidate to optimize aerosol properties, release rates, and storage stability
- Performed numerous microbiology tests of virus or bacteria titer via FFA, TCID, HPLC, agar plating, and optical density
- Performed and optimized processes for stabilizing biologically active samples via freeze-drying, foam-drying and spray-drying.
- Project lead on developing a formulation and process cycle suitable for Foam-Drying attenuated *Francisella Tularensis*.
- Refined and performed a protocol to test for Adenovirus concentration using Anion-Exchange HPLC (high performance liquid chromatography).

- Conducted Solid-State analyses to help evaluate formulation and process variables using Differential Scanning Calorimetry and Karl-Fischer Titration with focus on moisture content and glass-transition temperature

CALCITEC, INC Santa Clara, CA April 2006 – June 2007

Calcitec developed resorbable calcium phosphate bone substitutes for spinal and orthopedic applications. Calcitec's products are intended to replace autograft and allograft bone. Calcitec halted operations due to a loss of funding.

Associate Process Engineer

- Refined a ceramic manufacturing process which included high-temperature synthesis, size reduction, surface modification, and solids-liquids separations
- Directed both the day-to-day operations and long-term planning for manufacturing personnel
- Created mathematical models of processing steps to aid analysis and upscaling
- Upscaled manufacturing processes to reduce variation and increase throughput
- Determined methods of finding process nonconformities and determined root causes of process variation
- Created and managed system for inventory control for manufacturing
- Created SOP's, inventory control system, protocols, reports, and work instructions for equipment, experiments, and processes compliant with ISO and cGMP standards.
- Validated (IQ, OQ, PQ) process equipment and processes
- Designed and performed experiments using standard wet chemistry techniques

SRU BIOSYSTEMS Woburn, MA June 2004 – August 2004

SRU Biosystems develops optical-based bioassays for use in drug discovery.

Biotech Engineering Intern

- Performed surface modification experiments to increase the product's sensitivity through organic chemistry
- Determined the root cause of a product failure and designed a process change to eliminate the failure

- Created novel optical instrumentation to analyze the product substrate as part of identifying the cause of the product failure

ADDITIONAL INFORMATION

- Stanford Men's Track and Cross Country. Competed for two-time NCAA National Champion Varsity Cross-Country and Track teams
- GRE: 800-Math, 800-Verbal